Power Electronics Interfaces for DC-Microgrids Applications

Gabriel Renan Broday

A Thesis
In the Department
of
Electrical and Computer Engineering

Presented in Partial Fulfillment of the Requirements
For the Degree of
Doctor of Philosophy (Electrical and Computer Engineering) at
Concordia University
Montreal, Quebec, Canada

October 2022

CONCORDIA UNIVERSITY
SCHOOL OF GRADUATE STUDIES

This is to certify that the thesis prepared

By: Gabriel Renan Broday

Entitled: Power Electronics Interfaces for DC-Microgrids Applications

and submitted in partial fulfillment of the requirements for the degree of

DOCTOR OF PHILOSOPHY (Electrical and Computer Engineering)

complies with the regulations of the University and meets the accepted standards with respect to originality and quality.

Signed by the final examining committee:

______________________________________Chair
Dr. Gregory Butler

______________________________________External Examiner
Dr. Reinaldo Tonkoski

______________________________________External to Program
Dr. Hua Ge

______________________________________Examiner
Dr. Pragasen Pillay

______________________________________Examiner
Dr. Chunyan Lai

______________________________________Thesis Supervisor
Dr. Luiz Lopes

Approved by ______________________________________
Dr. Jun Cai, Graduate Program Director

12/2/2022 ______________________________________
Dr. Mourad Debbabi, Dean
Gina Cody School of Engineering and Computer Science

ABSTRACT

Power Electronics Interfaces for DC-Microgrids Applications

Gabriel Renan Broday, PhD.

Concordia University, 2022

The decentralization of power generation has become a topic of high interest for industry and academia. The integration of stochastic Renewable Energy Sources (RESs) at the distribution level is facilitated by incorporating them into a Microgrid. In this scenario, DC-Microgrids are a good option since many RESs, such as photovoltaic and fuel cell, and energy storage units present DC output characteristics. Also, the efficiency of the DC-DC interfaces tends to be higher than in DC-AC and issues such as frequency regulation, reactive power control and synchronization are avoided. The control of segments of the distribution system as a Microgrid also helps with the deployment of new large loads such as Electric Vehicles (EVs).

However, the intermittent nature of RESs presents a natural challenge for the large scale implementation of DC-Microgrids. Since weather and nature conditions (such as wind, tides, and sunshine) can be rather unpredictable and are uncorrelated with power consumption needs, DC-Microgrids based on RESs must be strongly supported by fast acting Energy Storage Systems (ESSs) to balance supply/demand and assure high power quality to the system. Among these storage devices, Supercapacitors (SCs) have seen a rise in their popularity for power quality improvement in DC-Microgrids. SCs are devices with a high power density and high charge/discharge rates that can be used to provide sudden bursts of power by managing currents with high gradients, acting as dynamic devices to either supply the necessary power or demand extra power within the DC-Microgrid. Thus, the interface of such system requires that both the power converter topology and the control scheme present the right set of features.

Therefore, this PhD research work discusses the main aspects regarding the operation of power electronics converters and suitable control laws considering the characteristics of the mentioned application. These aspects include: the modulation scheme employed, steady-state characteristics of the power converters and modelling/design of a suitable control law.

First, a unified controller for multi-state operation of the traditional 4-switch Bidirectional Buck-Boost DC-DC converter is proposed. It employs a carrier-based modulation scheme with three modulation signals that allows the converter to operate in all four possible states and eight different modes of operation. A mathematical model is developed for devising a multi-variable control scheme using feedback linearization. This allows the design of control loops with simple PI controllers that can be used for all multi-state modes under a wide range of operating conditions with the same performance.

Then, to deal with the limitations presented by the previous converter, a novel bidirectional DC-DC converter based on a Tapped-Inductor (TI) for higher voltage gain at moderate duty cycles is proposed. What is more, the direction of the current in the intermediate inductor of the new topology does not need to be reversed for power flow reversal, leading to a faster action and avoiding singularities in the control law. Besides, it can employ a similar multi-state and multi-variable modulation scheme that eliminates the Right Half-Plane (RHP) zero, common in Boost-type converters. A systematic approach for deriving control laws for the TI current and output voltage based on exact state feedback linearization is discussed. The performance of the proposed control scheme is verified by simulation for a SC-based ESS.

Acknowledgments

This research work was funded by the Natural Sciences and Engineering Research Council (NSERC) of Canada and by Concordia University. My most sincere thank you to all the academic, industrial and government partners that made this and many other projects possible.

I would like to start by thanking my family in Brazil. My parents and my brothers were a constant source of motivation and the reminder that, no matter how far you are, there will always be people who love you and cheer for you.

I would like to thank my supervisor, prof. Luiz A. C. Lopes, for the opportunity of working under his supervision. His guidance, support, and most important, his friendship, were essential throughout the course of my PhD. I would like to extend my gratitude to the Power Electronics and Energy Research Group (PEER) professors, Prof. Pragasen Pillay and Prof. Chunyan Lai, for always being there for the students, showing willingness and understanding no matter the situation.

A warm thank you to the committee members, for their time reviewing this thesis and for their guidance on the improvement of this research work.

I would like to thank prof. Gilney Damm, prof. William Pasillas-Lépine, and prof. Houshang Karimi for their contribution in this research work. Additionally, I would like to acknowledge *MITACS-Canada* and the *Réseau Québécois sur L'énergie Intelligente* (RQEI) for providing the necessary funding that allowed me to work with such an extraordinary group of people.

I would also like to thank my colleagues from the PEER group for the technical discussions, friendship and good moments we shared. A very special thank you to my friends Luccas Matiuzzi Kunzler, Amitkumar Kortagere, Chirag Desai, Deepak Chetia, Karin Feistel, Mohamed Ismail Omer and Vincent Prévost. I would also like to take the opportunity to thank my friends back in Brazil, especially William de Jesus Kremes and Fabricio Stadler Grellmann.

Finally, I would like to dedicate this work to Lays, my better half and soulmate. Her love, patience and support were my driving force during this journey. Without you all of this would be meaningless.

Table of Contents

List of Figures

List of Tables

1. Introduction

The decentralization of power generation has become a trend for both the industry and researchers. Environmental and social issues concerning the installation of new fossil-based power plants and the high financial costs associated to the upgrade and maintenance of the current transmission/distribution system are driving the need for a more local and sustainable power generation model. Taking this into account, DC-Microgrids have shown to be a really good option for, among others, the decentralization of power and consequently the modernization of the conventional grid [1] – [4].

By definition, a DC-Microgrid can be seen as an autonomous small-scaled power grid system, consisting of "energy generators/suppliers" from renewable and non-renewable-resources (PV panels, wind turbines, fuel cells, etc.), energy storage devices (such as batteries and supercapacitors) and power electronics interfaces (power converters) [1] - [9]. In summary, the DC-Microgrids can be understood as a complete electrical power system in all characteristics which are inherent to them, but on a tiny scale [8] [9].

In this scenario, DC-Microgrids have been considered a natural approach for better accommodating stochastic Renewable Energy Sources (RESs) and charging of Electric Vehicles (EVs) at the distribution level. Since most of the RESs output DC quantities, the integration of renewables is done with simpler and reduced number of power conversions, where the energy efficiency of the system can be improved and it is much easier to deal with since aspects such as frequency regulation, power factor, reactive power and synchronization are eliminated [1] [2] [10].

DC-Microgrids have also the capability of operating completely independent of the conventional power grid. In this mode, called as island mode, the power generation sources can be placed close to the loads, avoiding, or at least reducing significantly, the need for larger and expensive transmission lines/systems. Recall that transmission lines, as we know it, bring a huge economic and environmental impact that include, among others: restriction of land use, permanent removal of wood and vegetation (which can provoke erosion and soil compaction) and disruption of natural hydrology [11] – [14]. It should be noted that there is a growing increase of power demand caused by the technological advancements of the last decades. The reduction/decrease of the loading of transmission systems caused by the distributed generation nature of DC-Microgrids presents a good solution to meet this growing demand in terms of reliability, reducing power outages and losses due to the proximity of the generation sources and loads [7] [8] [10] [11].

Another important aspect of the implementation of DC-Microgrids is the social inclusion it can provide. Even though the access to electrical energy is already well-established as a basic human right, whether for economical or geographical reasons, there are still some remote communities around the world living without electricity [12] – [14]. Some of this communities, located in African and South/Central-American countries, for example, have great potential for renewable generation based on solar radiation and wind, which can strongly support the implementation of a DC-Microgrid [12] [13]. In this case, the implementation of a DC-Microgrid can greatly improve the quality of life of these communities, where electricity can be used, among others, for household purposes such as lightning, heating and personal hygiene [12] [13].

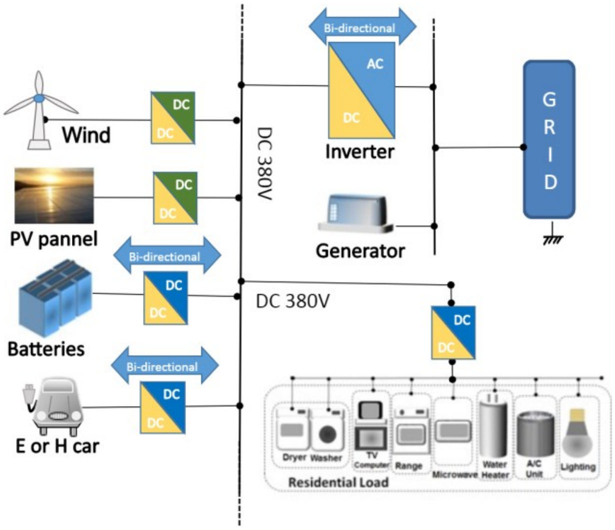

Figure 1.1 – Overview of a DC-Microgrid based in energy storage systems and renewable sources

However, one important factor that should be considered when employing a DC-Microgrid based on renewable power generation is the intermittent nature of RES. Since weather and nature conditions can be rather unpredictable, the employment of such systems must be supported by storage devices in order to proper balance the power demand within the system [15] [16].

Talking specifically about residential DC-Microgrids and Electric Vehicles (EVs), Energy Storage Systems (ESSs) have an important role to play balancing the power generation and power demand within the system, and also on the regulation of power variations in order to keep and assure the power quality through the system. In summary, the ESS will act as a buffer for the DC-Microgrid, storing and supplying back the energy according to the system needs. In [16], some of the main elements used as energy storage units on DC-Microgrids and other DC-applications are presented and discussed, and they are summarized next in Table 1.1.

Table 1.1 – Energy Storage Elements [16]

Storage Unit	**Energy Density** (Wh/l)	**Power Density**	**Lifetime** (in years)	**Response Time** (ms)	**Cost** ($/kWh)
Batteries	**HIGH** (200-350)	**LOW**	**SHORT** (5-15)	**MEDIUM** (3-5)	**LOW** (100-800)
Flywheel	**MEDIUM** (80-200)	**MEDIUM**	**LONG** (>15)	**HIGH** (>10)	**MEDIUM** (1000)
Supercapacitors	**LOW** (2-10)	**HIGH**	**LONG** (>15)	**FAST** (<1)	**HIGH** (10k-20k)
SMES	**LOW** (0.5-10)	**HIGH**	**LONG** (>20)	**MEDIUM** (1-10)	**HIGH** (>20k)

As presented in Table 1.1, the different elements present different characteristics, making them good for some applications and not for others. For example, batteries are widely used for the energy bank of EVs due to their high energy density, but their low power density and low charge/discharge rate represent some natural drawbacks for this application. On the other hand, Supercapacitors (SCs) present high power density and high charge/discharge rates, but since their energy density is low, they cannot fully power an EV, since a SC bank for this application would be costly and with a high volume [15] – [17]. Then, in order to avoid those limitations, batteries and SCs are being merged into a single system in DC-applications called Hybrid Energy Storage Systems (HESSs). The main idea of a HESS is to combine different energy storage units creating a new system capable to provide the benefits of each energy source, thus increasing efficiency and reducing costs of the overall system [18] – [24].

Among these storage devices, SCs have seen a rise in their popularity for power quality improvement in DC-Microgrids. In such application, the power quality within the DC-Microgrid is directly related to the voltage regulation of the common DC-bus, where one should be able to fast and precisely regulate the DC-bus voltage if high power quality is to be achieved. Therefore, since SCs are devices with a high power density and high charge/discharge rates, they can be used in such systems to provide sudden bursts of power by managing currents with high gradients, acting as dynamic devices to either supply the necessary power or demand extra power within the DC-Microgrid, this way keeping the DC-bus voltage of the system strongly regulated [4] [16] [18] [21].

However, SCs are not frequently available, or are more expensive, at high voltage levels and their voltages vary quite a bit with the amount of energy stored. Also, SCs are devices commercially sold with high capacitances and low voltages, and interfacing them to the DC-Microgrid can be quite challenging, especially if the DC-bus voltage is of a high value [25] [26]. Therefore, additional features for the SC power electronics interface is to have a high voltage gain and be able to operate with a wide input/output voltage range. These are also typical characteristics for power electronics interfaces of hydrogen fuel cells that are being considered for EVs as well as for Net-Zero Energy Homes (NZEH), since the fuel cell produces heat as a sub-product of electricity generation [6] [16] [19] [20] [25] [26].

1.1 Challenges of DC-Microgrids and Research Problems

In such systems, power electronics converters will allow the fast and precise control of the power flow among the different devices/elements, maximizing efficiency and improving the interaction between the different elements through the overall system. In this scenario, the study of power electronics converters and their control strategy is of high importance if the mentioned technologies are to be made more accessible to the society [19] [20] [25] [27] [29] [30].

With power electronics converters presenting fast power flow control, the power quality of the mentioned systems can be significantly enhanced. In addition, the use of SCs for fast transients in parallel with batteries avoid the latter providing strong power variations. This can greatly extend batteries lifetime without compromising the SCs which are very well fit for fast power variations.

Taking this into account, different power topologies and control strategies have been proposed for DC-applications in the past few years. Depending on the application, the power electronics converters should present specific characteristics and good trade-offs concerning performance and cost or complexity. The power converters of the ESSs must be bidirectional and can be either isolated or non-isolated. The Dual-Active Bridge (DAB) is an example of the former, allowing higher voltage gains than the latter at the expense of a higher switch-count. Among the non-isolated bidirectional DC-DC converters there are, among others, the Class-C and the 4-switch Buck-Boost converter, with two half-bridges and an intermediate inductor.

Another important factor for the implementation of DC-Microgrids is the control strategy. Aspects such as system reliability, operational and set-up costs and performance/efficiency are directly related to the control law employed within the system [1], [21] – [25]. It is a function of the controllers to provide proper power flow management and, as mentioned before, ensure high power quality through the voltage regulation of the DC-bus voltage.

Power converters frequently employ linear PI-type controllers, mainly due to their simplicity and for the fact that they are already well-established both for academia and industry applications [27] – [30]. They are designed based on converter models linearized around a specific operating point. In this case, in order to obtain the desired linear model, some of the system dynamics are disregarded, and the constant changes of operating conditions within the DC-Microgrids are not taken into account either. Recent studies have shown that this approach plays a major factor on the underperformance and inefficiency of DC-Microgrids, since the performance of PI controllers tends to degrade if the operating point of the converter changes. This might be a significant issue for DC-Microgrids and ESSs that are prone to wide variations and very volatile operating conditions resultant from the impact of RESs generation and variable loads [31] – [35]. Recall that SCs typically operate with voltages in the range of rated to half-rated.

For these reasons, a more robust control strategy must be employed. In this scenario, the use of nonlinear controllers is showing to be a good solution for the volatile nature of working conditions on DC-Microgrids, where the design of nonlinear controllers is based on a complete model of the system, where the nonlinear dynamics and the whole operation space is taken into account . This way, such controllers can provide a broader region of operation, eliminating stability issues and performance degradation as the conditions change [31] – [35].

On the other hand, such approaches still face some resistance to be employed, mainly because they usually rely on more complex models, and a heavy mathematical approach is necessary to determine the control strategy. For cases like this, state feedback linearization techniques are a good and effective alternative. State feedback linearization has been applied to unidirectional Buck, Boost and Buck-Boost converters in [36] – [40], where the proposed nonlinear control laws presented increased robustness and efficiency when compared to traditional linear controllers.

It was also applied to the bidirectional Class-C converter in [41]. However, [41] also discussed another potential issue on the actual implementation of these control laws into real power converters. In this case, if the inductor current is used as a feedback term in the denominator of the control law, the zero crossing of the inductor current represents a difficult feature to deal with.

1.2 Thesis Objectives and Contributions

The applications and topics discussed in the previous sections regarding DC-Microgrids, ESSs and the implementation of power electronics converters for such applications is an area of research with several questions to be addressed.

As mentioned earlier in this Chapter, it will be the power converters employed in the DC-Microgrids and storage systems that will allow the fast and precise power flow control of the system assuring high power quality. There has been a lot of work regarding the use of different topologies and their advantages/disadvantages, where the issues addressed go from simplicity of implementation to control aspects. Therefore, the enhanced operation of power converters and consequently the operation of the overall system where they are employed, and also aspects such as system reliability, operational and set-up costs, are directly related to these power electronics interfaces and their characteristics.

This way, this PhD research aims make a contribution on the main aspects regarding the operation of power electronics converters considering the characteristics of the mentioned applications. Among others, these aspects are summarized in this thesis into three mains topics for discussion/contribution: the modulation scheme employed, steady-state characteristics of the power converters and modelling/design of a suitable control law. Thus, the main contributions of this PhD research work are summarized below:

- Proposal of a new modulation scheme for a bidirectional DC-DC converter
- Proposal of a parallel control structure for a bidirectional DC-DC converter
- Proposal of a unified nonlinear control scheme for a bidirectional DC-DC converter
- Proposal of a novel power electronics topology
- Modelling and design of a nonlinear controller for the novel power electronics topology

Based on the above, the following publications were achieved during the realization of this PhD research work:

Journal publications:

- **J1) G. R Broday,** L. A. C Lopes and G. Damm, "Exact Feedback Linearization of a Multi-Variable Controller for a Bi-Directional DC-DC Converter as Interface of an Energy Storage System" on Energies 2022, 15(71), 7923, pp. 1-26, October 2022.

- **J2) G. R Broday**, G. Damm, W. Pasillas-Lépine and L. A. C. Lopes, "A Unified Controller for Multi-State Operation of the Bi-Directional Buck–Boost DC-DC Converter" on Energies 2021, 14(23), 7921, pp. 1-21, November 2021.

Conference publications:

- **C1) G. R. Broday,** L. A. C. Lopes and H. Karimi, "A Robust Nonlinear Multi-Variable Controller for a 5-Switch Bi-Directional DC-DC Converter for DC-Microgrids Applications" on IEEE 1st Industrial Electronics Society Annual On-Line Conference (ONCON) 2022, December 2022, pp. 1-6.

- **C2) G. R. Broday** and L. A. C. Lopes, “A Minimum Power Loss Approach for Selecting the Turns Ratio of a Tapped Inductor and Mode of Operation of a 5-Switch Bidirectional DC-DC Converter” on IEEE 4th International Conference on DC Microgrids (ICDCM) 2021, Arlington - USA, July 2021, pp. 1-7.

- **C3) G. R Broday**, G. Damm, W. Pasillas-Lépine and L. A. C. Lopes, “Modeling and dynamic feedback linearization of a 5-switch tri-state buck-boost bidirectional DC-DC converter” on IEEE International Conference on Industrial Technology (ICIT) 2021, Valencia - Spain, March 2021, pp. 427-432.

- **C4) G. R. Broday** and L. A. C. Lopes, “A novel 5-switch tapped-inductor multi-state bidirectional DC-DC converter” on IEEE International Conference on Industrial Technology (ICIT) 2018, Lyon - France, February 2018, pp. 596-599.

- **C5) G. R. Broday,** C. B. Nascimento, E. Agostini and L. A. C. Lopes, “A bidirectional DC-DC converter for Supercapacitors in Hybrid Energy Storage Systems” on IEEE 11th International Conference on Compatibility, Power Electronics and Power Engineering (CPE-POWERENG) 2017, Cadiz - Spain, April 2017, pp. 298-303.

1.3 Thesis Structure

This PhD thesis consists of 5 Chapters, being this the first one, the Introduction, where the main aspects concerning DC-Microgrids, ESSs and power electronics interfaces were discussed and how this research work aims to make a contribution on this field.

Chapter 2 presents the proposal of a unified nonlinear PI-controller for the operation of a well-known bidirectional DC-DC converter, the 4-switch Bidirectional Buck-Boost DC-DC converter. The novel unified controller is made possible due to the proposal of a novel multi-state modulation scheme for such converter. This new modulation scheme, the modelling of the system, and control considerations, such as controller gains and reference determination, are presented and discussed in detail in this Chapter. The work presented in this Chapter concerns publication J2, as defined in the last section.

Chapter 3 presents the novel 5-switch Bidirectional DC-DC converter proposed in this PhD thesis. The conceptualization of this novel topology and how it arises from some of the limitations presented by the 4-switch Bidirectional Buck-Boost DC-DC converter are discussed. Then, the main working principle of the novel topology along the possible operating states and operating modes are presented. In order to choose one of the possible operating modes for a given operation, a design example is also discussed in this Chapter. The work presented in this Chapter concerns publications C2, C4 and C5.

Chapter 4 presents the modelling and control of the novel 5-switch converter based on exact state feedback linearization employing Lie derivatives. An explicit formal mathematical control design and stability analysis, based on a zero-dynamics formalism, are also presented and discussed. The work presented in this Chapter concerns publications J1, C1 and C3.

Finally, Chapter 5 presents the final conclusions of this thesis and possible future works.

2. A Unified Controller for Multi-State Operation of the 4-Switch Bidirectional Buck-Boost DC-DC Converter

2.1 Chapter Introduction

This Chapter proposes a unified control scheme for the 4-switch Bidirectional Buck-Boost DC-DC converter that allows it to operate in several multi-state (Tri-state and Quad-state) modes. In this way, the RHP zero that usually appears in the output voltage/current to duty cycle transfer functions related to the conventional Dual-state Boost and Buck-Boost modes is eliminated and the most efficient mode can be used for given operating conditions. A carrier-based Pulse-Width Modulation (PWM) scheme that allows the operation of the converter with Dual-state, Tri-state and Quad-state logic is proposed. A model for the converter operating in multi-state with multi-variable control is developed. It is used to derive a unified control scheme based on feedback linearization for the control of the output voltage/current of the converter and the intermediate inductor current with simple PI-controllers, independently. In the proposed scheme, one can have the converter operating in five different multi-state modes by converting control variables w_1 and w_2 from the control scheme, into three modulation signals u_1, u_2 and u_3 according to given rules. Simulation results are used to show that the dynamic performance of the converter with the unified control schemed is essentially the same for the converter operating in any of the multi-state modes and for a wide range of input voltage and output current.

Thus, this Chapter is organized in the following way: In Section 2.2, the multi-state carrier-based Pulse-Width Modulation (PWM) scheme and modes of operation of the DC-DC converter are introduced. Section 2.3 presents the mathematical model of the converter and the proposed control scheme with feedback linearization. Section 2.4 discusses an approach for obtaining the modulation signals for the PWM (u_1, u_2 and u_3) from the control variables (w_1 and w_2) obtained in Section 2.3. A design example is presented in Section 2.5 and the performance of the proposed and conventional control schemes are verified in Section 2.6. The Chapter conclusions are stated in Section 2.7.

2.2 The 4-Switch Bidirectional Buck-Boost DC-DC Converter

Energy storage units such as SCs can provide fast varying currents for power balancing and voltage regulation of DC-grids, provided they have a suitable interface: Power electronics converter and control scheme. A 2-switch class-C DC-DC converter is frequently used as interface of SCs [21]. However, its dynamic response tends to be relatively slow due to the presence of a Right Half Plane (RHP) zero in the output voltage (V_o) to duty cycle (D) transfer function in the Boost mode. This can be addressed with a Tri-state logic that eliminates the RHP zero, at the expense of an addition switch and the use of a multi-variable modulation scheme [42]. Another issue with the class-C converter is that it loses its power flow control ability, due to the conduction of the top anti-parallel diode, when the DC-grid voltage falls below the voltage of the storage device [30].

The 4-switch Bidirectional Buck-Boost converter, with two half-bridges and an intermediate inductor as shown in Figure 2.1, can be used to overcome this issue [43]. In fact, it was used in a DC-bus fault protection scheme in [30] and [44]. Its ability to operate in the Buck, Boost and Buck-Boost modes can be explored in several ways, including increased efficiency [45]-[48]. The Tri-state logic has also been applied to the 4-switch converter operating in the Buck-Boost mode for enhanced dynamic performance [49]. One issue with the Tri-state logic is that it concerns a multi-variable control problem with two variables, usually the ON and OFF duty cycles (D_{on} and D_{off}) that need to be determined. The free-wheeling duty cycle (D_{fw}) is taken as the remainder of the switching period. The small-signal model employed for the design of linear controllers is complicated, mostly when one attempts to control two state variables what leads to the appearance of cross-coupled transfer functions [50]. This can be addressed by keeping constant the duration of a state, typically D_{off} [49], or employing a dual-mode control scheme with parallel [51] or cascaded [52] control loops.

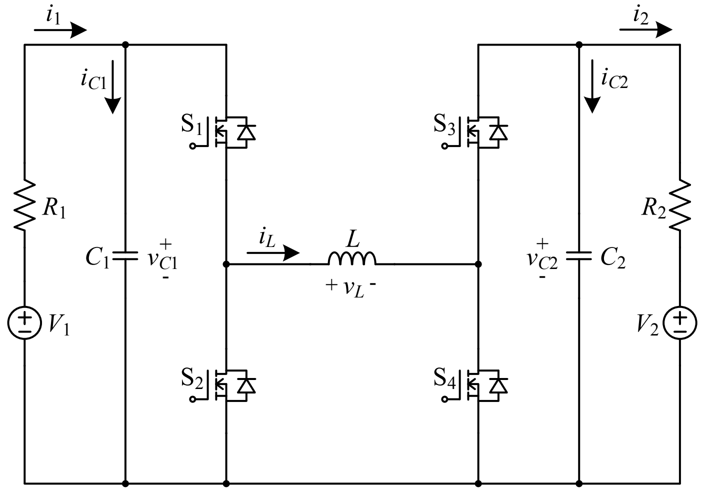

Figure 2.1 – The 4-Switch Bidirectional Buck-Boost DC-DC Converter

2.2.1 Operating States of the 4-Switch Bidirectional Buck-Boost DC-DC Converter

For the proper operation of the 4-switch Bidirectional Buck-Boost DC-DC converter, two switches must be ON at the same time in order to provide a viable current path, which is also called as operating state. Then, the combination of the different operating states that can arise will determine the operating mode and characteristics of the converter for a given operation. For the 4-switch Bidirectional Buck-Boost DC-DC converter, the generation of its operating states is usually done by employing 2 modulating signals, one for the left switch-leg (switches S_1 and S_2), and another one for the right leg (switches S_3 and S_4), where the only constraint is that the switches from the same leg cannot be ON at the same time in order to avoid potential short-circuits [30] [43]-[52]. Then, considering the possible combinations of ON switches at the same time, all four possible operating states for this converter (S_{14}, S_{13}, S_{23} and S_{24}) are shown in Figure 2.2, where the subscript indicates the switches ON at a given time. Thus, State S_{XY} concerns a moment when switches S_X and S_Y are ON/activated together.

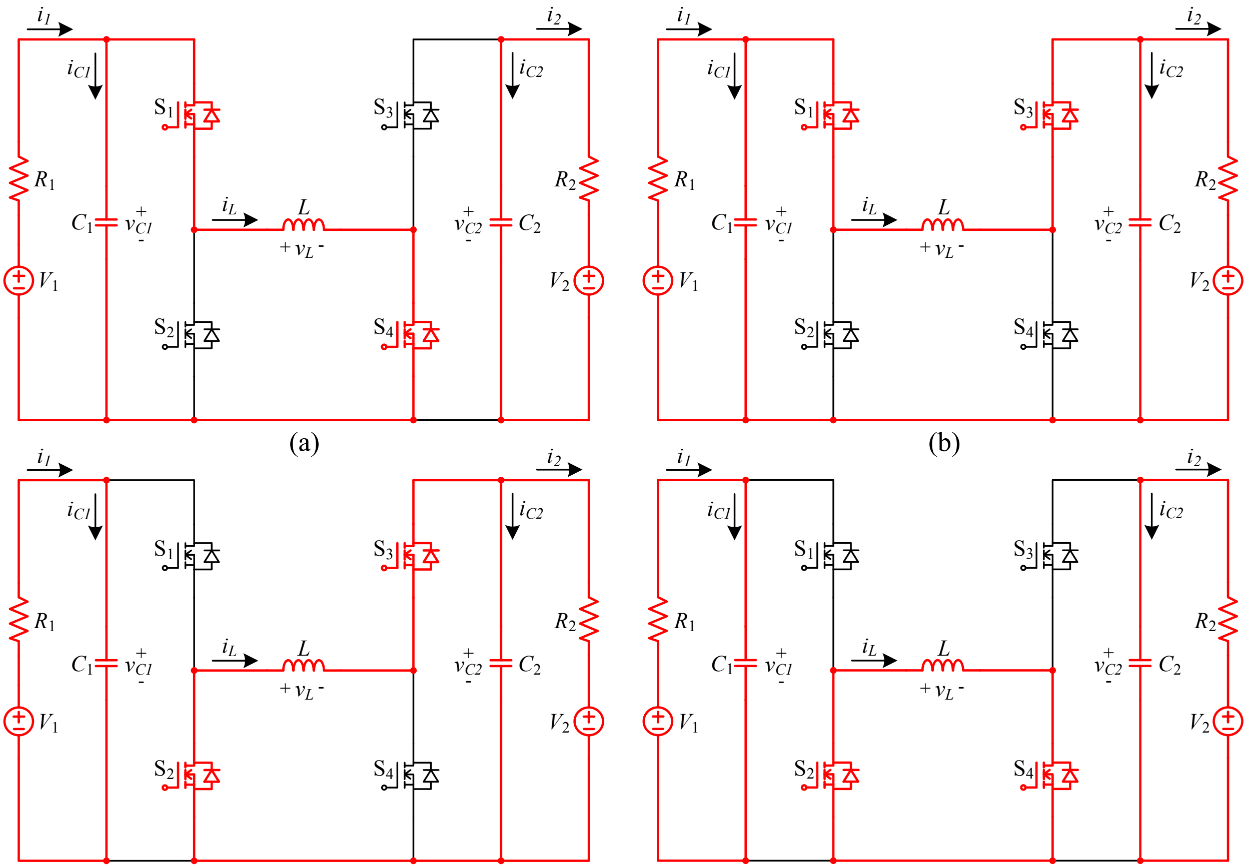

(a) (b) (c) (d)

Figure 2.2 – Operating states of the 4 switch converter: (a) State S_{14}, (b) State S_{13}, (c) State S_{23}, and (d) State S_{24}

From KVL and KCL analysis of the operating states presented in Figure 2.2, the following can be determined, where the main aspects of each operating state are summarized in Table 2.1.

- State S_{14}: In this state, switches S_1 and S_4 are ON. One can find that the voltage v_L across the inductance L is equal to v_{C1}, the currents i_{C1} and i_{C2} through the capacitors C_1 and C_2 are, respectively, (i_1-i_L) and -i_2.
- State S_{13}: In this state, switches S_1 and S_3 are ON. One can find that the voltage v_L across the inductance L is equal to (v_{C1} - v_{C2}). The currents i_{C1} and i_{C2} through the capacitors C_1 and C_2 are, respectively, (i_1-i_L) and (i_L-i_2).
- State S_{23}: In this state, switches S_2 and S_3 are ON. One can find that the voltage v_L across the inductance L is equal to -v_{C2}, the currents i_{C1} and i_{C2} through the capacitors C_1 and C_2 are, respectively, i_1 and (i_L-i_2).
- State S_{24}: In this state, switches S_2 and S_4 are ON. One can find that the voltage v_L across the inductance L is equal to 0, the currents i_{C1} and i_{C2} through the capacitors C_1 and C_2 are, respectively, i_1 and -i_2. This state is also called as free-wheeling state.

Table 2.1 – Summarization of the Operating States of the 4-switch Bidirectional Buck-Boost DC-DC Converter

State	i_{C1}	i_{C2}	v_L	**Current Path/Switches ON**
S_{14}	$i_1 - i_L$	$- i_2$	v_{C1}	S_1 and S_4
S_{13}	$i_1 - i_L$	$i_L - i_2$	$v_{C1} - v_{C2}$	S_1 and S_3
S_{23}	i_1	$i_L - i_2$	$- v_{C2}$	S_2 and S_3
S_{24}	i_1	$- i_2$	0	S_2 and S_4

2.2.2 The Proposed Multi-State Carrier-Based Modulation Scheme

The carrier-based Pulse-Width Modulation (PWM) scheme for the Bidirectional Buck-Boost DC-DC converter proposed in this thesis is shown in Figure 2.3(a). It presents three modulation signals, $0 \leq u_1 \leq u_2 \leq u_3 \leq V_m$, where V_m is the peak value of the sawtooth carrier, usually assumed to be equal to 1 V. With the proposed modulation scheme, a third modulating signal is added, and the control of the right switch-leg is done with 2 modulating signals (u_1 and u_3). By adding an extra modulating signal, all possible operating states can be used within a switching period and, what is more, and what will be a topic of discussion further in this Chapter, the decoupling of the state variables of the system can be achieved. By comparing the modulation signals with the carrier using the circuit shown in Figure 2.4, one obtains the gating signals for switches S_1, S_2, S_3 and S_4

as shown in Figure 2.3(b). All four possible states of operation for this converter, and their sequence within a switching period imposed by the PWM modulator, are shown in Figure 2.3(c).

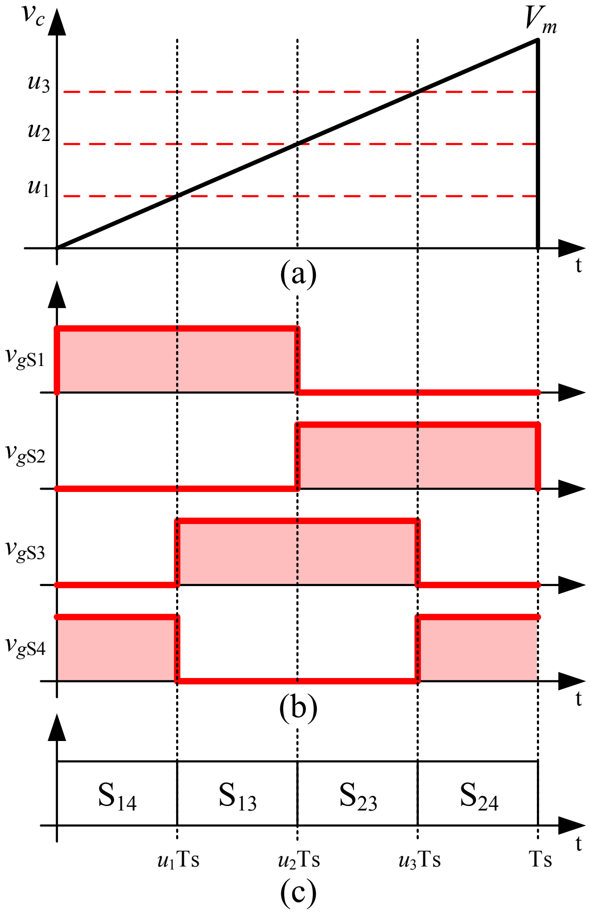

Figure 2.3 – The proposed carrier-based PWM modulation scheme:
(a) Carrier and modulation signals; (b) Gating signals of the switches; c) Operating states

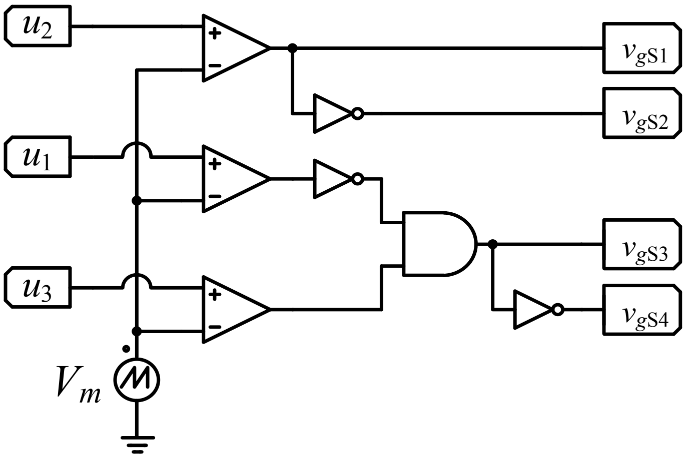

Figure 2.4 – Realization of the proposed carrier-based PWM modulation scheme for the 4-switch Bidirectional Buck-Boost DC-DC Converter

From Figure 2.3, for $V_m = 1$ V, one can see that:

$$u_2 = D_1 \tag{2.1}$$

$$u_3 - u_1 = D_3 \tag{2.2}$$

By setting additional constraints concerning the magnitudes of the modulation signals u_1, u_2 and u_3, one can have the converter operating in eight different modes as shown in Table 2.2. The modes in which the average voltage across the inductor (V_L) cannot be made zero on a switching period are not useful/practical. It should be noted that for operation in Buck modes (1 and 4) it is mandatory that $v_{C1} > v_{C2}$ while for the Boost modes (3 and 6) that $v_{C1} < v_{C2}$. It has been shown that operation in the Buck and Boost modes, when possible, leads to lower power converter losses and stress on the switches than in the Buck-Boost mode [53].

Table 2.2 – Modes of Operation of the 4-switch Bidirectional Buck-Boost DC-DC Converter

u_1	u_2	u_3	**States**	**Mode of Operation**
0	0	u_3	S_{23}-S_{24}	Not useful – Disregard
0	$u_{2,3}$	$u_{2,3}$	S_{13}-S_{24}	Not useful – Disregard
0	u_2	1	S_{13}-S_{23}	1 – Dual-state Buck
$u_{1,2}$	$u_{1,2}$	1	S_{14}-S_{23}	2 – Dual-state Buck-Boost
u_1	1	1	S_{14}-S_{13}	3 – Dual-state Boost
0	u_2	u_3	S_{13}-S_{23}-S_{24}	4 – Tri-state Buck with free-wheeling (fw)
u_1	u_2	1	S_{14}-S_{13}-S_{23}	5 – Tri-state Buck-Boost with no fw
u_1	$u_{2,3}$	$u_{2,3}$	S_{14}-S_{13}-S_{24}	6 – Tri-state Boost with fw ($u_{2,3} \geq u_1$)
$u_{1,2}$	$u_{1,2}$	u_3	S_{14}-S_{23}-S_{24}	7 – Tri-state Buck-Boost with fw ($u_3 \geq u_{1,2}$)
u_1	u_2	u_3	S_{14}-S_{13}-S_{23}-S_{24}	8 – Quad-state

2.3 Mathematical Model for the 4-Switch Converter

In order to obtain the model that describes the dynamics of the system considered in this Chapter, the dynamic-average model approach is applied within a switching period, where one can find the following set of equations:

$$< i_{C1} >_{Ts} = (i_1 - i_L)(u_1) + (i_1 - i_L)(u_2 - u_1) + (i_1)(u_3 - u_2) + (i_1)(1 - u_3) \tag{2.3}$$

$$< i_{C2} >_{Ts} = (-i_2)(u_1) + (i_L - i_2)(u_2 - u_1) + (i_L - i_2)(u_3 - u_2) + (-i_2)(1 - u_3) \tag{2.4}$$

$$< v_L >_{Ts} = (v_{C1})(u_1) + (v_{C1} - v_{C2})(u_2 - u_1) + (-v_{C2})(u_3 - u_2) \tag{2.5}$$

Then, by making the necessary mathematical manipulations and considering the input and output currents (i_1 and i_2) as functions of the capacitor voltages (v_{C1} and v_{C2}), feeder resistances (R_1 and R_2) and the DC-units voltages (V_1 and V_2), one can find the following state space model.

$$\frac{dv_{C1}}{dt} = \frac{V_1}{R_1C_1} - \frac{v_{C1}}{R_1C_1} - \frac{i_L}{C_1}(u_2) \tag{2.6}$$

$$\frac{dv_{C2}}{dt} = \frac{V_2}{R_2C_2} - \frac{v_{C2}}{R_2C_2} + \frac{i_L}{C_2}(u_3 - u_1) \tag{2.7}$$

$$\frac{di_L}{dt} = \frac{v_{C1}}{L}(u_2) - \frac{v_{C2}}{L}(u_3 - u_1) \tag{2.8}$$

According to (2.6)-(2.8), the converter presents three state variables (v_{C1}, v_{C2} and i_L), and three control signals (u_1, u_2 and u_3). Typically, one wishes to control either the output current of the converter (i_2) or the output voltage of the converter (v_{C2}), which require similar control actions. Frequently, this is achieved with an inner inductor current (i_L) control loop and an outer current/voltage loop [28] [30] [49]. However, with the three modulation signals and the four possible operating states, one can decouple the output quantities from the inductor current, having a certain value of v_{C2}, or i_2, with different values of i_L, what is not the case for the conventional cascaded control scheme. This can be exploited for either reducing the losses in the converter, with a low value of i_L, or having a faster dynamic response for the v_{C2}, with a larger value of i_L. Therefore, in this analysis, it is assumed that there will be a reference value for the average value of the output voltage (v_{C2}^*) and a reference value for the inductor current (i_L^*). These values are not independent and a discussion on suitable values for i_L^* is presented in Section 2.4.

In order to control two of the state variables, one can employ two control variables. Therefore, by making the following change of variables:

$$w_1 = u_3 - u_1 \tag{2.9}$$

$$w_2 = u_2 \tag{2.10}$$

One can convert (2.6) – (2.8) to:

$$\frac{dv_{C1}}{dt} = \frac{V_1}{R_1C_1} - \frac{v_{C1}}{R_1C_1} - \frac{i_L}{C_1}w_2 \tag{2.11}$$

$$\frac{dv_{C2}}{dt} = \frac{V_2}{R_2C_2} - \frac{v_{C2}}{R_2C_2} + \frac{i_L}{C_2}w_1 = -\frac{i_2}{C_2} + \frac{i_L}{C_2}w_1 \tag{2.12}$$

$$\frac{di_L}{dt} = \frac{v_{C1}}{L}w_2 - \frac{v_{C2}}{L}w_1 \tag{2.13}$$

These are non-linear equations due to the cross product between state variables and control variables. In such a case, one can design control loops for the average values of the output voltage (V_{C2}) and inductor current (I_L) based on the feedback linearization technique [37] [39] [40].

2.3.1 Output Voltage Control Loop with Feedback Linearization

The feedback linearization technique can be used in the design of a controller for the output voltage of the converter (v_{C2}) as follows. First, an auxiliary input variable (v_x) related to v_{C2} and corresponding to i_{C2} is defined as:

$$\frac{dv_{C2}}{dt} = \frac{v_x}{C_2} \tag{2.14}$$

It provides a means for designing a linear PI-type controller (Gv_{C2}) as shown in Figure 2.5. Then, with v_x being the voltage error (v_{C2}* - v_{C2}) processed by the PI-controller, (2.14) becomes:

$$\frac{dv_{C2}}{dt} = \frac{1}{C_2}\left[k_{pv}(v_{C2}^* - v_{C2}) + k_{iv}\xi_v\right] = \frac{v_{PIv}}{C_2} \tag{2.15}$$

$$\frac{d\xi_v}{dt} = v_{C2}^* - v_{C2} \tag{2.16}$$

It should be noted that v_x is the output of the output voltage loop PI (v_{PIv}) and it corresponds to i_{C2}. In steady-state, I_{C2} and V_{PIv} should be zero. Finally, the value of the control variable w_1 is obtained by substituting (2.12) in (2.15) leading to:

$$w_1 = \frac{1}{i_L}\left[i_2 + k_{pv}\,(v_{C2}^* - v_{C2}) + \,k_{iv}\xi_v\right] = \frac{1}{i_L}(i_2 + v_{PIv}) \tag{2.17}$$

There, one can clearly see the presence of the feedforward signals i_L and i_2, what should make the dynamic response of the performance of the v_{C2} control loop determined essentially by the PI-controller design specifications. Since $0 \leq u_1 \leq u_2 \leq u_3 \leq 1$, and according to (2.9), one should have $0 \leq w_1 \leq 1$. While v_{C2} and V_2, are expected to remain positive at all times, i_2 and i_L become negative as the direction of the power flow reverses, with $V_{C2} < V_2$. Also, when i_L crosses zero, the value of w_1 changes between ∞ and $-\infty$, requiring a limiter to keep it within the [0 – 1] expected range.

From (2.17), one can say that in steady-state, $I_2 = w_1 I_L$ with $0 \leq w_1 \leq 1$. i_L and i_2 should have the same sign, with the magnitude of i_L being larger or equal to the magnitude of i_2. In general, when one applies a positive step in v_{C2}*, the positive error will make v_{PIv} change from "0" to positive. If i_2 and i_L are positive, w_1 increases so as to increase v_{C2}. Conversely, if i_2 and i_L are negative, w_1 decreases, due to the negative sign of i_L, what should make v_{C2} increase since $i_{C2} = w_1 i_L - i_2$. Therefore, the control law described in (2.14) should work for both forward and reverse power flows.

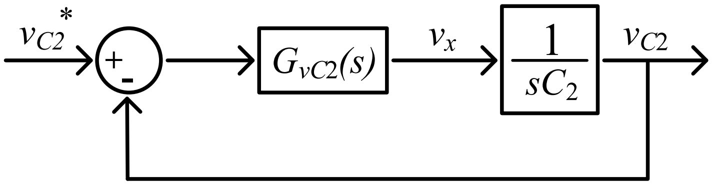

Figure 2.5 – Block diagram with the auxiliary variable v_x used for the design of the output voltage controller

2.3.2 Inductor Current Control Loop with Feedback Linearization

The same approach can be employed for the inductor current control loop. In this case, another auxiliary input variable (v_y), related to i_L and corresponding to v_L, is defined as:

$$\frac{di_L}{dt} = \frac{v_y}{L} \tag{2.18}$$

It provides a means for designing a linear PI-type controller (G_{ciL}) as shown in Figure 2.6. With v_y being the voltage error (i_L* - i_L) processed by the PI-controller, (2.18) becomes:

$$\frac{di_L}{dt} = \frac{1}{L}\left[k_{pi}\,(i_L^* - i_L) + \ k_{ii}\xi_i\right] = \frac{v_{PIi}}{L} \tag{2.19}$$

$$\frac{d\xi_i}{dt} = i_L^* - i_L \tag{2.20}$$

One can see from Figure 2.6 that v_y is the output of the inductor current PI-controller, v_{PIi}, and it corresponds to v_L. In steady-state both V_L and V_{PIi} should be zero. The value of the control variable w_2 is obtained by substituting (2.13) in (2.19), leading to:

$$w_2 = \frac{1}{v_{C1}}\left[v_{C2}w_1 + k_{pi}\,(i_L^* - i_L) + \ k_{ii}\xi_i\right] = \frac{1}{v_{C1}}(v_{C2}w_1 + v_{PIi}) \tag{2.21}$$

In the expression above, one sees the feedforward of signals v_{C1}, v_{C2} and w_1. Neither v_{C1} nor v_{C2} should present any challenges to the computation of w_2, since they should be positive and not much different from V_1 and V_2. By feedforwarding w_1, the dynamic response of the system should be determined by the current PI-controller. Since $0 \leq u_2 \leq 1$ in the PWM scheme and according to (7), $0 \leq w_2 \leq 1$. Concerning the values of w_1 and w_2 in steady-state, one can see from (2.13) that $w_2 > w_1$ if $v_{C2} > v_{C1}$.

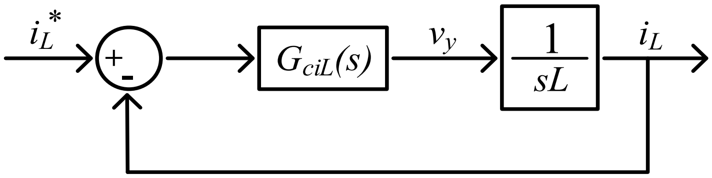

Figure 2.6 – Block diagram with the auxiliary variable v_y used for the design of the inductor current controller

2.3.3 Impact of the Output Current and Input Voltage on the Choice of the Reference Inductor Current

As discussed in previous Sections, variable w_1 will be used for controlling v_{C2} and variable w_2 for controlling i_L. Both control variables should be limited between 0 and 1. This will impose constraints on the possible values of V_1, V_2 and i_L which are important to know. An equation describing this relationship can be derived from the equivalent circuit shown in Figure 2.7. It considers the reflection of the voltages V_1 and V_2 and resistances R_1 and R_2 to the intermediate (inductor) segment of the converter, using the principle of DC-transformer and the duty cycles of the S_1-S_2 and S_3-S_4 converter legs [55].

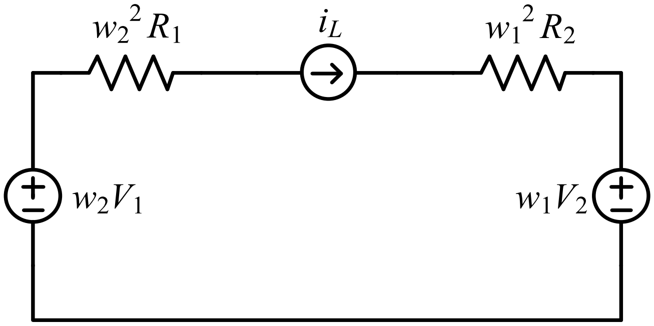

Figure 2.7 – Equivalent circuit of the converter with sources and resistances reflected to the intermediate segment

Based on (2.1), (2.2), (2.9) and (2.10) the duty cycles of the two legs, which correspond to the turns ratios of the DC-transformers, can be computed as:

$$D_1 = w_2 \;\text{ and }\; D_3 = w_1 \tag{2.22}$$

In general, by controlling v_{C2}, one should be able to control i_2, which is related to the inductor current by:

$$i_2 = w_1 i_L \tag{2.23}$$

Therefore, for a given desired output current (i_2) and a given value of inductor current (i_L), a suitable value for w_1 can be determined. Next, one can estimate a candidate value of w_2 for given values of V_1, V_2 and i_L for a specific value of i_2 ($\leq i_L$) and respective value of w_1. For the operating conditions to be feasible, $0 \leq w_2 \leq 1$.

By using KVL in Figure 2.7, the following second order equation can be used for calculating w_2:

$$i_L R_1 w_2^2 - V_1 w_2 + i_L R_2 w_1^2 + V_2 w_1 = 0 \tag{2.24}$$

In order to have $0 \leq w_2 \leq 1$, with given values of V_2, i_L, R_1 and R_2 as w_1 varies between 0 and a maximum value (w_{1max}), there is a minimum value of V_1 (V_{1min}), calculated by:

$$V_{1min} = i_L(R_1 + R_2 w_{1max}^2) + V_2 w_{1max} \tag{2.25}$$

Figure 2.8 shows the values of w_2 as a function of i_2 with a maximum output current (i_{2max}) of 20 A, for V_2 = 48 V, i_L = 40 A (fixed) and $R_1 = R_2$ = 62.5 mΩ for various values of V_1. For this particular case, using (22) with w_{1max} = 0.5, one obtains V_{1min} = 27.125 V. From Figure 2.8, one can see that for values of $V_1 < V_{1min}$ one cannot have $0 \leq i_2 \leq i_{2max}$ with $0 \leq w_2 \leq 1$. Conversely, for $V_1 > V_{1min}$, one can have $0 \leq i_2 \leq i_{2max}$ with $0 \leq w_2 \leq 1$.

Alternatively, one can use a larger i_L, say 60 A, and a smaller w_{1max}, say 0.33, for i_{2max} = 20 A. In this case, one computes V_{1min} = 20.17 V. Figure 2.9 shows the values of w_2 as a function of i_2 ($w_1 i_L$, $0 \leq w_1 \leq 0.33$), for V_2 = 48 V, i_L = 60 A and for various values of V_1. As in the previous case, an i_{2max} of 20 A can be obtained with $0 \leq w_2 \leq 1$, as long as $V_1 \geq V_{1min}$. In general, in order to decrease V_{1min}, it suffices to increase i_L. By using a lower w_{1max}, one increments the Boost effect that allows the use of a lower input voltage.

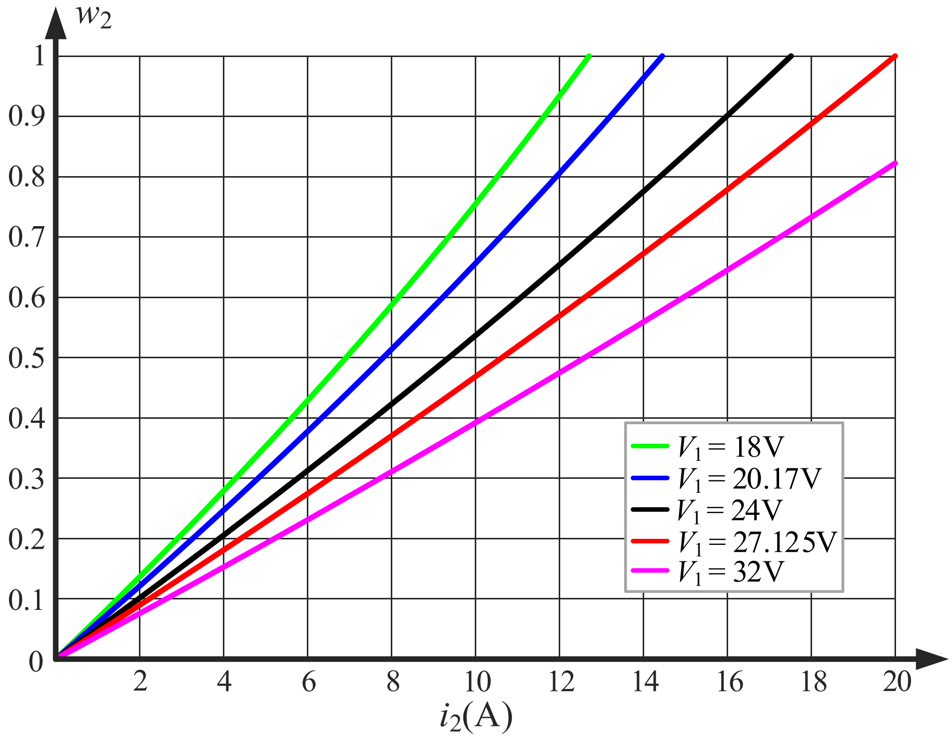

Figure 2.8 – Values of w_2 as a function of i_2 and V_1, for $V_2 = 48$ V, $i_L = 40$ A and $R_1 = R_2 = 62.5$ mΩ. Values of V_1 are: 18 V (green), 20.17 V (blue), 24 V (black), $V_{1min} = 27.125$ V (red) and 32V (magenta).

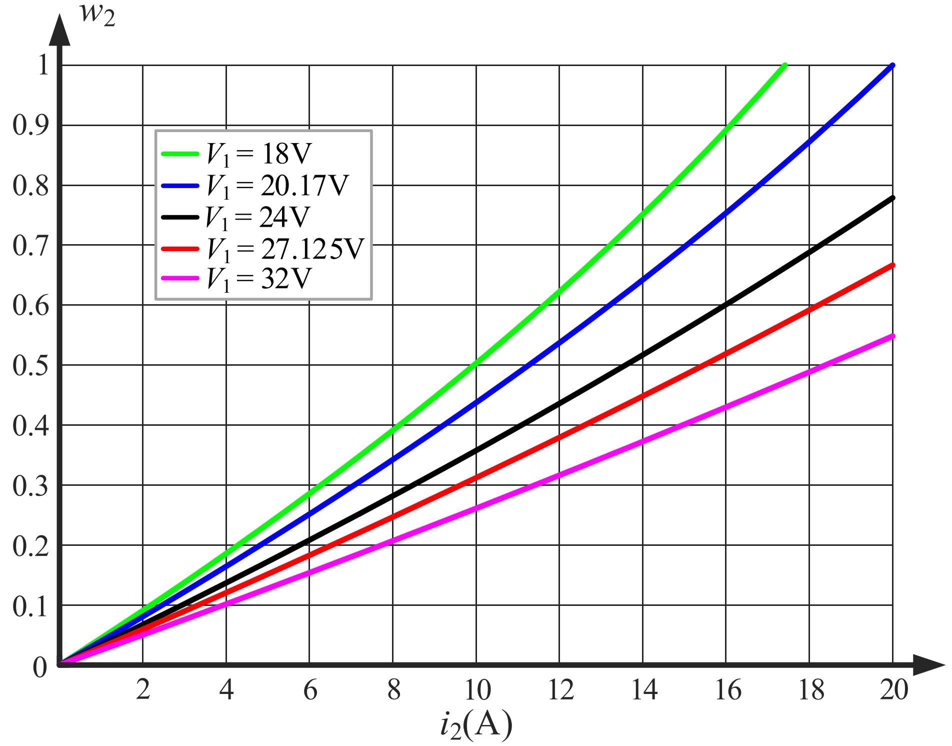

Figure 2.9 – Values of w_2 as a function of i_2 and V_1, for $V_2 = 48$ V, $i_L = 60$ A and $R_1 = R_2 = 62.5$ mΩ. Values of V_1 are: 18V (green), $V_{1min} = 20.17$V (blue), 24V (black), 27.125V (red) and 32V (magenta).

2.3.4 Reference Value for the Inductor Current

In the analysis presented in the previous Section, a constant reference inductor current (i_L*) is considered. One issue is that for a low value of i_2*, a low value of w_1 is used. If one wishes to reduce v_{C2}*and i_2*, the value of w_1 will decrease and possibly saturate, slowing down the dynamic response. Besides, if one wishes to reverse the power flow, both i_2 and i_L need to be reversed. The value of i_L* should change from, say 60 to -60 A, what will take more time to realize, than if the current variation was smaller.

Another option is to determine a value for i_L* as a function of i_2. One of the requirements of this converter is that, since $0 \le w_1 \le 1$ and $i_2 = w_1\, i_L$, $0 \le |i_2| \le |i_L|$. This can be based on a gain (k_{i2L}), where $i_L^* = k_{i2L}\, i_2$, which is the inverse of the value of w_1 in steady-state. To keep w_1 not too low, so that it can be decreased to regulate v_{C2} without saturating at the minimum value, one can select $k_{i2L} = 3$, for $w_1 = 0.33$. This matches with the conditions shown in Figure 2.9, where for $i_{2max} = 20$ A, $i_L = 60$ A and one can operate with $V_{1min} = 20.17$ V.

2.4 Obtaining u_1, u_2 and u_3 from w_1 and w_2

The control scheme developed in Section 2.3 for v_{C2} and i_L considered control variables w_1 and w_2. For the actual implementation of the proposed multi-state PWM scheme, one needs the modulation signals u_1, u_2 and u_3 for generating the gating signals of the switches. As shown in Table 2.2, there are eight possible modes of operation for the non-isolated 4-switch bidirectional Buck-Boost DC-DC converter. Only those that allow independent control of w_1 and w_2 can be used with the proposed control scheme. Based on the values they employ for u_1, u_2 and u_3, one can say that only modes 4-8 comply with this condition. Another aspect to be considered is whether they are compatible with the input and output voltages in the circuit. For instance, mode 4 (Tri-state Buck) can only be used when $v_{C1} > v_{C2}$ while mode 6 (Tri-state Boost) can only be used when $v_{C1} < v_{C2}$. Conversely, modes 5, 7 and 8 (tri-state Buck-Boost and quad-state) can be used for all cases.

Table 2.3 shows how to obtain u_1, u_2 and u_3 from w_1 and w_2 for the five multi-state modes. For mode 5 (Tri-state Buck-Boost with no free-wheeling state), since $0 \le u_1 \le u_2$ then, $1 \le w_1 + w_2$. For mode 6 (Tri-state Boost with free-wheeling), $w_1 \le w_2$. Finally, for mode 8 (Quad-state), one can use a constant large value for c, say 0.95, while ensuring that $w_1 \le w_2 \le c$.

Table 2.3 – Multi-state modes of operation compatible with the proposed control scheme.

u_1	u_2	u_3	**Mode of Operation**
0	w_2	w_1	4 – Tri-state Buck with free-wheeling (fw)
$1-w_1$	w_2	1	5 – Tri-state Buck-Boost with no fw
w_2-w_1	w_2	w_2	6 – Tri-state Boost with fw
w_2	w_2	w_2+w_1	7 – Tri-state Buck-Boost with fw
$c-w_1$	w_2	c	8 – Quad-state

2.5 Design Example

The following parameters were selected for a case study that concerns the interface of a SC rated at 48 V to a DC-grid also rated at 48 V. It is assumed that the voltage in the SC (V_1) can vary between rated and half-rated (24 V $\leq V_1 \leq$ 48 V). Concerning the DC-grid voltage (V_2), it is assumed that it can vary by +/- 5% around rated value, thus 45.6 V $\leq V_2 \leq$ 50.4 V. The other converter parameters are: $R_1 = R_2 = 62.5$ mΩ, $C_1 = C_2 = 76.8$ μF, $L = 38.8$ μH, $f_{sw} = 250$ kHz, -20 A $\leq i_2 \leq$ 20 A.

2.5.1 Controller Design

Based on (2.14) and (2.18), one only needs the values of C_2 and L, respectively, to design the output voltage and inductor current controllers. Since in the actual switched converter voltages and currents present switching harmonics, first order Low-Pass Filters (LPFs) of 100 kHz are employed in both control loops.

The control specifications are determined following standard procedures for the design of PI-controllers. The bandwidth of the inductor current control loop (f_{x_iL}) is selected as 50 kHz (20% of f_{sw}) in order to avoid any interference of the switching frequency into the current control loop and its phase margin as 60°. Since the output voltage of the converter (v_{C2}) is regulated based on the switching of the inductor current through the feedforwarding of w_1, the bandwidth of the voltage control loop should present a slower dynamic when compared to the current loop to fully decouple the two loops, therefore the bandwidth of the voltage control loop is selected as 10 kHz (20 % of f_{x_iL}) and its phase margin as 60°.

Instead of a conventional PI-controller, a type-2 PI-controller is used in this study. The additional pole further helps attenuating the switching harmonics in the sensed inductor current and output capacitor voltage. Their parameters are: $k_i = 13.63$, $\tau_i = 106.16$ μs, $fp_i = 1668$ kHz and $k_v = 2.46$, $\tau_v = 193.43$ μs, $fp_v = 30.4$ kHz.

2.6 Performance Verification

There are several aspects of the proposed concept to be verified. First is the performance achieved with the proposed control scheme with PI-controllers and feedback linearization for various operating conditions: Forward and Reverse power flows with $V_1 < V_2$ and $V_1 > V_2$. This can be done with the mathematical equations derived in Section 2.3 and employing control variables w_1 and w_2. Next is the performance of the actual switched converter. The goal is to demonstrate that one can convert control variables w_1 and w_2, obtained for the unified model, into u_1, u_2 and u_3 so that the converter operates in a desired mode. The dynamic response of the converter should be similar irrespectively of the selected mode of operation, as long as both w_1 and w_2, are used for obtaining u_1, u_2 and u_3.

The schematic diagram of the proposed control scheme is shown in Figure 2.10. There one can see how the control laws for w_1 and w_2 are created as a function of the reference signals and sensed converter quantities. LPFs are included to attenuate the switching harmonics and a limiter is used to prevent the magnitude of i_L, used in the denominator of (2.17), from becoming too small, during power flow reversals. Limiters are also used for keeping w_1 and w_2 that correspond to D_3 and D_1, within 0 and 1. Then, depending on the selected mode of operation, control variables, w_1 and w_2, are converted into the modulation signals u_1, u_2 and u_3, and used in the PWM modulator of Figure 2.3 to create the gating signals for the switched converter.

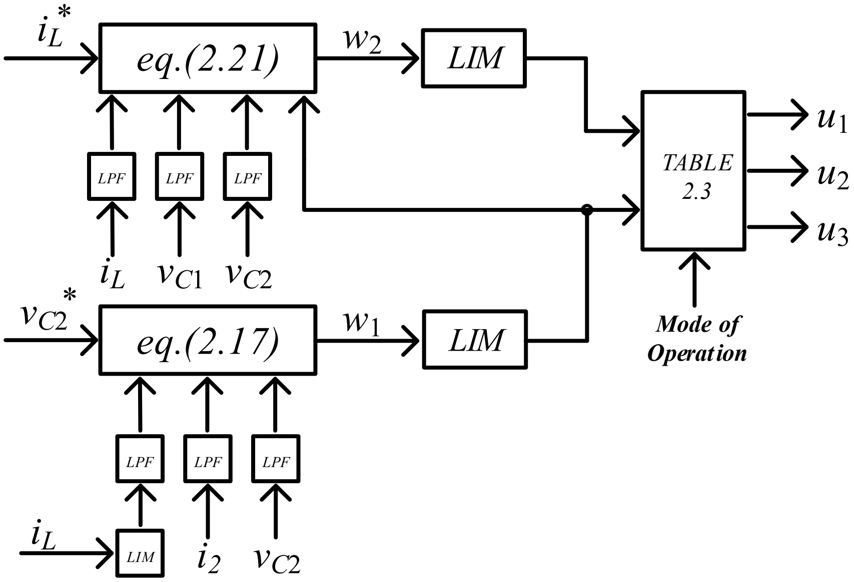

Figure 2.10 – Proposed unified controller for multi-state operation of the bidirectional Buck-Boost DC-DC converter

2.6.1 Control Scheme with PI-controllers and Feedback Linearization

The performance of the proposed unified controller for multi-state operation of the 4-switch Bidirectional Buck-Boost DC-DC converter is verified with the mathematical model in this Section. The parameters of the SC interface (V_1 in Figure 2.1) are those shown in Section 2.5. A SC with a small capacitance (15 mF) is the base value used in this test so that one can observe the variations of the voltage in the storage unit (v_1) as well as the fast varying current and voltage waveforms, in the same time frame. It is assumed that the magnitude of the DC-bus voltage and feeder (v_2) and the value of the feeder impedance (R_2) are known. They are used in the calculation of the reference value for the output capacitor voltage (v_{C2}*) and inductor current (i_L*) as a function of the reference injected current (i_2*). As mentioned in Section 2.3.4, $k_{i2L} = 3$.

Key waveforms obtained with control laws for w_1 and w_2, (2.14) and (2.18), and the mathematical model of the converter, (2.11)-(2.13), are shown in Figure 2.11. On the top, one can see the waveform of the DC-bus voltage (v_2), with an average value of 48 V and a +/-5% triangular ripple of 40 Hz along with the voltage across the SC (v_1). The latter varies as a function of the injected current (i_2), shown just below, which concerns a staircase waveform of 20 Hz and maximum current of 20 A. The voltage across the SC increases when $i_2 > 0$ and decreases when $i_2 < 0$. The injected power is shown in the screen at the bottom, presenting a zero average value. In such a case, the power losses across the two feeder resistors come from the SC, which tends to discharge over time, as seen in the top screen. For most of the time, $v_1 < v_2$, but $v_1 > v_2$ in a short segment. Therefore, the converter needs to operate in both the Boost (step-up) and Buck (step-down) modes. It is evident that there is good tracking of the reference values for the injected current (i_2), output capacitor of the converter (v_{C2}) and inductor current (i_L), with control signals, w_1 and w_2, shown just below those waveforms.

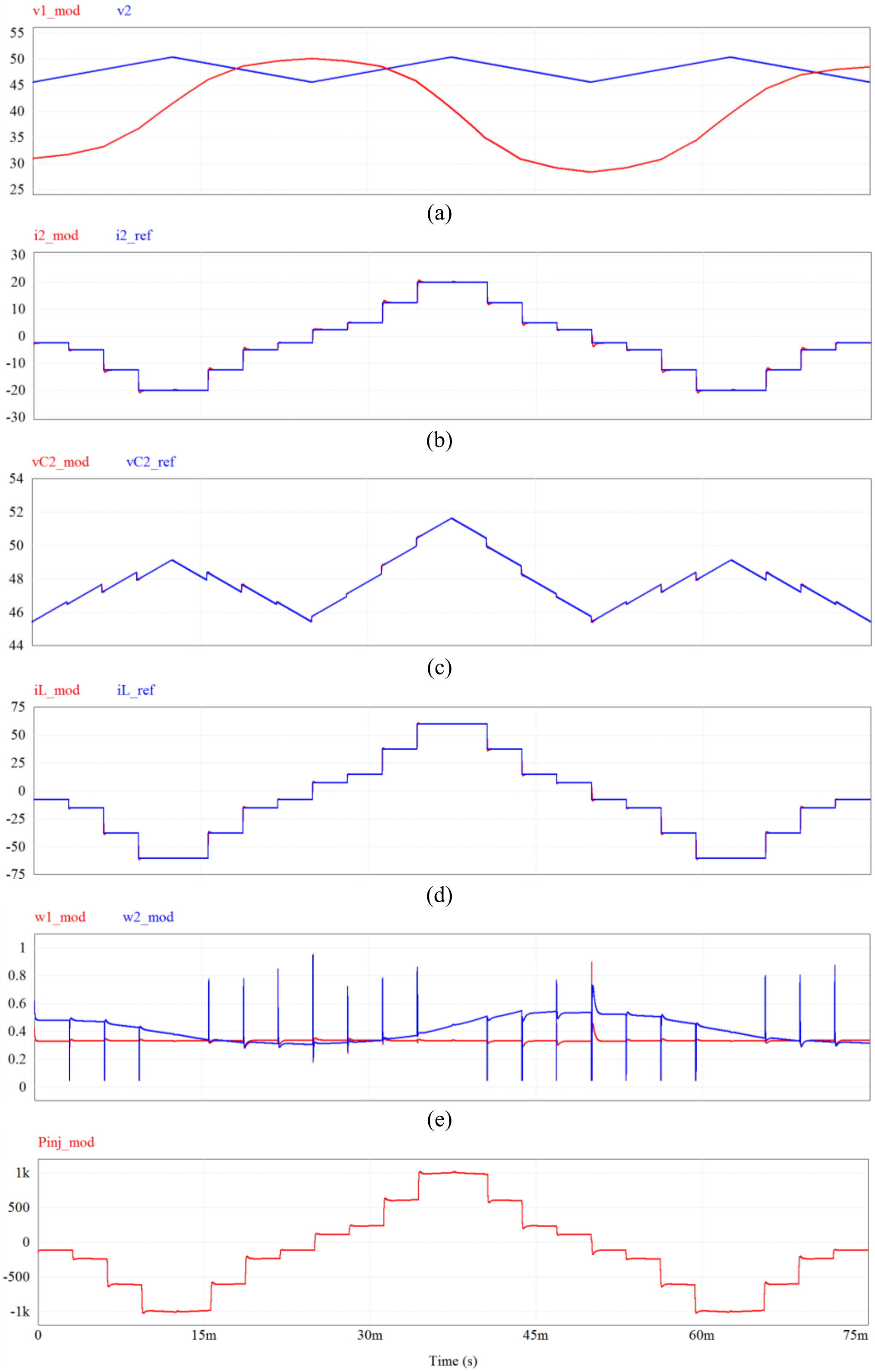

(a)

(b)

(c)

(d)

(e)

(f)

Figure 2.11 – Waveforms with the mathematical model: a) Input and output voltages (in Volts); b) Reference and output current (in Amps); c) Reference and output capacitor voltage (in Volts); d) Reference and inductor current (in Amps); e) Control variables; f) Injected power (in Watts)

2.6.2 Performance Verification with the Switched Converter

Having shown that the proposed control scheme provides a fast and accurate control of the inductor and the output current of the converter using the developed mathematical model of the system, its feasibility is verified with the switched converter for the same test conditions. This is done by simulation with the power electronics software PSIM.

In this case, the control variables (w_1 and w_2) are converted into the modulation signals of the PWM modulator (u_1, u_2 and u_3) so that the converter operates in a desired multi-state mode according to the expressions shown in Table 2.3. Since the converter is expected to operate in the Buck and Boost modes, only the Tri-state Buck-Boost and Quad-state modes, in Table 2.3, are considered at first.

Figure 2.12 shows key waveforms for the switched converter operating in the Quad-state mode. The waveforms are essentially the same obtained for the mathematical model test. The main difference is the presence of switching harmonics. Index “con” indicates results obtained with the switching converter while “mod” refer to the mathematical model.

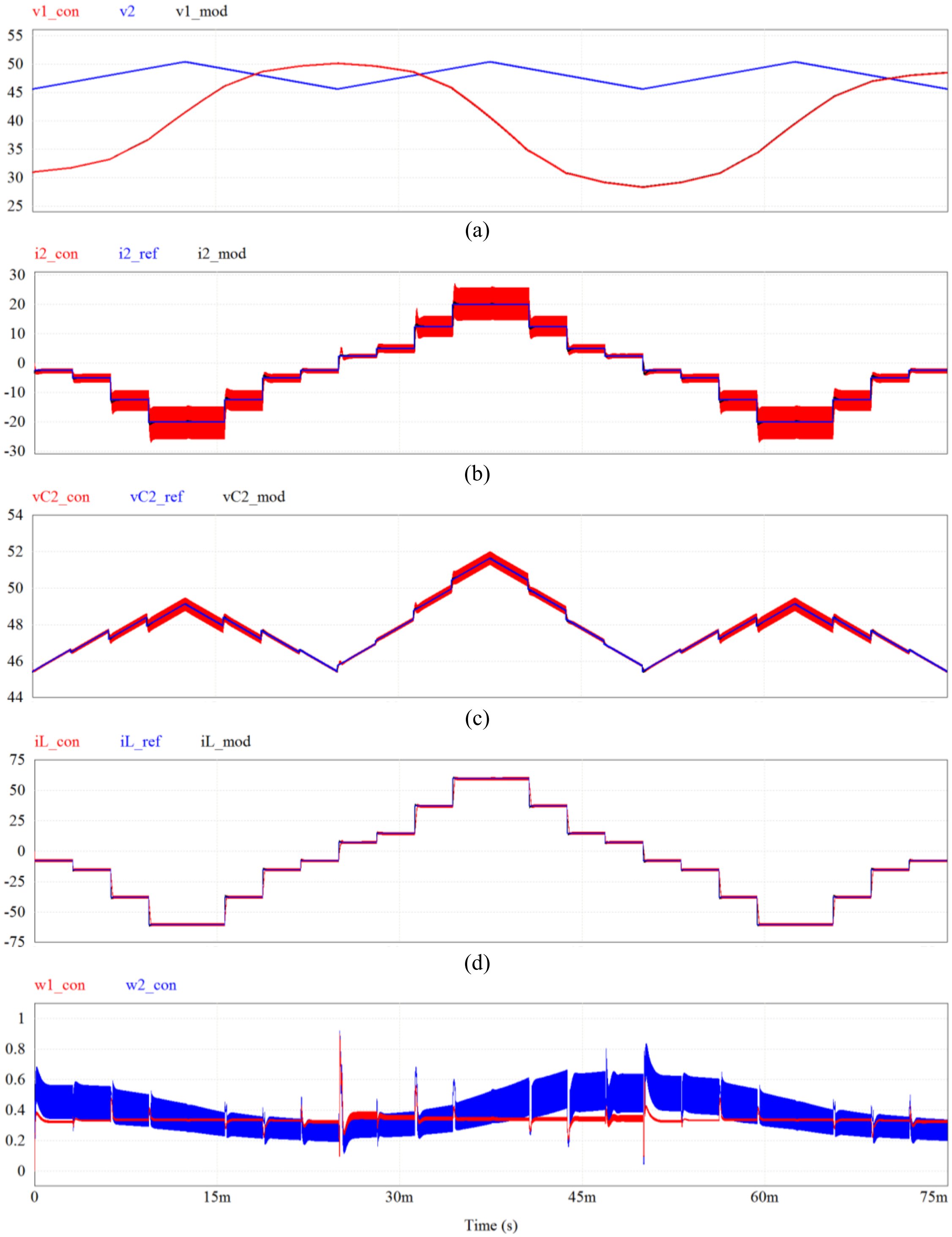

(a)

(b)

(c)

(d)

(e)

Figure 2.12 – Waveforms with the switched converter in the quad-state mode: a) Input and output voltages (in Volts); b) Reference and output current (in Amps); c) Reference and output capacitor voltage (in Volts); d) Reference and inductor current (in Amps); e) Control variables

In Figure 2.13, one can see a close view of the control parameters (w_1 and w_2), the modulation signals ($u_1 \leq u_2 \leq u_3$) and the gating signals of switches S_1 and S_3. There one can observe all sorts of combinations of v_{gS1} and vg_{S3}, meaning that all four switching states are employed in the quad-state mode.

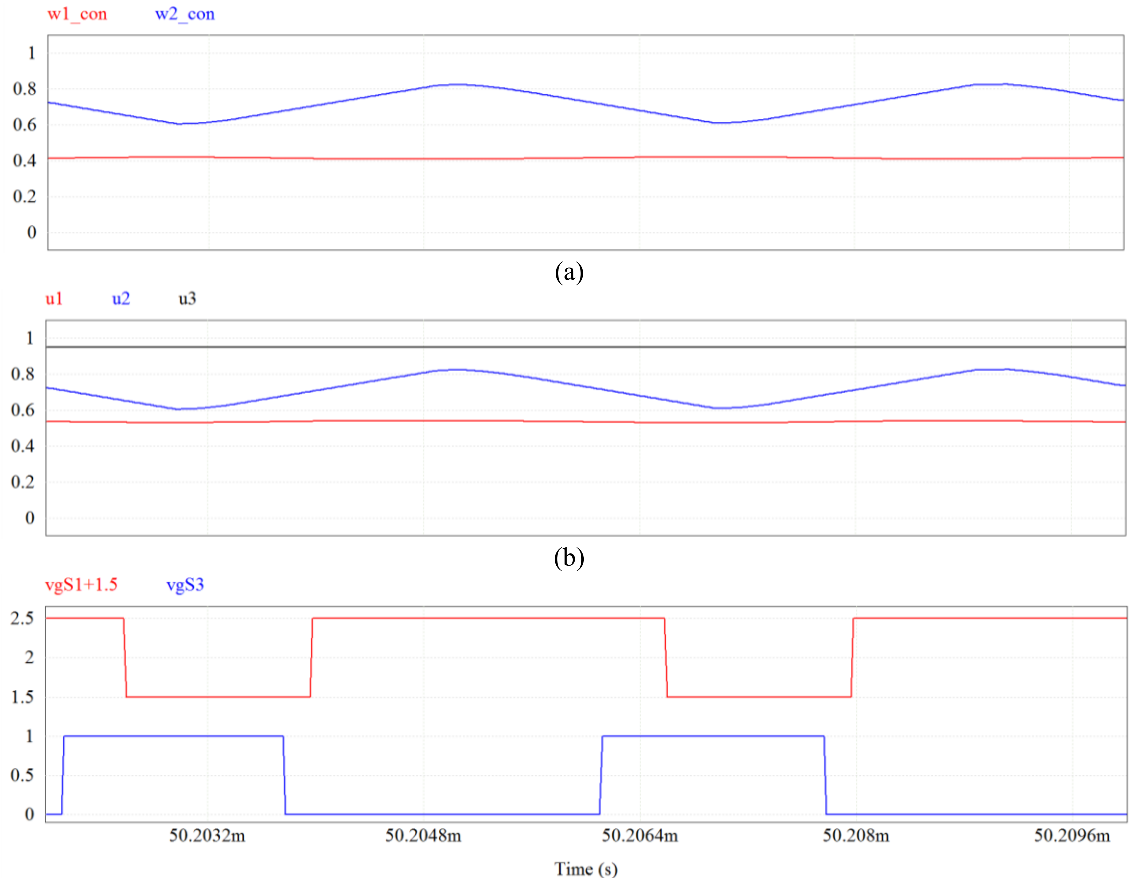

(a)

(b)

(c)

Figure 2.13 – Waveforms with the switched converter in the Quad-state mode:
a) Control variables; b) Modulation signals; c) Gating signals of switches S_1 and S_3

Figure 2.14 shows the same waveforms for the switched converter operating in a tri-state Buck-Boost mode, mode 5 in Table 2.3. The waveforms are essentially the same as those for the quad-state mode. As shown in Figure 2.15, the free-wheeling state, when S_2 and S_4 conduct together, is not present in this mode.

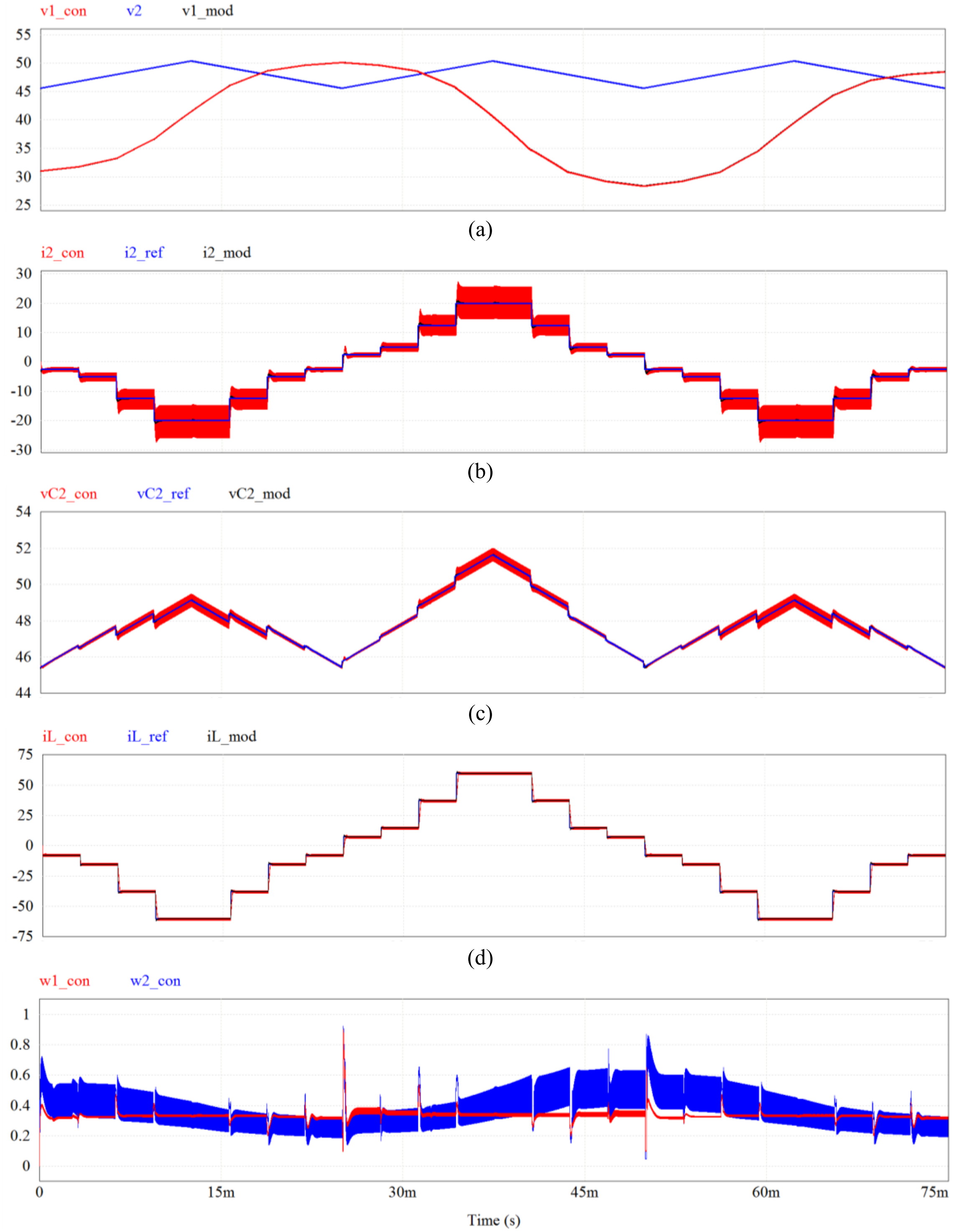

(a)

(b)

(c)

(d)

(e)

Figure 2.14 – Waveforms with the switched converter in the Tri-state Buck-Boost no free-wheeling mode: a) Input and output voltages (in Volts); b) Reference and output current (in Amps); c) Reference and output capacitor voltage (in Volts); d) Reference and inductor current (in Amps); e) Control variables

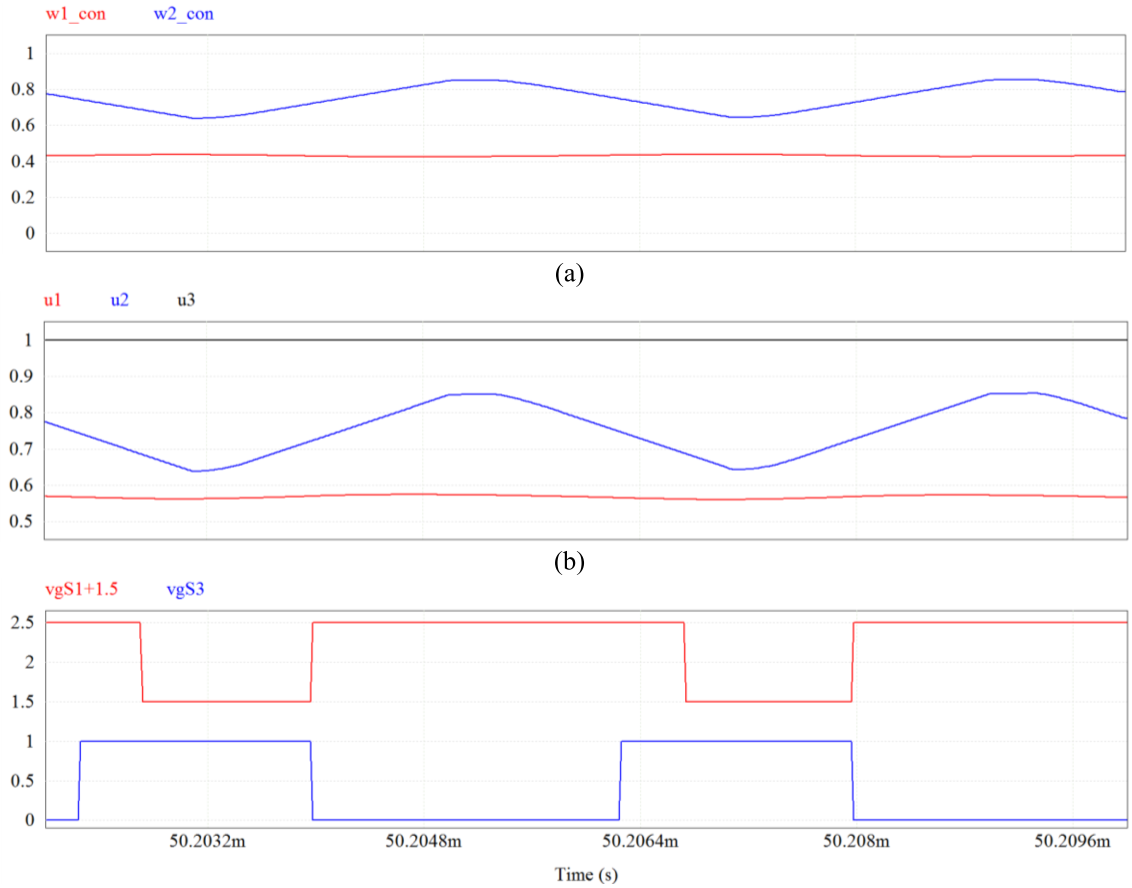

(a)

(b)

(c)

Figure 2.15 – Waveforms with the switched converter in the Tri-state Buck-Boost no free-wheeling mode:
a) Control variables; b) Modulation signals; c) Gating signals of switches S_1 and S_3

For testing the converter operating in the Tri-state Buck and Boost modes, one should always have $v_1 > v_2$ and $v_1 < v_2$, respectively. In order to keep the same output voltage and current waveforms, one can change the initial voltage of the SC (v_1) so that the converter always operates in the desired mode. Besides, it is important to reduce the range of variation of v_1 by increasing the capacitance of the SC to 0.03 F. Figure 2.16 shows waveforms for the switched converter operating in the Tri-state Buck mode, where v_1 is always bigger than v_2.

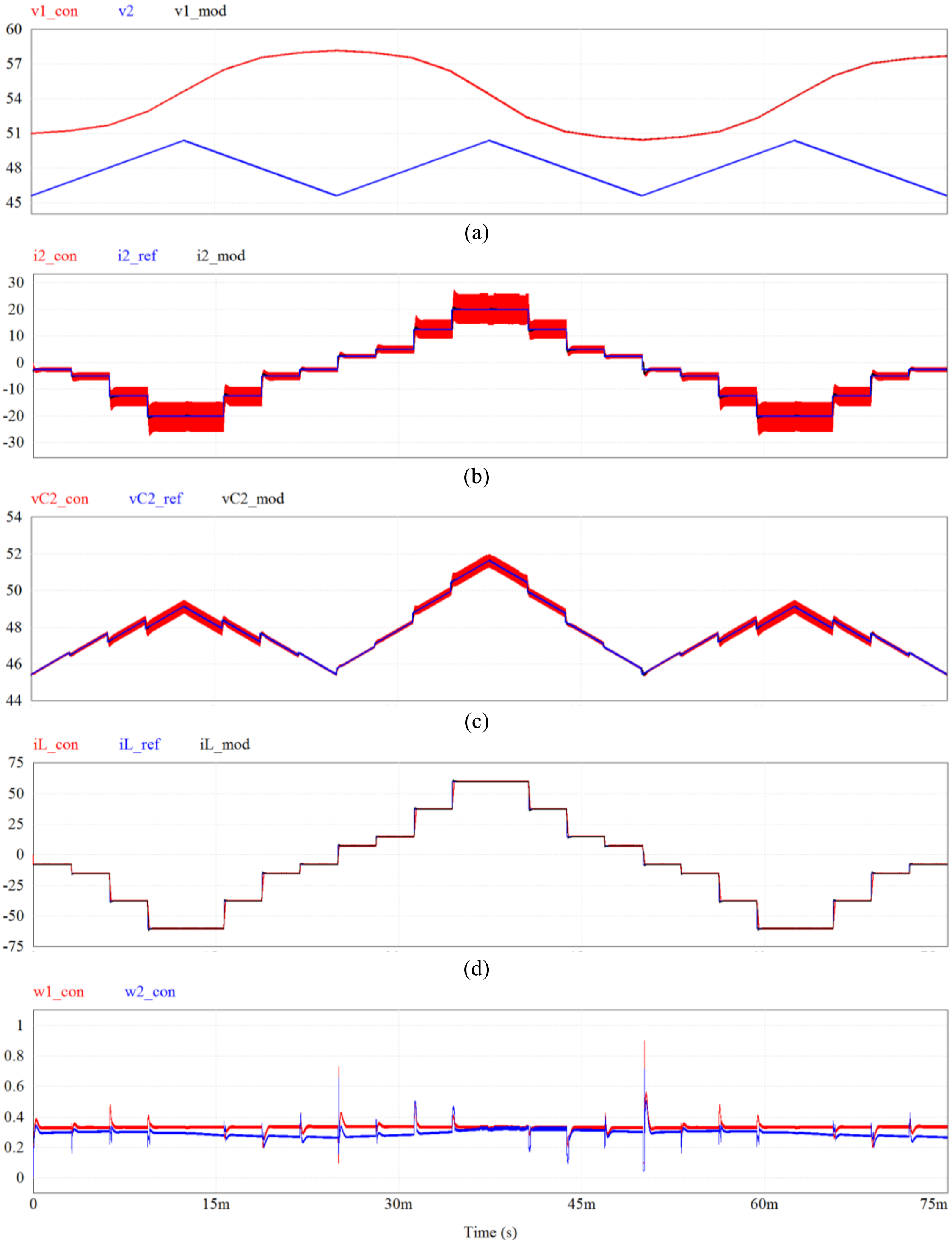

(a)

(b)

(c)

(d)

(e)

Figure 2.16 – Waveforms with the switched converter in the Tri-state Buck mode: a) Input and output voltages (in Volts); b) Reference and output current (in Amps); c) Reference and output capacitor voltage (in Volts); d) Reference and inductor current (in Amps); e) Control variables

Again, the unified controller allows a fast and close tracking of the reference quantities. The quantities obtained with the model, index “mod”, are shown along with those of the switched converter, index “con” to show the similarities. The major difference is the presence of the switching harmonics that can be seen in some waveforms. The control parameters, modulation signals and gating signals of switches are shown in Figure 2.17, where one can see that only three states are used, S_{13}-S_{23}-S_{24}, as seen in Table 2.1.

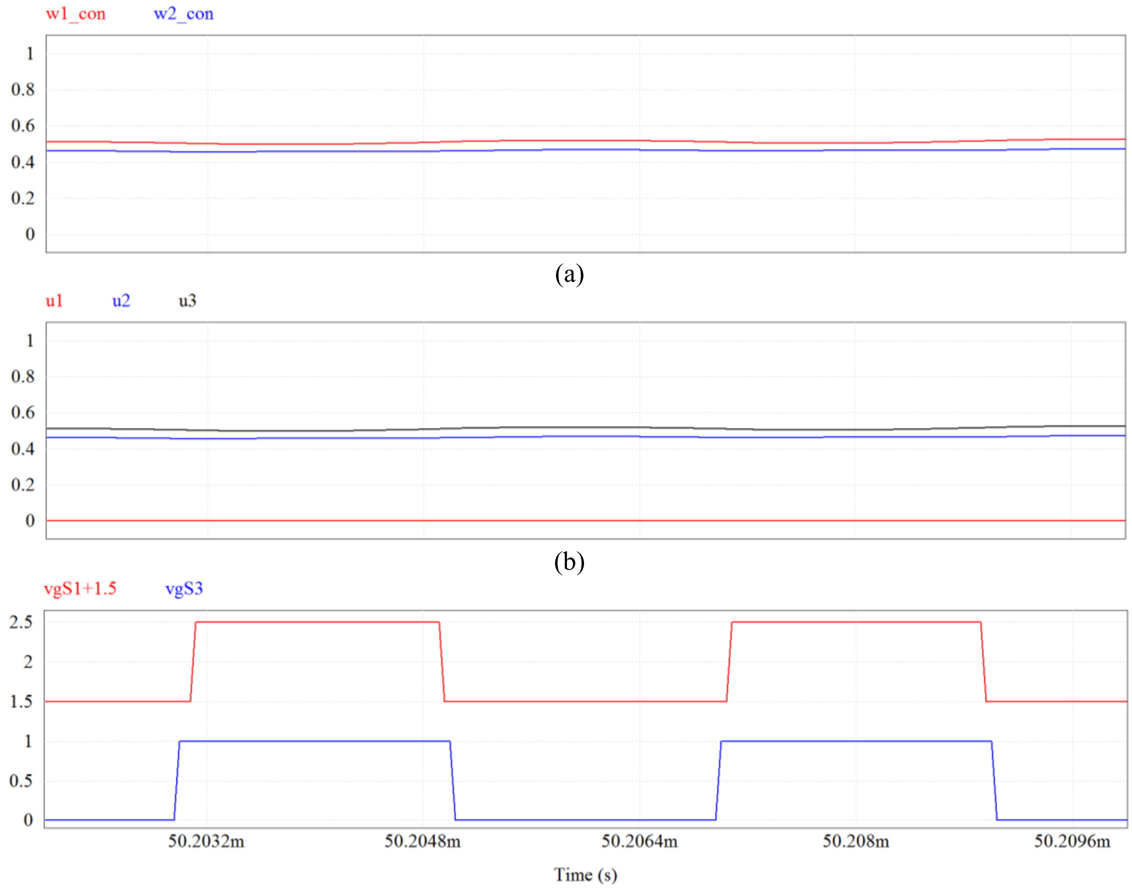

(a)

(b)

(c)

Figure 2.17 – Waveforms with the switched converter in the Tri-state Buck mode:
a) Control variables; b) Modulation signals; c) Gating signals of switches S_1 and S_3

Finally, Figure 2.18 shows waveforms for the switched converter operating in the Tri-state Boost mode, where v_1 is always smaller than v_2. It should be noted that the conventional class-C DC-DC converter could not be used in this case. The unified controller allows a good tracking of the reference quantities. In the bottom screen, the control variables obtained for the switching converter, index “con”, are similar to those obtained for mathematical model, index “mod”. The control parameters, modulation signals and gating signals of switches, with only three-states, are shown in Figure 2.19. In this particular case $u_2 = u_3$, as determined in Table 2.3.

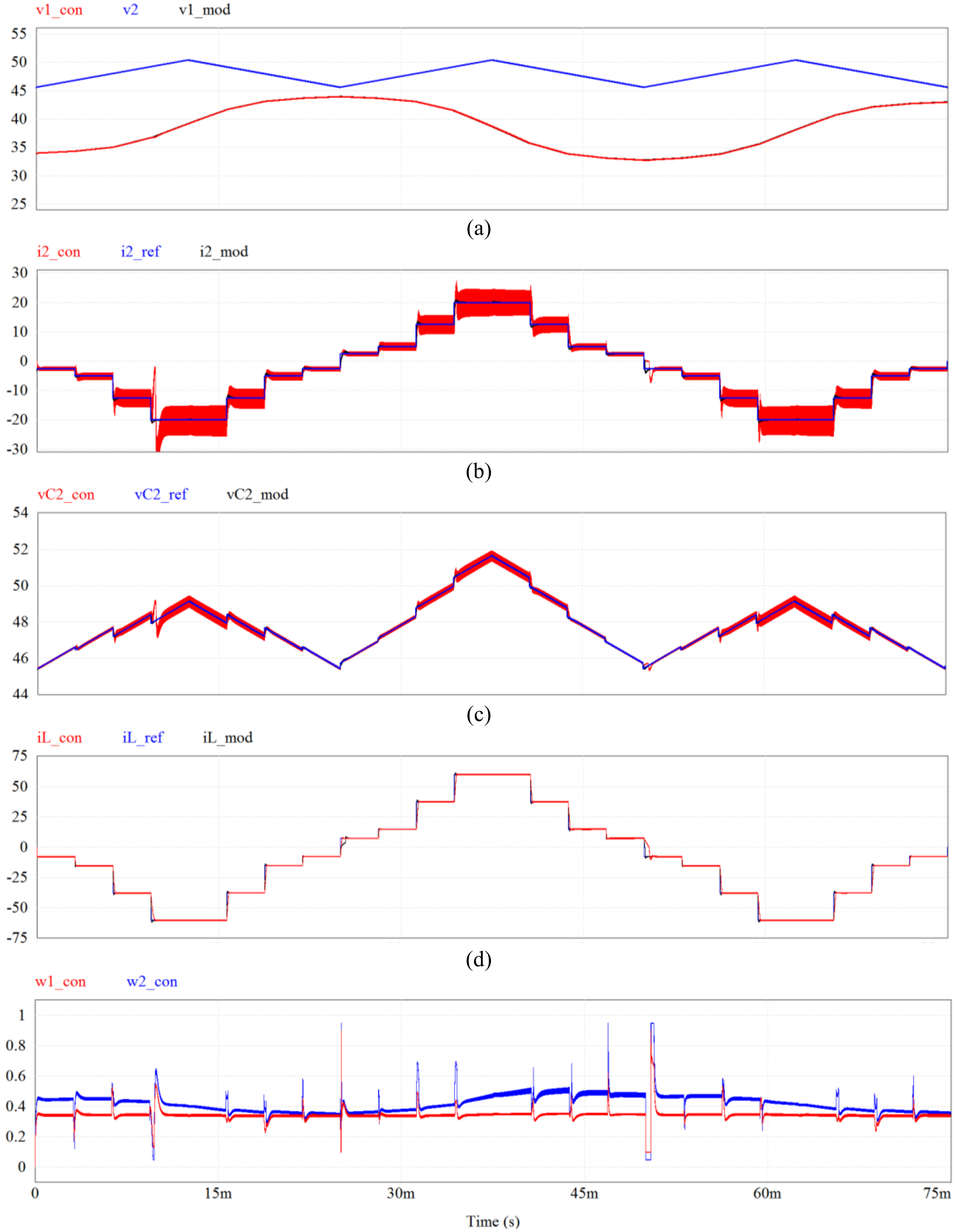

(e)

Figure 2.18 – Waveforms with the switched converter in the Tri-state Boost mode: a) Input and output voltages (in Volts); b) Reference and output current (in Amps); c) Reference and output capacitor voltage (in Volts); d) Reference and inductor current (in Amps); e) Control variables

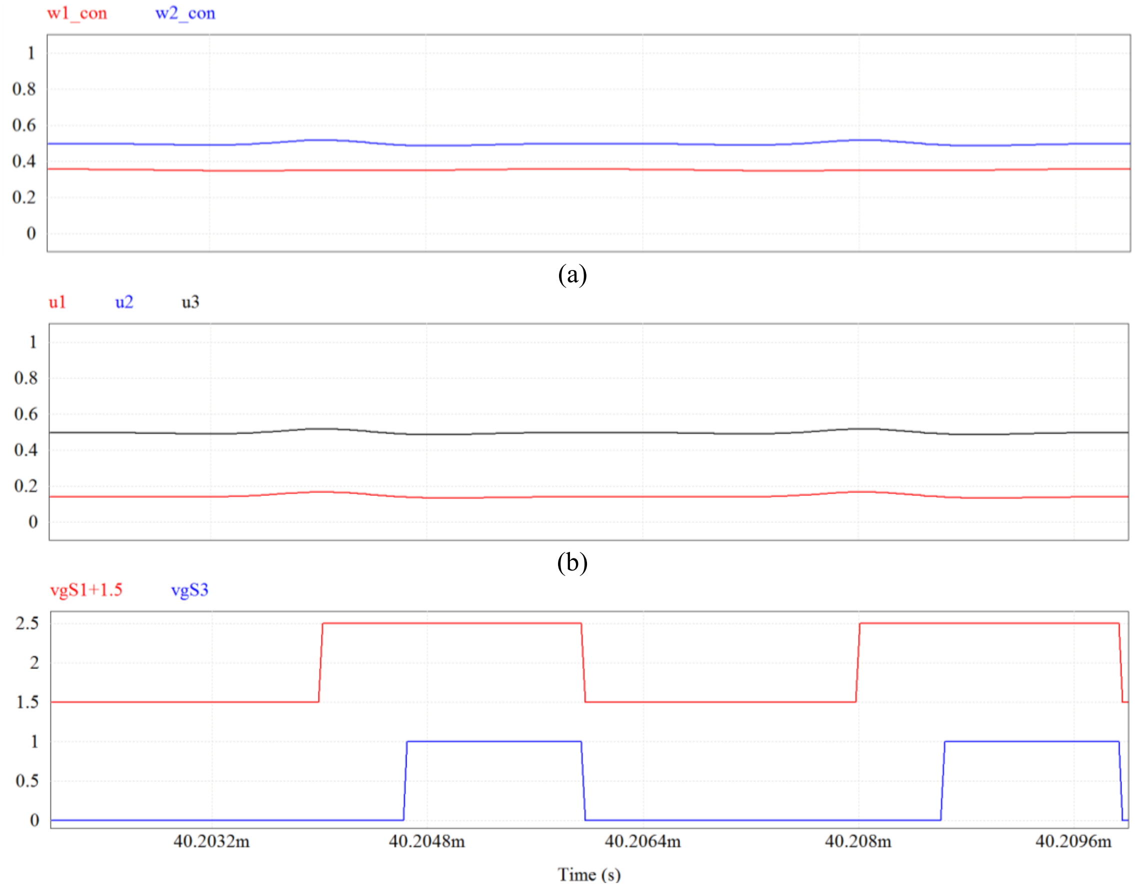

(a)

(b)

(c)

Figure 2.19 – Waveforms with the switched converter in the Tri-state Boost mode:
a) Control variables; b) Modulation signals; c) Gating signals of switches S_1 and S_3

2.6.3 Comparison to a Conventional Technique

The performance of the proposed unified controller for multi-state operation will be compared with a conventional technique. In this case, it concerns the 4-switch Bidirectional DC-DC converter operating with Dual-state in the Buck-Boost mode (mode 2 in Table 2.2). The output current (i_2) is controlled with a single loop employing a standard PI-controller. This is designed considering a model of the plant linearized around a certain operating point. The transfer function relating the injected current (i_2) to the duty cycle (D) of the converter is the following:

$$\frac{i_2(s)}{D(s)} = \frac{1}{R_2 L C_2}\left[\frac{(V_{C1}+V_{C2})-(I_L L)s}{s^2+\left(\frac{1}{R_2 C_2}\right)s+\frac{(1-D)^2}{L C_2}}\right] \tag{2.26}$$

One can clearly see that the system presents non-minimal phase when $I_L > 0$. A linear PI-controller was designed for the current loop considering $V_{C1} = V_{C2} = 48$ V, $D = 0.5$ and $I_L = 40$ A.

Because of the RHP zero at 4.7 kHz, the bandwidth of the control loop should be about 20% of that, thus it was selected as 1 kHz with a phase margin of 60°. A first order LPF of 25 kHz was employed at the sensed output current signal. The parameters of the current loop PI-controller are: $k_i = 5.1\text{m}$, $\tau_i = 918\ \mu\text{s}$, $f_{pi} = 5.8$ kHz.

The conventional technique was used in the switched converter for the test case presented in Figure 2.11. The capacitance of the SC is 15 mF and the DC-bus voltage (v_2) presents an average value of 48 V and a +/-5% triangular ripple of 40 Hz. Figure 2.20(a) shows the SC voltage and the DC-bus voltage on the top. Figure 2.20(b) at the bottom shows the staircase reference output current along with the current obtained with the proposed, index “con” and the traditional, index “trad” control schemes. In this case, the filtered (25 kHz) output current signals are shown, so that one can better observe the difference between the two responses. There one can see that the response of the traditional PI-controller presents longer settling times than the proposed scheme, and sometimes it fails to track the reference current. This is because the PI-controller was designed for operation close to a certain operating point. Figure 2.21 shows the response of the two controllers when both the input and the output voltages are 48 V, the values used in the model of the plant and design of the traditional PI-controller. There one can see that the proposed and the conventional control techniques perform equally well.

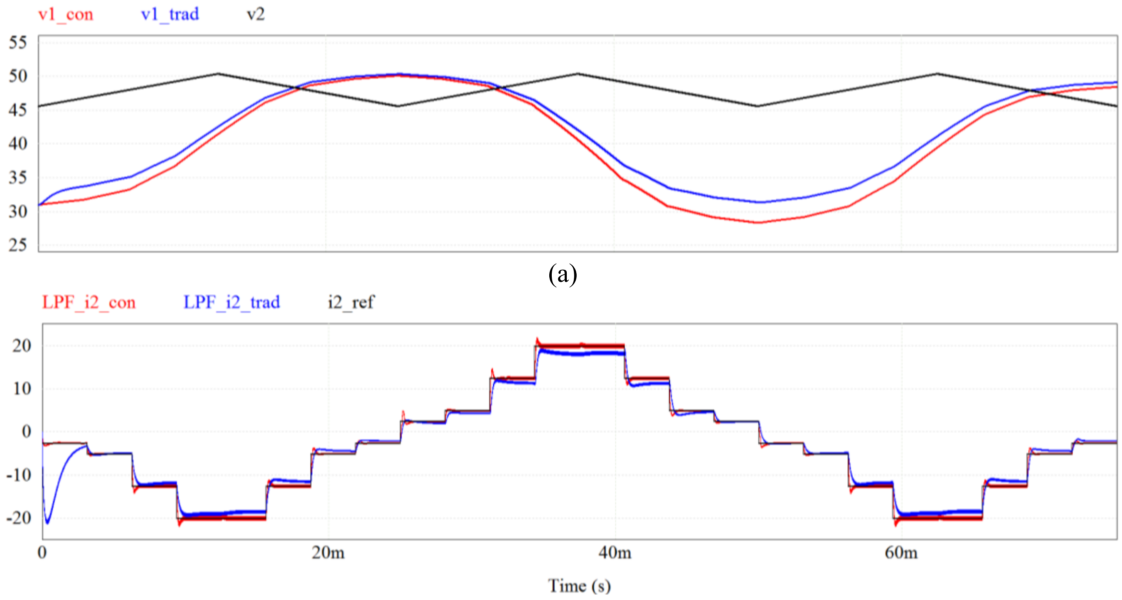

(a)

(b)

Figure 2.20 – Waveforms with the proposed unified multi-state controller and the traditional dual-state Buck-Boost controller for the SC interface to a DC grid: a) the input and output voltages (in Volts) for the two cases b) Reference and output currents (in Amps) for the two cases

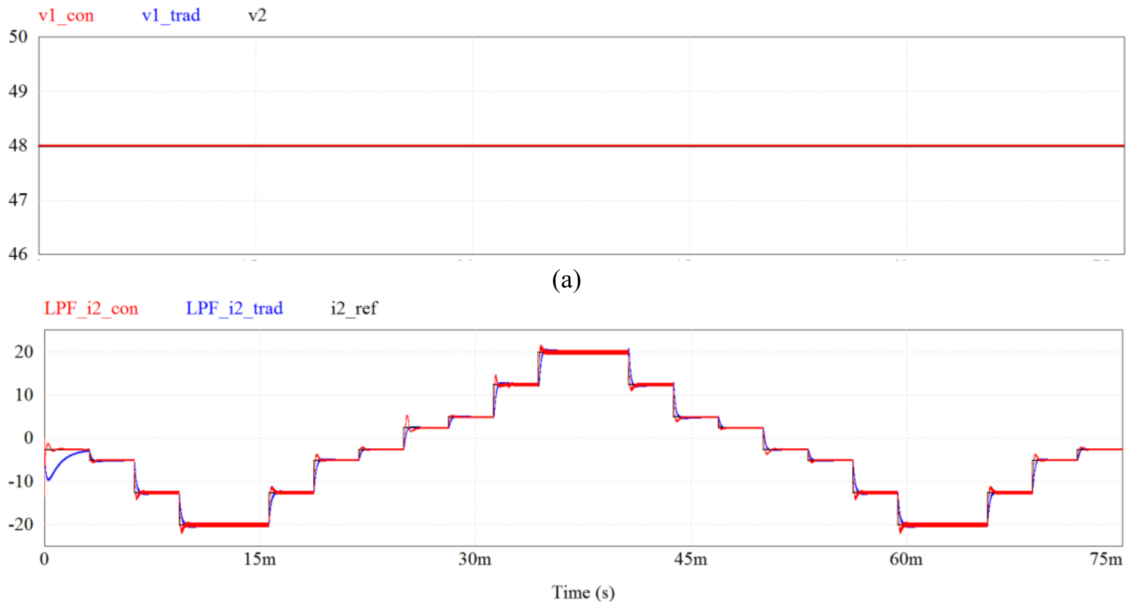

(b)

Figure 2.21 – Waveforms with the proposed unified multi-state controller and the traditional dual-state Buck-Boost controller for two 48 V regulated DC-buses: a) the input and output voltages (in Volts) for the two cases b) Reference and output currents (in Amps) for the two cases

2.6.4 Discussion of Results

The first test shown in Section 2.6.1 for the 4-switch Bidirectional Buck-Boost DC-DC converter interfacing the SC to a DC-grid, considered the mathematical model of the converter and the control laws for control variables w_1 and w_2. The resulting waveforms show that the proposed control scheme with multi-variable control and feedback linearization provides a very good transient response to step variations in the reference currents i_2* and i_L*. Besides, the load disturbance, represented by the triangular voltage ripple on the DC-bus, did not degrade the tracking of currents nor output voltage in steady-state. The dynamic responses with fixed PI-controllers was essentially the same despite the large variation in the SC voltage, 28 V to 50 V, and the reversal of the power flow direction. This is provided by the feedback linearization technique.

The second test shown in Section 2.6.2 considered the actual/switched bidirectional DC-DC converter, with the scheme for converting control variables w_1 and w_2, into PWM modulation signals u_1, u_2 and u_3, according to a selectable and desired multi-state mode of operation. The Quad-state and Tri-state Buck-Boost modes were used for the cases where the input voltage is smaller and larger than the output voltage. For the test with the Tri-state Buck and Tri-state Boost modes, the values of the SC and initial input voltage were adjusted so that the input voltage is always larger, for the Buck, and smaller, for the Boost, than the output or DC-grid voltage, considering the same reference output current and DC-bus voltage. It should be noted that, taking into account all these tests, the input voltage varied between 28 V and 58 V but the dynamic response of the proposed control scheme with fixed PI-controllers was essentially the same for all multi-state modes of operation.

The fact that the conventional current control scheme for a Dual-state Buck-Boost DC-DC converter with a single PI-controller works well when the operating conditions do not vary much was highlighted in Section 2.6.3. There it was shown that in applications such as the interface of a SC, with a wide voltage variation, to an unregulated DC-grid, the use of the proposed unified controller provides a better response in terms of dynamic response and tracking of the reference output current.

2.7 Chapter Conclusions

This chapter presented a unified controller for multi-state operation of the 4-switch Bidirectional Buck-Boost DC-DC converter suitable for interfacing SCs to DC-grids. According to the literature, multi-state operation of DC-DC converters allows the elimination of RHP zeros, switch power loss equalization, etc. The challenge of multi-variable control was tackled by employing feedback linearization and simple fixed PI-controllers. A mathematical model for designing the controllers and obtaining the control laws for the generic parameters (w_1 and w_2) was developed. These can be converted to three modulation signals (u_1, u_2 and u_3) and used in a carrier-based PWM scheme for generating the gating signals for five different multi-state modes of operation. The technique was verified by means of simulations in the interface of a SC operating in a wide range of voltages to a DC-bus with a +/-5% of voltage ripple. The same set of controllers provided fast and accurate regulation for step changes in the reference quantities under bi-directional power flow for the converter operating in Quad-state, Tri-state Buck-Boost, Tri-state Buck and Tri-state Boost modes.

3. The Novel 5-Switch Tapped-Inductor Multi-State Bidirectional DC-DC Converter

3.1 Chapter Introduction

In this Chapter, based on the previous limitations presented by the 4-switch converter employing the nonlinear controller based on feedback linearization, a novel bidirectional power electronics converter is proposed. It concerns a 5-switch DC-DC converter, based on a Tapped Inductor (TI), that presents voltage gains that vary as a function of the duty cycle (*D*) and the turns ratio (*n*) of the TI with Buck, Boost and Buck-Boost characteristics. Unlike previously reported DC-DC converters, this one allows reversal of the power flow without reversing the intermediate inductor current. This is beneficial since the inductor current, which is often used in the denominator of nonlinear control laws, will always be positive eliminating potential singularities.

Thus, this Chapter is organized in the following way: In Section 3.2, the novel 5-switch converter is introduced, where the working principle of the converter as well as the possible operating states/modes are presented and discussed in detail. Section 3.3, the steady-state analysis of some selected modes is discussed, where the main equations and theoretical waveforms are presented. In section 3.4, the impact of *n* into the voltage gain characteristic of the novel topology is assessed. Then, from section 3.5 to 3.7, an approach on how to select the value of *n* and operation modes for a given operation based on the power losses of the novel topology is discussed. Finally, the conclusions of this Chapter are stated in section 3.8.

3.2 The Novel 5-Switch Converter

As discussed in the last Chapters, SCs are devices that come in high capacitances and low voltages. It is possible to achieve higher voltage levels with the association of multiple SCs in series, but this should yield higher costs and complexity in order to assure voltage balancing across long arrays of SC cells. On the other hand, there is a trend for increasing the magnitude of the DC-bus voltage of Microgrids where, by doing so, the current drawn for a given power demand is reduced, thus reducing conduction losses and also reducing the size and weight of conductors. This presents a challenge for the connection of SCs to these systems. Therefore, a suitable power electronics topology that can present high voltage conversion characteristic is needed to interface SCs to high-voltage DC-buses in DC-Microgrids.

In this scenario, even presenting the Buck and Boost operation capability, the 4-switch converter discussed in the last Chapter is not suitable for applications where a high/low gain is required. This is due to the fact that this converter presents just the conventional Boost/Buck operation, where the voltage gain is defined just as a function of the duty cycle (*D*) of the controllable switch, in this case 1 / (1-*D*) for the Boost mode and *D* for the Buck mode.

This way, to deal with the voltage gain limitations of the previous topology, a new converter was proposed by [19]. In this new topology, switches S_2 and S_4 of the 4-switch converter are replaced by a single switch that taps the inductor. By employing a Tapped Inductor (TI), the voltage gain range of the converter is extended, where it will become a function of two parameters, the *D* of the controlled switch and the turns ratio (*n*) of the tapped inductor, meaning that the *D* of the converter at a certain operating point can be chosen according to the needs of the system, which means that an appropriate value can be determined based in the winding ratio of the inductor, where the converter will work with higher efficiency and the utilization of the circuit components is optimal [55]-[59]. Also, high or low voltage gains can be achieved with these TI-based topologies, presenting low components cost and relatively high efficiency. Talking specifically about *D* range extension for high/low voltage gains, TI-converters are regarded to present the best weight, size, complexity and cost associated when compared with other methods used to the same purpose (such as the cascading of converters, the use of multi-winding transformers and quadratic converters) [55]-[59].

However, [20] and [60] showed that the 3-switch TI converter proposed by [19] presents some limitations regarding the speed of its current/power flow control, since the power flow direction is based on the direction of the current flowing in the magnetizing inductance of the TI. Also, by removing a switch when compared with the 4-switch converter, the switching schemes available for this converter and consequently the use of multi-state operations is limited, and concerns regarding the RHP zero and the aging of components plays again a role in the implementation of this converter [20] [60].

Figure 3.1 shows the power electronics converter proposed in this Thesis and discussed in this Chapter. It consists of 5 power switches and a TI interfacing two DC-elements. One of the main features of this converter is a high voltage gain that can be achieved by adjusting the *n* of the TI. Besides, the direction of the power flow can be reversed without changing the direction of the intermediate inductor (magnetizing inductance) current (i_{LM}), which favors a faster dynamic response in case of power flow reversal.

For the proper operation of the power converter, switches S_1 to S_4 should be unidirectional in terms of current, such as those used in PWM Current Source Inverters (CSIs), which can be achieved by employing either IGBTs with reverse blocking capability or IGBTs/MOSFETs in series with a diode. Conversely, S_T (the switch that taps the inductor to the common node of the DC-buses) is a standard IGBT/MOSFET with anti-parallel body diode for bidirectional current flow. The TI is modeled as an ideal transformer with two windings (L_{T1} and L_{T2}) and a magnetizing inductance (L_M) in parallel with the primary winding, where the turns ratio of the windings, L_{T1}/L_{T2}, is $n/1$. Besides, it presents different operating states depending on the switching logic implemented, leading to controllable voltage gains (V_2/V_1) that vary with the control variable (the duty cycle D of the switches) with Buck, Boost and Buck-Boost characteristics. The choice of the turns ratio of the TI (n:1) affects the values of D that should be neither too small nor too large.

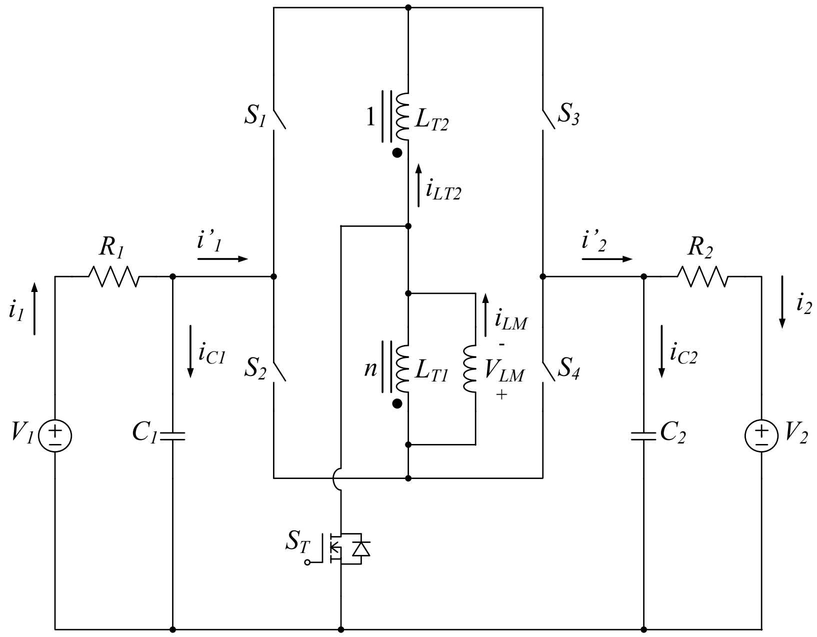

Figure 3.1 – The proposed 5-switch Bidirectional DC-DC Converter

For further analysis purposes, since this is a bidirectional topology and considering the circuit presented in Figure 3.1, it is assumed that, if the power flows from V_1 to V_2, meaning that i_1 and i_2 are positive, the converter operates in the Forward mode (P_{1to2}). On the other hand, if the power flows from V_2 to V_1, i_1 and i_2 are negative and the converter operates in the Reverse mode (P_{2to1}).

3.2.1 Forward Mode of Operation

Similar to the 4-switch converter presented and discussed in the last Chapter, the proposed 5-switch converter presents operating states that, when combined, make the converter operate with given features. For the operating states, the current path must be provided by two active switches. However, different from the 4-switch converter where the same operating states could be used for both power flow directions, each power flow direction presents operating states that can only be used for that specific condition/operation. This way, the operating states of the Forward mode of the novel 5-switch bidirectional converter are presented next in Figure 3.2.

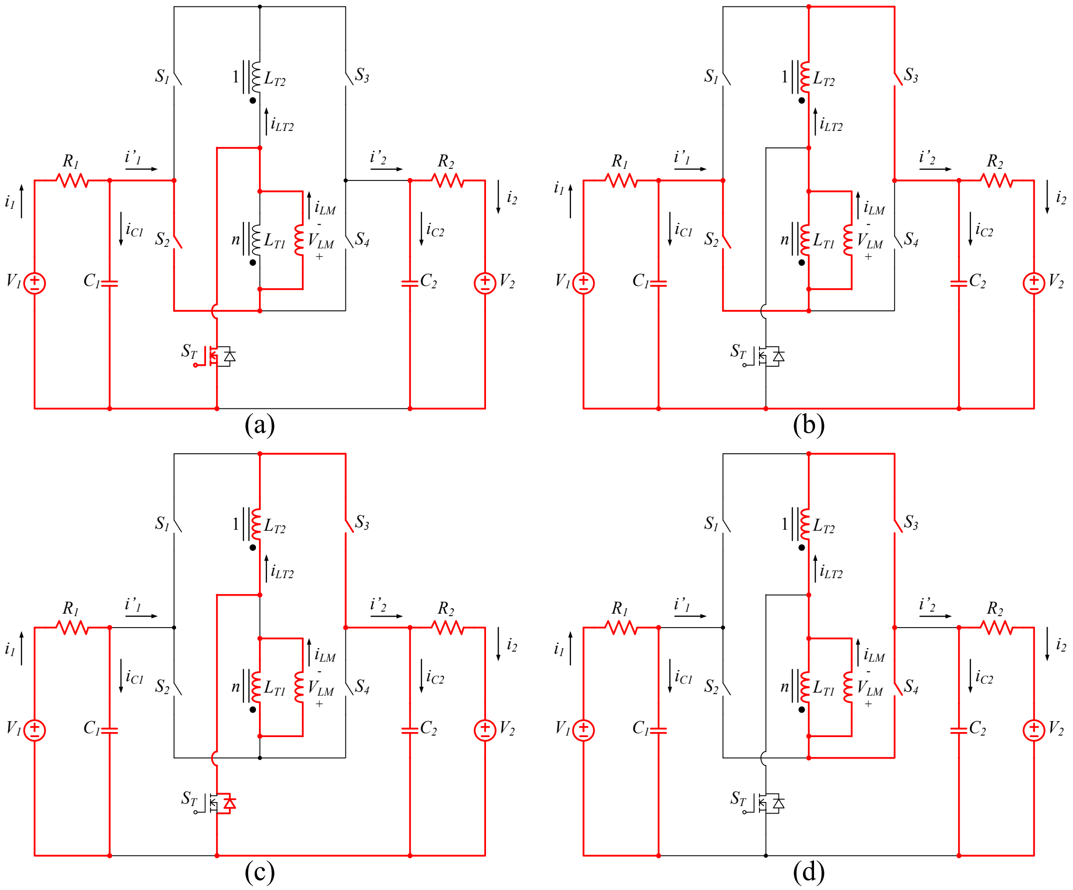

Figure 3.2 – Operating states of the Forward Mode for the proposed 5-switch Bidirectional DC-DC Converter

From KVL and KCL analysis of the operating states presented in Figure 3.2, the following can be determined:

- State S_{2T}: In this state, switches S_2 and S_T are ON. One can find that the voltage v_{LM} across the magnetizing inductance L_M is equal to v_{C1}. The current i'_1 is the magnetizing current i_{LM} and, since both switches S_3 and S_4 are OFF, the current i'_2 is equal to 0.

- State S_{23}: In this state, switches S_1 and S_3 are ON. One can find that the voltage v_{LM} across the inductance L_M is equal to $[n\ (v_{C1} - v_{C2})] / (n+1)$. For this state, since the energy is transferred directly from one voltage source to the other, current i'_1 and i'_2 present the same magnitude, which is $[n\ (i_{LM})] / (n+1)$.
- State S_{3T}: In this state, only switch S_3 is ON, and the complimentary current path is provided by the antiparallel body-diode of switch S_T. From this operating state, one can find that the voltage v_{LM} across the inductance L_M is equal to $-nv_{C2}$. Now, since both switches S_1 and S_2 are OFF, the current i'_1 is equal to 0, and the current i'_2 is ni_{LM}, which is the reflected current from the magnetizing inductance.
- State S_{34}: In this state, switches S_3 and S_4 are ON. This is called as the Forward free-wheeling operating state. For this state, the voltage v_{LM} is equal to 0V, and both currents i'_1 and i'_2 are also 0A.

Based on the analysis of the operating states presented above, the main aspects of each operating state are summarized next in Table 3.1.

Table 3.1 – Summarization of the Forward operating states for the novel 5-switch Bidirectional DC-DC Converter

State	i'_1	i'_2	v_{LM}	**Current Path**	**Power Flow**
S_{2T}	i_{LM}	0	$v_{C1} > 0$	S_2 and S_T	V_1 to inductor
S_{23}	$(n\ i_{LM})/(n+1)$	$(n\ i_{LM})/(n+1)$	$(n\ v_{C1} - n\ v_{C2})/(n+1)$	S_2 and S_3	V_1 to V_2
S_{3T}	0	$n\ i_{LM}$	$-n\ v_{C2}$	S_3 and $D(S_T)$	Inductor to V_2
S_{34}	0	0	0	S_3 and S_4	Free-wheeling (fw)

Then, from the combination of the possible operating states, the novel 5-switch bidirectional converter can present up to 8 different operating modes for the Forward power flow. Note that, since the 5-switch converter is an extension of the 3-switch converter (which was already a TI version of the 4-switch converter), these modes are similar to the ones from Chapter 2.

Table 3.2 – Forward operating modes for the novel 5-switch Bidirectional DC-DC Converter

States	**Mode of Operation**
S_{23}-S_{3T}	1 – Forward Dual-State Buck
S_{2T}-S_{23}	2 – Forward Dual-State Boost
S_{2T}-S_{3T}	3 – Forward Dual-State Buck-Boost
S_{23}-S_{3T}-S_{34}	4 – Forward Tri-State Buck with Free-wheeling (fw)
S_{2T}-S_{23}-S_{34}	5 – Forward Tri-State Boost with fw
S_{2T}-S_{3T}-S_{34}	6 – Forward Tri-State Buck-Boost with fw
S_{2T}-S_{23}-S_{3T}	7 – Forward Tri-State Buck-Boost with no fw
S_{2T}-S_{23}-S_{3T}-S_{34}	8 – Forward Quad-State Buck-Boost

3.2.2 Reverse Mode of Operation

Now, for the Reverse mode, the possible operating states are presented next in Figure 3.3. They are very similar to the ones from the Forward mode, where the main difference between these modes is that switches S_2 and S_3 are the ones used for the Forward mode, while S_1 and S4 are the main switches for the Reverse mode, with S_T being the only switch used for both modes.

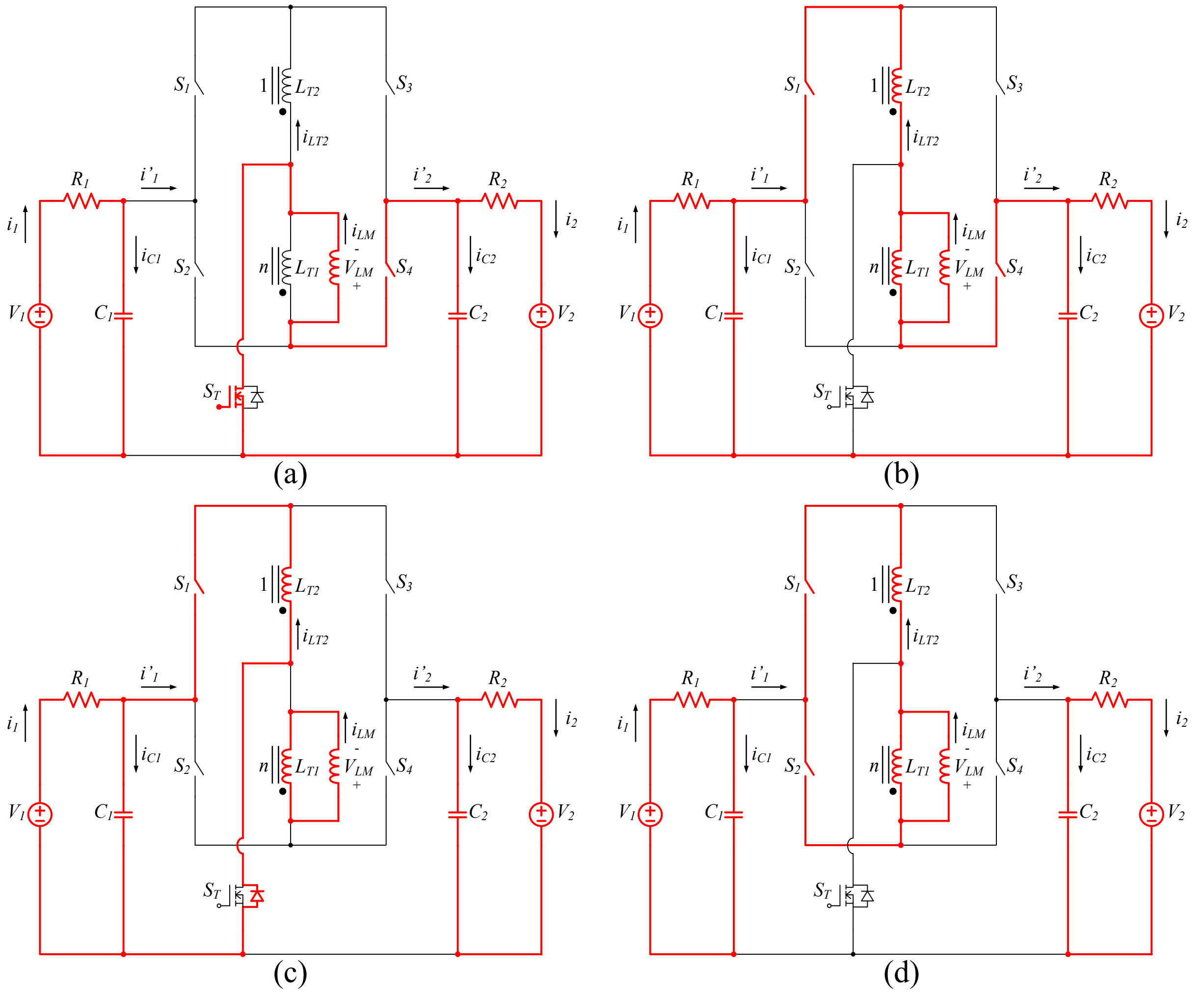

Figure 3.3 – Operating states of the Reverse Mode for the proposed 5-switch Bidirectional DC-DC Converter

Similar to the Forward operation, from KVL and KCL analysis of the operating states presented in Figure 3.3, the following can be determined, where the main aspects of each operating state are summarized in Table 3.3.

- State S_{4T}: In this state, switches S_4 and S_T are ON. One can find that the voltage v_{LM} across the magnetizing inductance L_M is equal to v_{C2}. The current i'_2 is the negative magnetizing current ($-i_{LM}$) and, since both switches S_1 and S_2 are OFF, the current i'_1 is equal to 0.

- State S_{14}: In this state, switches S_1 and S_4 are ON. One can find that the voltage v_{LM} across the inductance L_M is equal to $[n\ (v_{C2} - v_{C1})] / (n+1)$. For this state, the energy is transferred directly from V_2 to V_1, currents i'_1 and i'_2 present the same magnitude, which is in this case $[-n\ (i_{LM})]/(n+1)$.
- State S_{1T}: In this state, only switch S_1 is ON, and the complimentary current path is provided by the antiparallel body-diode of switch S_T. From this operating state, one can find that the voltage v_{LM} across the inductance L_M is equal to $-nv_{C1}$. Now, with switches S_3 and S_4 turned OFF, the current i'_2 is equal to 0, and the current i'_1 is the reflected current from the magnetizing inductance ($-ni_{LM}$).
- State S_{12}: In this state, switches S_1 and S_2 are ON. This is called as the Reverse Free-wheeling operating state. For this state, the voltage v_{LM} is equal to 0V, and both currents i'_1 and i'_2 are also 0A.

Based on the analysis of the operating states presented above, the main aspects of each operating state are summarized next in Table 3.3.

Table 3.3 – Summarization of the Reverse operating states for the novel 5-switch Bidirectional DC-DC Converter

State	i'_1	i'_2	v_L	Current Path	Power Flow
S_{4T}	0	$-i_{LM}$	$v_{C2} > 0$	S_4 and S_T	V_2 to inductor
S_{14}	$(-n\ i_{LM})/(n+1)$	$(-n\ i_{LM})/(n+1)$	$(n\ v_{C2} - n\ v_{C1})/(n+1)$	S_1 and S_4	V_2 to V_1
S_{1T}	$-n\ i_{LM}$	0	$-n\ v_{C1}$	S_1 and $D(S_T)$	Inductor to V_1
S_{12}	0	0	0	S_1 and S_2	Free-wheeling (fw)

Then, with the combination of the operating states presented in Table 3.3, the Reverse mode can also present up to 8 different operating modes. These modes are presented next in Table 3.4, where one sees that these modes are basically the same as the ones from the Forward mode. However, one should note that now the terms Buck, Boost and Buck-Boost relate to the magnitudes of V_2 to V_1, while for the Forward mode relates to the opposite, which is V_1 to V_2.

Table 3.4 – Reverse operating modes for the novel 5-switch Bidirectional DC-DC Converter

States	Mode of Operation
S_{14}-S_{1T}	1 – Reverse Dual-State Buck
S_{4T}-S_{14}	2 – Reverse Dual-State Boost
S_{4T}-S_{1T}	3 – Reverse Dual-State Buck-Boost
S_{14}-S_{1T}-S_{12}	4 – Reverse Tri-State Buck with Free-wheeling (fw)
S_{4T}-S_{14}-S_{12}	5 – Reverse Tri-State Boost with fw
S_{4T}-S_{1T}-S_{12}	6 – Reverse Tri-State Buck-Boost with fw
S_{4T}-S_{14}-S_{1T}	7 – Reverse Tri-State Buck-Boost with no fw
S_{4T}-S_{14}-S_{1T}-S_{12}	8 – Reverse Quad-State Buck-Boost

3.3 Steady-State Analysis of Dual-State Modes

Since it would be unfeasible to present the analysis of all operating modes presented in Tables 3.2 and 3.4, just the analysis of the Dual-state operations are presented next in this Thesis in order to highlight some of the features of this new topology. The main reason for that is that these modes already present the 3 mains operating states for each power flow direction: S_{23}, S_{2T} and S_{3T} for the Forward modes; and S_{1T}, S_{14} and S_{4T} for the Reverse modes.

In order to determine the modes to be presented/analyzed, it is assumed that V_1 will be the high-voltage side and $V2$ the low one. Based on this assumption, the converter can operate in 4 different Dual-State modes: 2 for the Forward mode and 2 for the Reverse mode. They are: Buck and Buck-Boost modes for the Forward case, and Boost and Buck-Boost for the Reverse case. Their analysis is presented next.

3.3.1 Forward Dual-State Buck

For the Forward Dual-State Buck mode, switch S_3 in ON during all the switching period, whereas switches S_2 is PWM controlled. During the first operating state (S_{23}), switches S_2 and S_3 are ON, and the duration of this operating state is defined by the duty cycle D_{2T}, which is the duty cycle of switch S_2. From this state, the following equations for the current through the ON switches and the voltage of the OFF switch can be found to be:

$$i_{S2} = \frac{n(i_{LM})}{n+1} \tag{3.1}$$

$$i_{S3} = \frac{n(i_{LM})}{n+1} \tag{3.2}$$

$$v_{ST} = v_{C1} - V_{LM} \tag{3.3}$$

For the second operating state (S_{3T}), switch S_3 remains ON, switch S_2 is turned OFF and the current finds a path through the antiparallel body-diode of S_T. Now, the equations that define this state are presented from (3.4) to (3.6).

$$i_{S3} = n(i_{LM}) \tag{3.4}$$

$$i_{ST} = -n(i_{LM}) \tag{3.5}$$

$$v_{S2} = v_{C1} - V_{LM} \tag{3.6}$$

From the previous equations, one sees that all the currents and voltages of the semiconductors are directly related to the values across the magnetizing inductance. This way, knowing how this inductance behaves and the theoretical waveforms of it is of high importance. From the analysis of the Forward Dual-State Buck mode, one can draw the theoretical waveforms for the voltage and current across the magnetizing inductance L_M. This is presented by Figure 3.4.

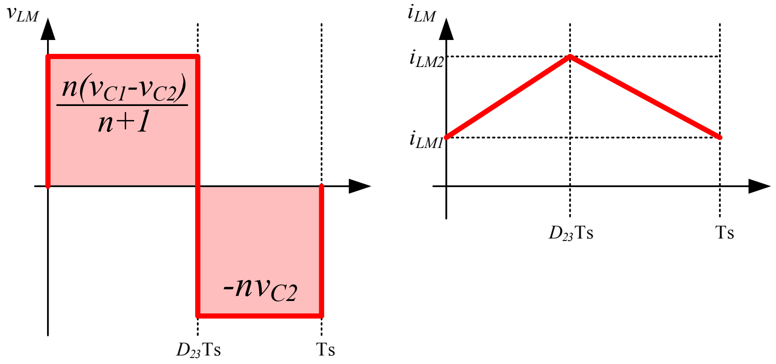

Figure 3.4 – Forward Dual-State Buck: Theoretical waveforms of the magnetizing inductance

Then, based on Figure 3.4, one can find (3.7), which is the equation that depict the average values of the magnetizing voltage within a switching period.

$$V_{LM}=\left[\frac{n(v_{C1}-v_{C2})}{n+1}\right]D_{23}+(-nv_{C2})(1-D_{23}) \tag{3.7}$$

By considering the average value of v_{LM} to be zero in steady-state, one obtains the voltage conversion characteristic of this mode as (3.8).

$$\frac{v_{C2}}{v_{C1}}=\frac{D_{23}}{n+1-nD_{23}} \tag{3.8}$$

Also, as can be seen from equations (3.1), (3.2), (3.4) and (3.5), the switch currents are a function of the magnetizing current, i_{LM}. Therefore, with the theoretical waveform of i_{LM} presented in Figure 3.4, one can define the time equation for the switch currents as the following:

$$i_{S2}(t)=\begin{cases}\left[\frac{n(i_{LM2}-i_{LM1})}{(n+1)D_{23}T_S}\right]t+\left[\frac{ni_{LM1}}{(n+1)}\right], & 0\le t\le D_{23}T_S\\ 0, & D_{23}T_S\le t\le T_S\end{cases} \tag{3.9}$$

$$i_{S3}(t)=\begin{cases}\left[\frac{n(i_{LM2}-i_{LM1})}{(n+1)D_{23}T_S}\right]t+\left[\frac{ni_{LM1}}{(n+1)}\right], & 0\le t\le D_{23}T_S\\ \left[\frac{n(i_{LM1}-i_{LM2})}{(1-D_{23})T_S}\right]t+\left[\frac{n(i_{LM2}-i_{LM1}D_{23})}{(1-D_{23})}\right], & D_{23}T_S\le t\le T_S\end{cases} \tag{3.10}$$

$$i_{ST}(t) = \begin{cases} 0, & 0 \leq t \leq D_{23}T_S \\ -\left[\dfrac{n(i_{LM1} - i_{LM2})}{(1 - D_{23})T_S}\right]t - \left[\dfrac{n(i_{LM2} - i_{LM1}D_{23})}{(1 - D_{23})}\right], & D_{23}T_S \leq t \leq T_S \end{cases} \tag{3.11}$$

Finally, the average value of the magnetizing current I_{LM}, and the equation for the sizing of the magnetizing inductance are presented next by equations (3.12) and (3.13), respectively, where: f_s is the switching frequency; P_c is the rated power and Δi_{LM} the inductor current ripple.

$$I_{LM} = \frac{(n+1)P_c}{nv_{C1}D_{23}} \tag{3.12}$$

$$L_M = \frac{n(v_{C1} - v_{C2})D_{23}}{(n+1)\Delta i_{LM}f_s} \tag{3.13}$$

3.3.2 Forward Dual-State Buck-Boost

For the Forward Buck-Boost mode, switch S_T in ON during all the switching period, whereas switches S_2 and S_3 are the ones PWM controlled. During the first operating state (S_{2T}), switches S_2 and S_T are ON, and the duration of this operating state D_{2T} is defined by the duty cycle of switch S_2, which is D_{2T}. From the analysis of this state, one can find the following equations for the current and voltage across the power semiconductors.

$$i_{S2} = i_{LM} \tag{3.14}$$

$$i_{ST} = i_{LM} \tag{3.15}$$

$$v_{S3} = -\left(\frac{V_{LM} + nv_{C2}}{n}\right) \tag{3.16}$$

For the second operating state (S_{3T}), switch S_T remains ON, switch S_2 is turned OFF and switch S_3 turns ON. Now, the equations that define this state are presented from (3.17) to (3.19). Note that both the Forward Buck and Forward Buck-Boost modes present the same second operating state.

$$i_{S3} = n(i_{LM}) \tag{3.17}$$

$$i_{ST} = -n(i_{LM}) \tag{3.18}$$

$$v_{S2} = v_{C1} - V_{LM} \tag{3.19}$$

As for the Forward Dual-State Buck mode, all the equations of the Forward Buck-Boost mode are functions of the voltage and current across the magnetizing inductance. This way, Figure 3.5

presents the theoretical waveforms of the voltage and current across the magnetizing inductance for the Forward Dual-State Buck-Boost mode.

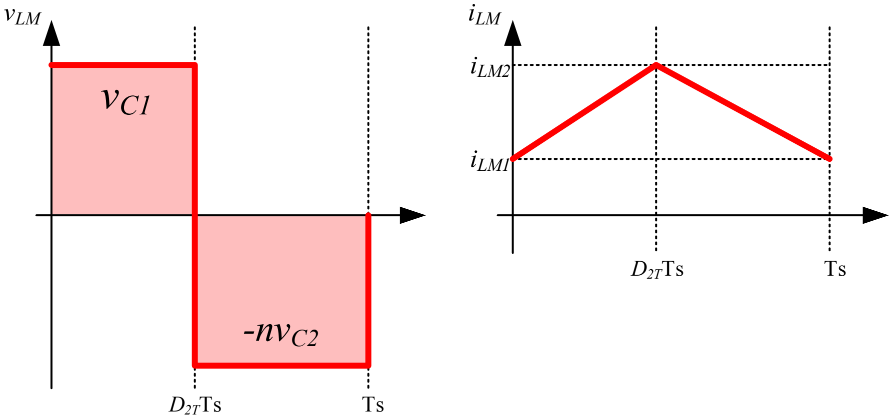

Figure 3.5 – Forward Dual-State Buck-Boost: Theoretical waveforms of the magnetizing inductance

Based on Figure 3.5, one can find the following equation that depicts the average voltage value of the magnetizing inductance within a switching period.

$$V_{LM} = (v_{C1})(D_{2T}) + (-nv_{C2})(1 - D_{2T}) \tag{3.20}$$

From (3.20) and, by considering the average value of v_{LM} to be zero in steady-state, one obtains the voltage conversion characteristic of the Forward Dual-State Buck-Boost mode in (3.21).

$$\frac{v_{C2}}{v_{C1}} = \frac{D_{2T}}{n(1 - D_{2T})} \tag{3.21}$$

Similar to the previous mode, the time equations for the switch currents for the Forward Dual-State Buck-Boost mode can be found from the theoretical waveform of the magnetizing inductance current, i_{LM}. They are presented next from (3.22) to (3.24).

$$i_{S2}(t) = \begin{cases} \left[\dfrac{(i_{LM2} - i_{LM1})}{D_{2T}T_S}\right] t + i_{LM1}, & 0 \le t \le D_{2T}T_S \\ 0, & D_{2T}T_S \le t \le T_S \end{cases} \tag{3.22}$$

$$i_{S3}(t) = \begin{cases} 0, & 0 \le t \le D_{2T}T_S \\ \left[\dfrac{n(i_{LM1} - i_{LM2})}{(1 - D_{2T})T_S}\right] t + \left[\dfrac{n(i_{LM2} - i_{LM1}D_{2T})}{(1 - D_{2T})}\right], & D_{2T}T_S \le t \le T_S \end{cases} \tag{3.23}$$

$$i_{ST}(t) = \begin{cases} \left[\dfrac{(i_{LM2} - i_{LM1})}{D_{2T}T_S}\right] t + i_{LM1}, & 0 \le t \le D_{2T}T_S \\ -\left[\dfrac{n(i_{LM1} - i_{LM2})}{(1 - D_{2T})T_S}\right] t - \left[\dfrac{n(i_{LM2} - i_{LM1}D_{2T})}{(1 - D_{2T})}\right], & D_{2T}T_S \le t \le T_S \end{cases} \tag{3.24}$$

The average value of the magnetizing current and the equation for the sizing of the magnetizing inductance for the Forward Dual-State Buck-Boost mode are presented next by equations (3.25) and (3.26), respectively.

$$I_{LM} = \frac{P_c}{v_{C1} D_{2T}} \tag{3.25}$$

$$L_M = \frac{v_{C1} D_{2T}}{\Delta i_{LM} f_s} \tag{3.26}$$

3.3.3 Reverse Dual-State Boost

For the Reverse Boost mode, switch S_4 in ON during all the switching period, whereas switches S_1 and S_T are PWM controlled. During the first operating state (S_{4T}), switches S_4 and S_T are ON, and the duration of this operating state (D_{4T}) is defined by the duty cycle of switch S_T. From the analysis of this state, the following equations can be found.

$$i_{S4} = i_{LM} \tag{3.27}$$

$$i_{ST} = i_{LM} \tag{3.28}$$

$$v_{S1} = \frac{-(n v_{C1} + V_{LM})}{n} \tag{3.29}$$

For the second operating state (S_{14}), switch S_4 remains ON, switch S_T is turned OFF and switch S_1 turns ON. Now, the equations that define the current and voltage across the power semiconductors are presented from (3.30) to (3.32).

$$i_{S1} = \frac{n(i_{LM})}{n+1} \tag{3.30}$$

$$i_{S4} = \frac{n(i_{LM})}{n+1} \tag{3.31}$$

$$v_{ST} = v_{C2} - V_{LM} \tag{3.32}$$

Following the same steps from the previous operating modes of the Forward operation, one can find see the theoretical waveforms for the magnetizing inductance of the Reverse Dual-State Boost mode in Figure 3.6. Also, the equation for the average value of the magnetizing voltage in a switching period can be seen in (3.33) and, after considering the steady-state value of v_{LM} to be 0, the voltage conversion characteristic of this mode in (3.34).

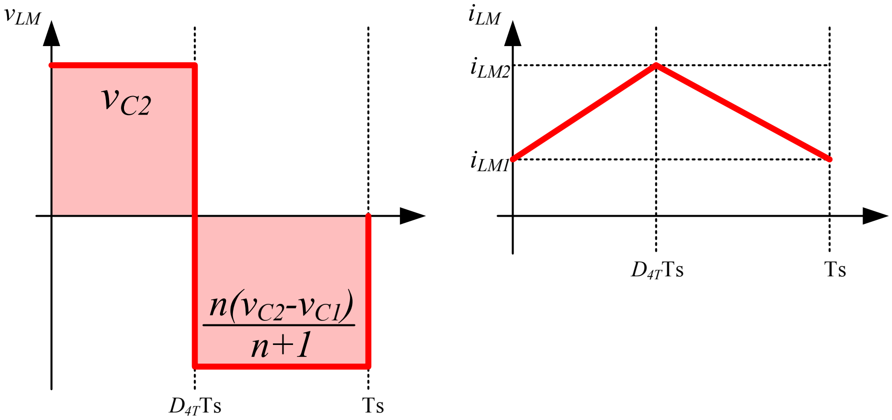

Figure 3.6 – Reverse Dual-State Boost: Theoretical waveforms of the magnetizing inductance

$$V_{LM} = (v_{C2})(D_{4T}) + \left[\frac{n(v_{C2} + v_{C1})}{n+1}\right](1 - D_{4T}) \tag{3.33}$$

$$\frac{v_{C2}}{v_{C1}} = \frac{n(1 - D_{4T})}{n + D_{4T}} \tag{3.34}$$

Next, from equations (3.35) to (3.37), the time equation for the switch currents of this mode based on Figure 3.6 are presented.

$$i_{S1}(t) = \begin{cases} 0, & 0 \le t \le D_{4T}T_S \\ \left[\frac{n(i_{LM1} - i_{LM2})}{(n+1)(1 - D_{4T})T_S}\right]t + \left[\frac{n(i_{LM2} - i_{LM1}D_{4T})}{(n+1)(1 - D_{4T})}\right], & D_{4T}T_S \le t \le T_S \end{cases} \tag{3.35}$$

$$i_{S4}(t) = \begin{cases} \left[\frac{(i_{LM2} - i_{LM1})}{D_{4T}T_S}\right]t + i_{LM1}, & 0 \le t \le D_{4T}T_S \\ \left[\frac{n(i_{LM1} - i_{LM2})}{(n+1)(1 - D_{4T})T_S}\right]t + \left[\frac{n(i_{LM2} - i_{LM1}D_{4T})}{(n+1)(1 - D_{4T})}\right], & D_{4T}T_S \le t \le T_S \end{cases} \tag{3.36}$$

$$i_{ST}(t) = \begin{cases} \left[\frac{(i_{LM2} - i_{LM1})}{D_{4T}T_S}\right]t + i_{LM1}, & 0 \le t \le D_{4T}T_S \\ 0, & D_{4T}T_S \le t \le T_S \end{cases} \tag{3.37}$$

The average value of the magnetizing current and the equation for the sizing of the magnetizing inductance for the Forward Dual-State Buck-Boost mode are presented next by (3.38) and (3.39).

$$I_{LM} = \frac{(n+1)P_c}{v_{C2}(n + D_{4T})} \tag{3.38}$$

$$L_M = \frac{v_{C2}D_{4T}}{\Delta i_{LM} f_s} \tag{3.39}$$

3.3.4 Reverse Dual-State Buck-Boost

For the Reverse Dual-State Buck-Boost mode, switch S_T is ON during all the switching period, whereas switches S_1 and S_4 are PWM controlled. During the first operating state (S_{4T}), switches S_4 and S_T are ON, and the duration of this operating state (D_{4T}) is defined by the duty cycle of switch S_4. From the analysis of this state, (3.40)-(3.42) are defined. Note that now the Reverse modes present the same first operating state, but not the second ones like the Forward operation.

$$i_{S4} = i_{LM} \tag{3.40}$$

$$i_{ST} = i_{LM} \tag{3.41}$$

$$v_{S1} = \frac{-(nv_{C1} + V_{LM})}{n} \tag{3.42}$$

For the second operating state (S_{1T}), switch S_T remains ON, switch S_4 is turned OFF and switch S_1 turns ON. The equations for the current and voltage across the power semiconductors are presented from (3.43) to (3.45).

$$i_{S1} = n(i_{LM}) \tag{3.43}$$

$$i_{ST} = -n(i_{LM}) \tag{3.44}$$

$$v_{S4} = v_{C2} - V_{LM} \tag{3.45}$$

Figure 3.7 shows the theoretical waveforms of the voltage and current across L_M for the Reverse Dual-State Buck-Boost mode.

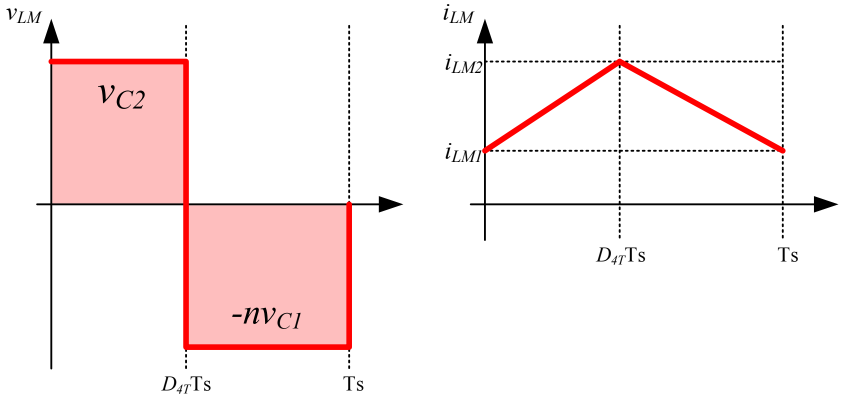

Figure 3.7 – Reverse Dual-State Buck-Boost: Theoretical waveforms of the magnetizing inductance

From Figure 3.7, one can find in (3.46) the equation that depicts the average values of the magnetizing voltage within a switching period. Finally, the voltage conversion characteristic of the converter operating in the Reverse Dual-State Buck-Boost mode is presented in (3.47).

$$V_{LM} = (v_{C2})(D_{4T}) + (-nv_{C1})(1 - D_{4T}) \tag{3.46}$$

$$\frac{v_{C2}}{v_{C1}} = \frac{n(1 - D_{4T})}{D_{4T}} \tag{3.47}$$

The time equation for the switch currents of the Reverse Dual-State Buck-Boost mode based are presented next in (3.48)-(3.50).

$$i_{S1}(t) = \begin{cases} 0, & 0 \leq t \leq D_{4T}T_S \\ \left[\frac{n(i_{LM1} - i_{LM2})}{(1 - D_{4T})T_S}\right]t + \left[\frac{n(i_{LM2} - i_{LM1}D_{4T})}{(1 - D_{4T})}\right], & D_{4T}T_S \leq t \leq T_S \end{cases} \tag{3.48}$$

$$i_{S4}(t) = \begin{cases} \left[\frac{(i_{LM2} - i_{LM1})}{D_{4T}T_S}\right]t + i_{LM1}, & 0 \leq t \leq D_{4T}T_S \\ 0, & D_{4T}T_S \leq t \leq T_S \end{cases} \tag{3.49}$$

$$i_{ST}(t) = \begin{cases} \left[\frac{(i_{LM2} - i_{LM1})}{D_{4T}T_S}\right]t + i_{LM1}, & 0 \leq t \leq D_{4T}T_S \\ -\left[\frac{n(i_{LM1} - i_{LM2})}{(1 - D_{4T})T_S}\right]t - \left[\frac{n(i_{LM2} - i_{LM1}D_{4T})}{(1 - D_{4T})}\right], & D_{4T}T_S \leq t \leq T_S \end{cases} \tag{3.50}$$

Finally, the average value of the magnetizing current, I_{LM}, and the equation for the sizing of the magnetizing inductance are for this mode are presented next by equations (3.51) and (3.52), respectively.

$$I_{LM} = \frac{P_c}{v_{C2}D_{4T}} \tag{3.51}$$

$$L_M = \frac{v_{C2}D_{4T}}{\Delta i_{LM}f_s} \tag{3.52}$$

3.4 Voltage Conversion Characteristic

As stated before, one of the main advantages of TI topologies is the fact that the voltage conversion characteristic (*G*) for such topologies can be changed according to the system needs based on the *n* of the TI. To better illustrate that, Figures 3.8 and 3.9 are presented next, where one can see how the *G* of the converter for the Forward modes discussed in the last section change for the same *D* as *n* varies its value. Figure 3.8 shows the plotting of equation (3.8) whereas figure 3.9 presents the plotting of equation (3.21).

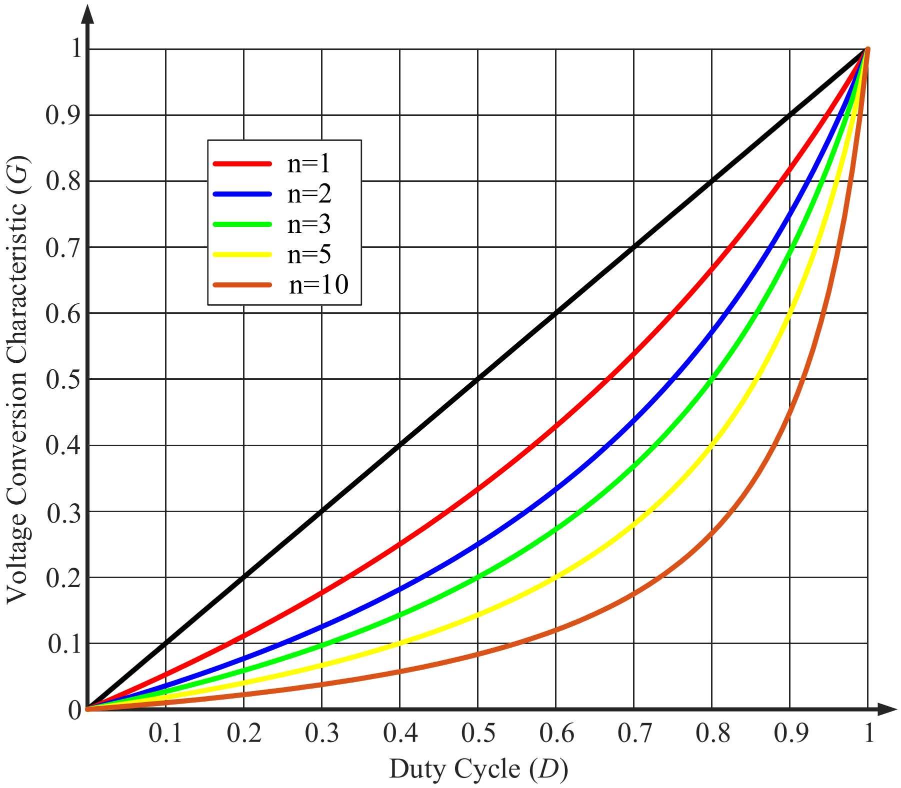

Figure 3.8 – Voltage conversion characteristic (*G*) of the Forward Dual-State Buck for different values of *n*

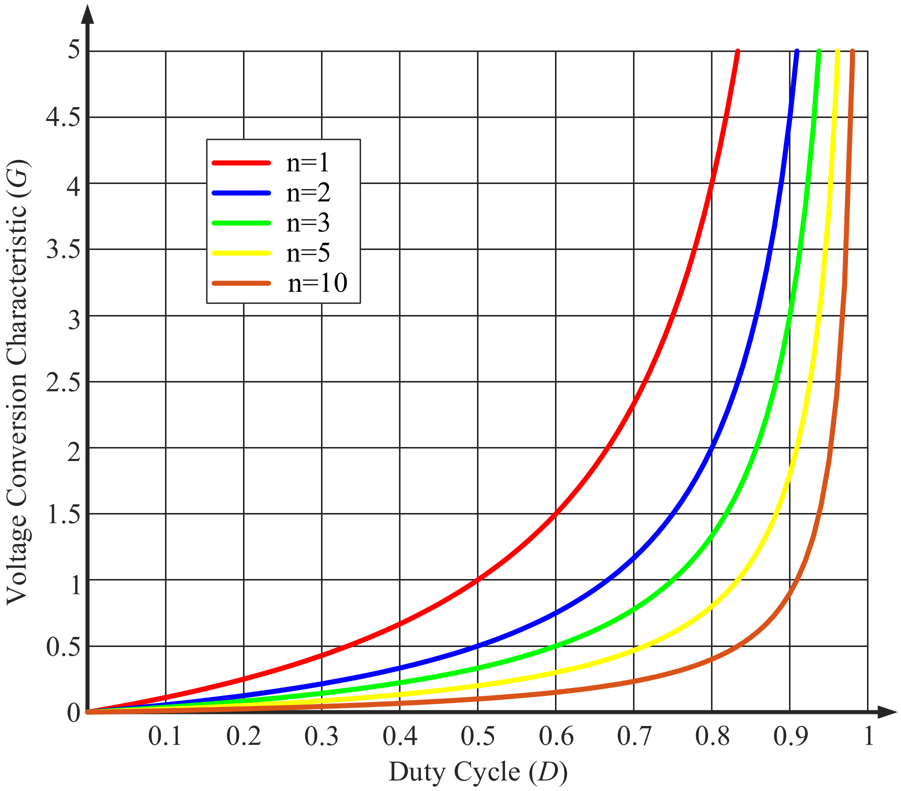

Figure 3.9 – Voltage conversion characteristic (*G*) of the Forward Dual-State Buck-Boost for different values of *n*

For the Dual-State Buck operation of the proposed converter, it is clearly presented in Figure 3.8 that, as the value of *n* increases, the 5-switch converter increases its capability of stepping-down a given voltage level. From this Figure, one sees that, for the traditional Buck operation, black curve in Figure 3.8, the converter presents the already known linear relation between the *G* and *D*, which is $G = D$. However, as *n* increases, one sees that that the converter can decrease the voltage even more. For example, for the traditional Buck operation, one needs $D = 0.5$ to obtain an output voltage with magnitude of half the input voltage. However, if one is employing the novel 5-switch converter with $n = 3$, green curve in Figure 3.8, one can have the same voltage gain for a $D = 0.8$ approximately.

Now, for the Forward Dual-State Buck-Boost, presented in Figure 3.9, one sees that, as *n* changes, the point where the converter changes its operation from being a step-down converter to a step-up also changes. For the traditional Buck-Boost operation, which happens for the proposed 5-switch converter if $n = 1$, this operating point is established when $D = 0.5$. However, for $n=3$, this point is moved forward for $D = 0.75$ approximately.

3.5 Power Loss Analysis for Turns Ratio and Modes of Operation Selection

As presented in the last sections, the value of *n* of the TI of the proposed converter plays a significant role on its operation. From the voltage conversion characteristic to all the switches currents, *n* will impact every aspect of the converter. However, there is still a lack of literature on how to properly select the value of *n* of the TI in such topologies. Usually, this is defined as a designer's choice, and aspects such how this choice was made and how it would impact significant aspects of the power topology, such as the overall efficiency of the system, are not well presented and discussed. Taking this into account, this thesis proposes a clear and well-oriented design approach to determine the value of *n* of a TI for the novel 5-switch bidirectional DC-DC based on the power losses analysis of the semiconductors, where an ideal value of *n* is defined in order for the converter to work with the highest possible efficiency for a given operating point. Also, since the discussed converter presents a variety of possible operating modes, this Thesis will address next how to select the modes of operation to be used for a given operation based on the choice of *n* and semiconductor losses.

For the power losses analysis of the converter, the two main sources of losses on the power semiconductors are taken into account: Conduction and switching losses.

For the conduction losses, recall that switches S_1 to S_4 must be unidirectional, and as mentioned previously, this can be done in two ways: either with IGBTs with reverse blocking capability or IGBTs/MOSFETs in series with a diode. For the power losses analysis, this Thesis will consider the later, with MOSFETS in series with diodes to realize the semiconductor switches (S_1 to S_4) that are unidirectional in current, while S_T concerns a MOSFET only. In terms of losses, this means that the conduction losses in such devices (S_1 to S_4) will be defined as the sum of the conduction losses in each semiconductor, while S_T follows the conventional losses calculation for a standard MOSFET. From the power semiconductor theory, one knows that:

$$Pcond_{MOSFET} = i_{S_{RMS}}{}^2 R_{DS} \tag{3.53}$$

$$Pcond_{Diode} = i_{D_{RMS}}{}^2 R_T + i_{D_{AVG}} V_{TO} \tag{3.54}$$

Where R_{DS} and R_T are, respectively, the conduction resistance of the MOSFET and diode and V_{TO} is the forward voltage of the diode. Subscripts *S* and *D* correspond to MOSFET and diode quantities, and *RMS* and *AVG* to root-mean-square and average values.

Since the MOSFET and diode are in series, for S_1 to S_4, they have the same values of average and RMS current. Thus, the total conduction losses for S_1 to S_4 (subscripts *SD*) can be defined as:

$$Pcond_{SD} = i_{SD_{RMS}}{}^2 (R_{DS} + R_T) + i_{SD_{AVG}} (V_{TO}) \tag{3.55}$$

For the switching losses, the following equations, (3.56) and (3.57), are used for the calculations. One important detail for the switching losses estimation is that, if the voltage across the series connection of the MOSFET and the diode is positive, the losses will be all concentrated in the MOSFET, thus for this case $P_{SW(\mathrm{diode})}=0$. Likewise, if the voltage across the series connection of the MOFEST and the diode is negative, the losses will be all concentrated in the diode, thus for this case $P_{SW(\mathrm{MOSFET})}=0$.

$$Psw_{MOSFET} = f_s V_{DS} \frac{\left(t_f i_{s_{rise}} + t_r i_{s_{fall}}\right)}{2} + f_s V_{DS} k_{oss} \tag{3.56}$$

$$Psw_{Diode} = f_s V_D Q_{RR} \tag{3.57}$$

Where f_s is the switching frequency; t_f and t_r are, respectively, the rise and fall times of the MOSFET; k_{oss} is the coefficient related to the losses due to the output capacitance C_{oss} of the MOSFET; Q_{RR} is the coefficient related to the losses due to the reverse recovery time of the diode.

From the above equations, one sees that it is necessary to obtain the RMS and average currents of the switches/diodes and maximum voltage of the switches (V_{DS}) and the diodes (V_D). This can be done from the information presented in the first sections of this Chapter and the analysis of the operating states presented in Figures 3.2 and 3.3.

With the analysis of the circuit presented in Figure 3.1, it is possible to see that, when one of the switches S_1 or S_2 is ON, and since they will never be turned ON at the same time for the proposed operating modes discussed in section 3.3, they will always be connected in series with the voltage source V_1. The same happens for switches S_3 and S_4 regarding the voltage source V_2. This way, the average currents circulating through this devices can be determined directly from the rated power of the converter and are presented by equations (3.58) and (3.59).

$$i_{SD1_{AVG}} = i_{SD2_{AVG}} = \frac{P_c}{V_1} \tag{3.58}$$

$$i_{SD3_{AVG}} = i_{SD4_{AVG}} = \frac{P_c}{V_2} \tag{3.59}$$

Next, details regarding the losses estimation for each operating mode discussed in Section 3.3 are presented, where the RMS currents and the maximum voltage of each power semiconductor necessary for the calculations will be presented.

3.5.1 Forward Dual-State Buck

For the Forward Dual-state Buck mode, the expression that defines the total losses of this mode is presented in (3.60). For this operating mode, the three switches used on the Forward operation will present conduction losses. However, since S_3 in ON within all the switching period, just switches S_2 and S_T will present switching losses.

$$P_{FB} = Pcond_{SD2,SD3,ST} + Psw_{SD2,ST} \tag{3.60}$$

Then, as mentioned previously, for the calculation of the losses, it is necessary to know the RMS currents and the maximum voltage across the switches and diodes. This is presented from (3.61) and (3.65), where one can see that all these expressions are defined by known parameters (P_c, V_1 and V_2) and are functions of the n of the TI. Note that the duty cycle D_{23} is also n dependent and, for the Forward Dual-State Buck mode, can be obtained from equation (3.8).

$$i_{SD2_{RMS}} = \frac{P_c}{V_1}\sqrt{\frac{(\Delta i_{LM}(\%)^2 + 12)}{12D_{23}}} \tag{3.61}$$

$$i_{SD3_{RMS}} = \frac{P_c}{V_1}\sqrt{\frac{(\Delta i_{LM}(\%)^2 + 12)\left(1 + (n^2 + 2n)(1 - D_{23})\right)}{12(D_{23})^2}} \tag{3.62}$$

$$i_{ST_{RMS}} = \frac{(n+1)P_c}{V_1}\sqrt{\frac{(\Delta i_{LM}(\%)^2 + 12)(1 - D_{23})}{12(D_{23})^2}} \tag{3.63}$$

$$V_{SD2_{max}} = V_1 + nV_2 \tag{3.64}$$

$$V_{ST_{max}} = \frac{V_1 + nV_2}{n+1} \tag{3.65}$$

3.5.2 Forward Dual-State Buck-Boost

For the Forward Dual-State Buck-Boost mode, the expression that defines the total losses of this mode is presented in (3.66). Similar to the Forward Dual-state Buck mode, all the switches present conduction losses. On the other hand, for this mode, the switches that present switching losses are S_2 and S_3, and not S_T as in the previous mode.

$$P_{FBB} = Pcond_{SD2,SD3,ST} + Psw_{SD2,SD3} \tag{3.66}$$

The RMS currents of each switch and their maximum voltage value are presented from (3.67) to (3.71). Similar to the previous section, the duty cycle D_{2T} of this mode is a function of *n*.

$$i_{SD2_{RMS}} = \frac{P_c}{V_1}\sqrt{\frac{(\Delta i_{LM}(\%)^2 + 12)}{12D_{2T}}} \tag{3.67}$$

$$i_{SD3_{RMS}} = \frac{nP_c}{V_1}\sqrt{\frac{(\Delta i_{LM}(\%)^2 + 12)(1 - D_{2T})}{12(D_{2T})^2}} \tag{3.68}$$

$$i_{ST_{RMS}} = \frac{P_c}{V_1}\sqrt{\frac{(\Delta i_{LM}(\%)^2 + 12)(n^2(1 - D_{2T}) + D_{2T})}{12(D_{2T})^2}} \tag{3.69}$$

$$V_{SD2_{max}} = V_1 + nV_2 \tag{3.70}$$

$$V_{SD3_{max}} = -\left(\frac{V_1 + nV_2}{n}\right) \tag{3.71}$$

3.5.3 Reverse Dual-State Boost

The total power losses for the Reverse Dual-state Boost mode are defined by (3.72). For this operating mode, the three switches used on the Reverse operation (S_1, S_4 and S_T) will present conduction losses. However, since S_4 is ON within all the switching period, just switches S_1 and S_T will present switching losses.

$$P_{RB} = Pcond_{SD1,SD4,ST} + Psw_{SD1,ST} \tag{3.72}$$

The RMS currents of each switch and their maximum voltage value are presented from (3.73) to (3.77). To obtain the duty cycle D_{4T} of this mode as a function of the turns ratio, equation (3.34) is used.

$$i_{SD1_{RMS}} = \frac{nP_c}{V_2}\sqrt{\frac{(\Delta i_{LM}(\%)^2 + 12)(1 - D_{4T})}{12(n + D_{4T})^2}} \tag{3.73}$$

$$i_{SD4_{RMS}} = \frac{P_c}{V_2}\sqrt{\frac{(\Delta i_{LM}(\%)^2 + 12)(n^2 + 2D_{4T}n + D_{4T})}{12(n + D_{4T})^2}} \tag{3.74}$$

$$i_{ST_{RMS}} = \frac{(n+1)P_c}{V_2}\sqrt{\frac{(\Delta i_{LM}(\%)^2 + 12)D_{4T}}{12(n + D_{4T})^2}} \tag{3.75}$$

$$V_{SD1_{max}} = -\left(\frac{nV_1 + V_2}{n}\right) \tag{3.76}$$

$$V_{ST_{max}} = \frac{nV_1 + V_2}{n+1} \tag{3.77}$$

3.5.4 Reverse Dual-State Buck-Boost

Finally, equation (3.78) presents the total power losses for the Reverse Dual-state Buck-Boost mode. Similar to the Reverse Boost mode, all three switches of the reverse operation present conduction losses. However, for the Buck-Boost mode, the switches that present switching losses are S_1 and S_4.

$$P_{RBB} = Pcond_{SD1,SD4,ST} + Psw_{SD1,SD4} \tag{3.78}$$

The RMS currents of each switch and their maximum voltage value are presented from (3.79) to (3.83).

$$i_{SD1_{RMS}} = \frac{nP_c}{V_2}\sqrt{\frac{(\Delta i_{LM}(\%)^2 + 12)(1 - D_{4T})}{12(D_{4T})^2}} \tag{3.79}$$

$$i_{SD4_{RMS}} = \frac{P_c}{V_2}\sqrt{\frac{(\Delta i_{LM}(\%)^2 + 12)}{12D_{4T}}} \tag{3.80}$$

$$i_{ST_{RMS}} = \frac{P_c}{V_1}\sqrt{\frac{(\Delta i_{LM}(\%)^2 + 12)(n^2(1 - D_{4T}) + D_{4T})}{12(D_{2T})^2}} \tag{3.81}$$

$$V_{SD1_{max}} = -\left(\frac{nV_1 + V_2}{n}\right) \tag{3.82}$$

$$V_{SD4_{max}} = nV_1 + V_2 \tag{3.83}$$

3.6 Design Procedure for Determination of Turns Ratio/Mode of Operation

With the knowledge provided by the previous sections, the losses of the converter for a given case study can be plotted. The application scenario for the selection of *n* and for the operating modes of the novel 5-switch converter is as an interface between two DC-buses/elements as depicted in Figure 3.1. It is assumed that the values of R_1 and R_2 are known and assumed to be the same as in Chapter 2, then R_1=R_2=0.625Ω. To match the operating modes discussed previously in this Chapter, where V_1 was defined to be the high-voltage side, the rated voltages were taken as V_1 = 380 V and V_2 = 96 V and the rated power is 1 kW.

Then, one needs to choose suitable power devices based on the voltage/current/power ratings of the converter. Also, since the final goal is to actually build/assembly the TI and converter, factors such as costs of the power semiconductors and accessibility to acquire them should also be taken into account. Based on all this aspects, the devices that are presented next in Table 3.5 were chosen.

Table 3.5 – Power semiconductors chosen for the design procedure

Components	**Devices**	**Parameters**
S_1 to S_T	5x IPW90R120C3 (900V/36A)	$R_{DS} = 0.12\Omega$; $t_f = 25$ns; $t_r = 20$ns; $k_{oss} = 3.9855$e-8 J/V
D_1 to D_4	4x FFSH30120A (1200V/30A)	$R_T = 0.013\Omega$; $V_{TO} = 1.45$V

For the plotting of the losses, the magnetizing current ripple is defined as 25% of the average value of the magnetizing current and the results of power losses are shown in Figure 3.10.

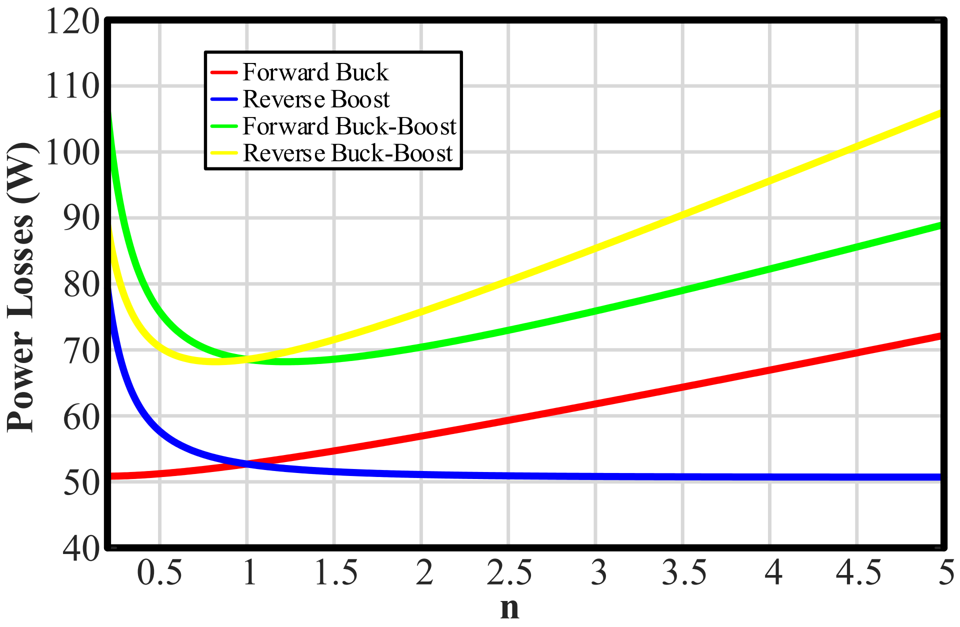

Figure 3.10 – Losses of the novel 5-switch converter as function of the turns ratio

From Figure 3.10, one sees that in the Forward mode, operation in the Buck mode (red curve) leads to lower power losses than the Buck-Boost mode (green curve). In the Reverse mode, operation in the Boost mode (blue curve) leads to lower power losses than the Buck-Boost mode (yellow curve).

For the choice of the actual value of n, one should consider reasonable steady-state values for D. Assuming that this should be kept in the range of 0.3 and 0.7, one can use equations (3.8), (3.21), (3.34) and (3.47) to determine the maximum and minimum value of n for each of the possible operating modes. By doing so, one finds the following: for the Forward Buck mode, one calculates that $0.268 \leq n \leq 5.903$; for the Forward Buck-Boost mode, $1.696 \leq n \leq 9.236$; for the Reverse Boost mode one gets $0.169 \leq n \leq 3.733$ while for the reverse Buck-Boost mode $0.108 \leq n \leq 0.589$.

For the final choice of *n*, there should be an overlap between the *n* values of a Forward and a Reverse mode. Since the Forward Buck and Reverse Boost clearly present the lowest losses, and an overlap for the range of $0.268 \leq n \leq 3.733$ is found for the combined modes, they are the selected modes of operation for the proposed case study. The next step is to find, within this range, the value of turns ratio where the converter would present the maximum efficiency possible, thus making this specific point the selected value for the turns ratio for the design of the TI. This is presented in Figure 3.11.

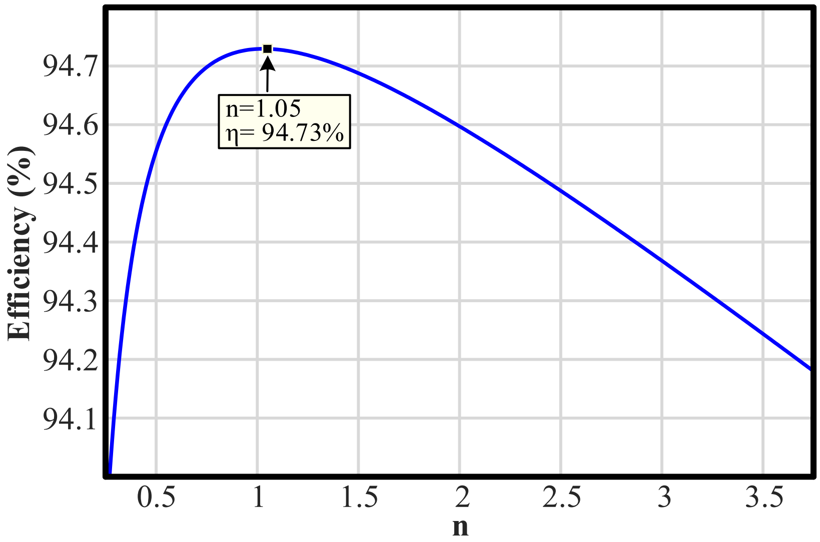

Figure 3.11 – Efficiency of the combined Forward Buck and Reverse Boost modes

From Figure 3.11, one sees that for the combination of the Forward Buck and Reverse Boost modes considering the proposed case study and the assumptions made throughout the last sections, the converter operates with an estimated maximum efficiency of 94.73% when the value of *n* of the TI is set to be 1.05, therefore making this the ideal value for operation of the 5-switch bidirectional DC-DC converter discussed in this case study. However, it should be noted that to facilitate the assembly of the TI, *n* could be adjusted in this case to 1 without compromising significantly the efficiency of the system.

3.7 Validation of Design Procedure

The verification of the equations derived in Section 3.5 for the choice of *n* of the TI and mode of operation of the converter are conducted in this section. The calculation of the converter losses is carried out using the Thermal Module available in the power electronics software PSIM. The parameters of the semiconductors depicted in Table 3.5 were used for the simulations of the converter operating in the Buck and Boost modes, with Forward and Reverse power flows for TIs with *n* of 1 and 3, respectively, for an output power of 1 kW. The "supply side" voltage was set at either 96 V or 380 V and the appropriate duty cycles to obtain the desired "load side" voltages were computed with the voltage gain equations presented in Section 3.3: 380 V or 96 V. Table 3.6 presents the theoretical and measured power losses as well the estimated efficiency for the converter operating in the Forward (Buck) and Reverse (boost) modes, for a TI with *n* = 1 and 3.

Table 3.6 – Power losses for different modes of operation and *n* of the TI

n	Mode	P_{Loss}(Th)	P_{Loss}(Sim)	Err. (%)	Effc. (Th)	Effc. (Sim)
1	F. Buck	52.71W	52.94W	+0.43%	94.73%	94.87%
	R. Boost	52.71W	49.64W	-5.82%		
3	F. Buck	61.81W	59.24W	-4.16%	94.37%	94.58%
	R. Boost	50.82W	49.24W	-3.11%		

From Table 3.6, one can see, as in Figure 3.10, that while the power losses in the Buck mode increase with *n*, it decreases slightly with *n* in the Boost mode. Overall, the efficiency considering the average of both modes is higher for a TI with *n* = 1, 94.73% theoretical and 94.87% simulated, than with *n* = 3, 94.37% theoretical and 94.58% simulated, as anticipated by Figure 3.11. It should be noted that the equations presented through this Chapter were developed for an ideal loss-less converter and, for the simulation procedure, current/voltage ripples and the intrinsic elements of each element/device are also taken into account, causing a slight error between theoretical and simulated values. However, one sees from Table 3.6 that the results are on an acceptable error range, where the worst case, the Reverse Boost for *n*=1, presented an error of just -5.82% from the simulated value to the theoretical one, this way validating the design approach presented in this Chapter.

3.8 Chapter Conclusion

In this Chapter, a novel 5-switch Bidirectional DC-DC converter based on a TI was proposed, where details regarding its conceptualization alongside with its operation principle (operating states and modes) were presented. Among the main features of this novel topology, high voltage conversion characteristic can be achieved by adjusting the *n* of its TI, allowing the converter to operate with wide input/output voltage ranges. Also, the direction of the power flow can be reversed without changing the direction of the intermediate inductor (magnetizing inductance) current (i_{LM}), which favors a faster dynamic response in case of power flow reversal. This characteristics have shown to be well suitable for applications where SCs are required.

In order to select the value of n for the TI and the modes of operation for a given case study, an approach based on minimizing the power losses on the semiconductors of the novel 5-switch Bidirectional DC-DC converter was also discussed. To achieve this goal, the proposed converter and a group of its operating modes were presented in detail. All the necessary steps to find the design equations for the power losses estimation of each operating mode discussed previously were carried out.

The calculations and approach presented in this Chapter indicate that the selection of the operating mode and the determination of the turns ratio of the TI play a role on the losses across the power switches of the novel 5-switch bidirectional DC-DC converter. By choosing two specific operating modes (Forward Buck and Reverse Boost) and a specific turns ratio value (n=1.05), the maximum efficiency of the converter was found to be 94.73% for the proposed case study. As verified by the simulation procedure, the choice of n and mode of operation of the converter according to the proposed method leads to lower power losses across the switches and higher efficiency for the converter.

4. Exact Feedback Linearization of a Multi-Variable Controller for the Novel 5-Switch Bidirectional DC-DC Converter

4.1 Chapter Introduction

In this Chapter, exact state feedback linearization is applied to the new bidirectional DC-DC converter with TI proposed in the last Chapter, where a systematic approach for deriving control laws for the TI current and output voltage is presented. It is a Dual-Input Dual-Output (DIDO) system, which is the simplest form of a Multi-Input Multi-Output (MIMO) system, where the magnitude of the inductor current presents a certain degree of independence with regards to the output voltage. In principle, it can be adjusted as a trade-off between converter losses and speed of response of the output voltage. For this, a multi-state modulation scheme, with multiple modulation signals to eliminate the RHP zero typically found in converters with intermediate inductors and an auxiliary variable to determine the power flow direction, is proposed for the modelling of the novel 5-switch DC-DC converter.

This Chapter is organized as follows: In Section 4.2, PWM modulator scheme proposed is discussed. Section 4.3 presents the modelling of the system for both power flow directions, and how they are combined into a single model. Section 4.4 presents the derivation of the control law of the converter based on exact state feedback linearization while Section 4.5 presents the system parameters, with considerations for controller design. The performance of the 5-switch converter operating in the tri-state Buck-Boost mode with state feedback by means of simulation is verified in Section 4.6. It also presents a comparison with the conventional dual-state Buck-Boost with cascaded inner current outer voltage loops with linear PI controllers. Finally, Section 4.7 provides the final conclusion of this Chapter.

4.2 The Modulation Scheme

The way to control novel 5-switch converter is through the control of D and the switching logic of its 5 switches. For this, the PWM modulator presented in Figure 4.1 is proposed, where one can see that 3 controllable modulating signals (m_1, m_2 and m_3) are used, where they are compared to a carrier signal V_m in order to generate the gating signals for the switches. Once the gating signals are generated, it is of paramount importance to correctly send them to the right switches to set the desired power flow direction. For this, a new binary variable based on the direction of the current

i_2, defined as "q", is implemented: if i_2 is positive, the power flows from the V_1 side to the V_2, q = 1 and the converter will operate in the Forward mode; if i_2 is negative, the power flows from the V_2 side to the V_1, q = 0 and the converter will operate in the Reverse mode. From Figure 4.1, one can see that this operation is done by means of 4 MUXs blocks, each associated with a particular unidirectional switch. The only switch that is not "q-dependent" is S_T, where its D is controlled exclusively through the controllable modulating signal m_1, being the only switch that is used for both power flow directions regardless the mode the converter works.

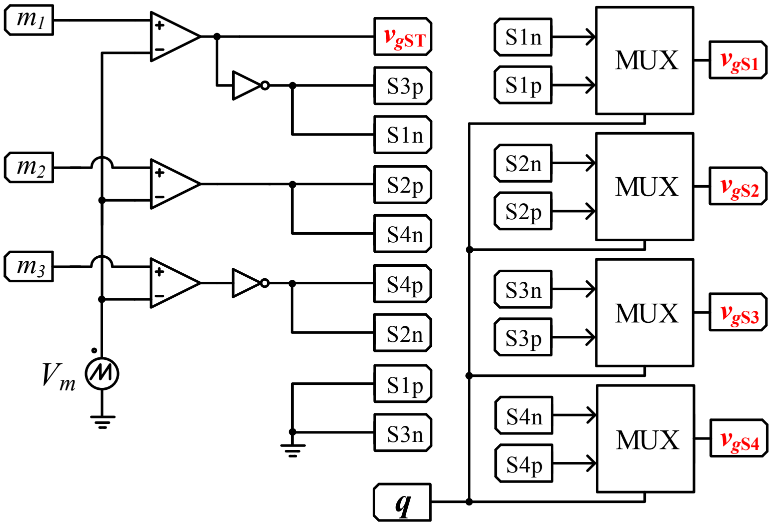

Figure 4.1 – PWM modulator for the novel 5-switch converter mode of operation.

4.3 Modelling of the System

Similar to what was done for the 4-switch converter in Chapter 2, in order to be able to design a suitable control law, a model based on the state variables of the system describing its dynamics must be found. However, since the novel 5-switch converter presents different operating states based on the power flow direction, a model for each case can be determined. This is presented next.

4.3.1 Forward Mode

The switching scheme for the Forward mode is presented next in Figure 4.2. There, one can see from Figure 4.2(b) that, when the converter operates in the Forward Mode with q = 1, the control variable m_1 controls switches S_T and S_3, where S_T is controlled by the main PWM signal while S₃ receives its complementary signal. Also, for this mode, control variables m_2 and m_3 will control, respectively, switches S₂ and S₄. With this gating signal generation, the sequence of states that arises is presented in Figure 4.2(c), where the subscript represents the current path.

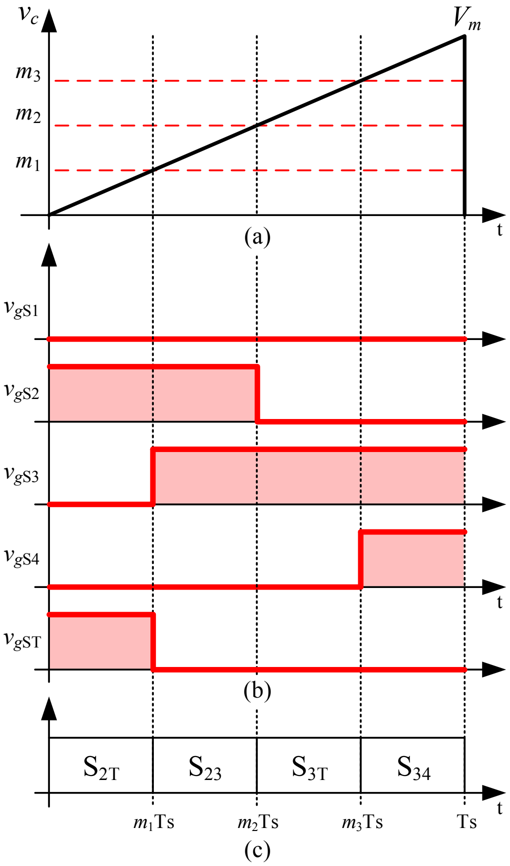

Figure 4.2 – Switching-scheme for the Forward Mode: (a) PWM modulator (b) Gating signals (c) Sequence of states

With the analysis of the operating states presented in Chapter 3, one obtains averaged equations that reflect the impact of the two DC-voltage units (V_1 and V_2), resistors R_1 and R_2, and the input and output filters C_1 and C_2 on the state variables of the converter for the Forward mode. They are presented next from (4.1) to (4.3).

$$V_{LM(f)} = v_{C1}\left[m_1 + \left(\frac{n}{n+1}\right)(m_2 - m_1)\right] - v_{C2}\left[\left(\frac{n}{n+1}\right)(m_2 - m_1) + n(m_3 - m_2)\right] \quad (4.1)$$

$$I_{C1(f)} = i_1 - i_{LM}\left[m_1 + \left(\frac{n}{n+1}\right)(m_2 - m_1)\right] \quad (4.2)$$

$$I_{C2(f)} = -i_2 + i_{LM}\left[\left(\frac{n}{n+1}\right)(m_2 - m_1) + n(m_3 - m_2)\right] \quad (4.3)$$

Then, by considering the input and output currents (i_1 and i_2) as a function of their respective voltages and feeder resistances, one finds the final model for the Forward mode to be:

$$\frac{di_{LM(f)}}{dt} = \frac{v_{C1}}{L_M}\left[m_1 + \left(\frac{n}{n+1}\right)(m_2 - m_1)\right] - \frac{v_{C2}}{L_M}\left[\left(\frac{n}{n+1}\right)(m_2 - m_1) + n(m_3 - m_2)\right] \quad (4.4)$$

$$\frac{dv_{C1(f)}}{dt} = \frac{V_1}{R_1C_1} - \frac{v_{C1}}{R_1C_1} - \frac{i_{LM}}{C_1}\left[m_1 + \left(\frac{n}{n+1}\right)(m_2 - m_1)\right] \quad (4.5)$$

$$\frac{dv_{C2(f)}}{dt} = \frac{V_2}{R_2C_2} - \frac{v_{C2}}{R_2C_2} + \frac{i_{LM}}{C_2}\left[\left(\frac{n}{n+1}\right)(m_2 - m_1) + n(m_3 - m_2)\right] \quad (4.6)$$

4.3.2 Reverse Mode

Now, for the Reverse mode, it is assumed that the power flows from V_2 to V_1 and, in this case, i_1 and i_2 are negative. The PWM modulator for this mode is presented in Figure 4.3, being the same as the one used for the Forward Mode. However, the gating signal generation, Figure 4.3(b) is different, generating a new sequence of operating states that is presented in Figure 4.3(c).

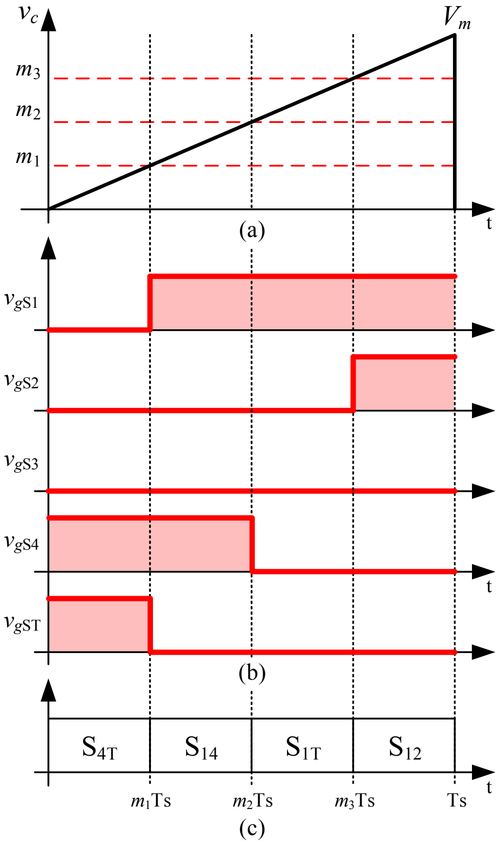

Figure 4.3 – Switching-scheme for the Reverse Mode: (a) PWM modulator (b) Gating signals (c) Sequence of states

Similar to the Forward mode, with the analysis of the operating states for the Reverse mode presented in Chapter 3, one can find the following set of averaged equations for the converter operating in the Reverse mode.

$$V_{LM(r)} = -v_{C1}\left[\left(\frac{n}{n+1}\right)(m_2 - m_1) + n(m_3 - m_2)\right] + v_{C2}\left[m_1 + \left(\frac{n}{n+1}\right)(m_2 - m_1)\right] \quad (4.7)$$

$$I_{C1(r)} = i_1 + i_{LM}\left[\left(\frac{n}{n+1}\right)(m_2 - m_1) + n(m_3 - m_2)\right] \quad (4.8)$$

$$I_{C2(r)} = -i_2 - i_{LM}\left[m_1 + \left(\frac{n}{n+1}\right)(m_2 - m_1)\right] \quad (4.9)$$

Then, by considering the input and output currents as a function of their respective voltages and feeder resistances, one finds the final model for the Reverse mode to be:

$$\frac{di_{LM(r)}}{dt} = \frac{-v_{C1}}{L_M}\left[\left(\frac{n}{n+1}\right)(m_2 - m_1) + n(m_3 - m_2)\right] + \frac{v_{C2}}{L_M}\left[m_1 + \left(\frac{n}{n+1}\right)(m_2 - m_1)\right] \quad (4.10)$$

$$\frac{dv_{C1(r)}}{dt} = \frac{V_1}{R_1C_1} - \frac{v_{C1}}{R_1C_1} + \frac{i_{LM}}{C_1}\left[\left(\frac{n}{n+1}\right)(m_2 - m_1) + n(m_3 - m_2)\right] \quad (4.11)$$

$$\frac{dv_{C2(r)}}{dt} = \frac{V_2}{R_2C_2} - \frac{v_{C2}}{R_2C_2} - \frac{i_{LM}}{C_2}\left[m_1 + \left(\frac{n}{n+1}\right)(m_2 - m_1)\right] \quad (4.12)$$

4.3.3 Model-Mixing Approach

In order to be able to control the converter, it is important to have a unified model that defines the converter for both the Forward and the Reverse modes regardless of the power flow direction. Since the power converter will never operate in both modes at the same time, one can assume that the final model that describes the entire system regardless of the operating mode will be the actual model of each mode, for as long as the converter stays operating in that specific mode. This is better illustrated by (4.13) – (4.15), where the two models found in the previous sections are mixed into a single and final one that is also a function of the variable q. This is done by multiplying the Forward mode model by q and the Reverse model by $\bar{q}$ and adding them. Note that, if the converter operates in the Forward mode, $q = 1$ and $\bar{q} = 0$, thus the final unified model of the converter will be the model developed for the Forward Mode. On the other hand, if the converter operates in the Reverse mode, $q = 0$ and $\bar{q} = 1$, and the final unified model of the converter will be the model developed for the Reverse Mode. It should be noted that this approach is important in order to have a single controller that works for both power flow directions. Otherwise, if the models were to be treaty individually, one would have to design specific controllers for each power flow direction, which would bring even more complexity to the system.

$$\frac{di_{LM}}{dt} = \frac{di_{LM(f)}}{dt}(q) + \frac{di_{LM(r)}}{dt}(\bar{q}) \tag{4.13}$$

$$\frac{dv_{C1}}{dt} = \frac{dv_{C1(f)}}{dt}(q) + \frac{dv_{C1(r)}}{dt}(\bar{q}) \tag{4.14}$$

$$\frac{dv_{C2}}{dt} = \frac{dv_{C2(f)}}{dt}(q) + \frac{dv_{C2(r)}}{dt}(\bar{q}) \tag{4.15}$$

Then, replacing (4.4) - (4.6) and (4.10) - (12) into (4.13) - (4.15), one finds the final model to be:

$$\frac{di_{LM}}{dt} = \dot{i_{LM}} = \frac{v_{C1}}{L_M}(u_2) - \frac{v_{C2}}{L_M}(u_1) \tag{4.16}$$

$$\frac{dv_{C1}}{dt} = \dot{v_{C1}} = \frac{V_1}{R_1C_1} - \frac{v_{C1}}{R_1C_1} - \frac{i_{LM}}{C_1}(u_2) \tag{4.17}$$

$$\frac{dv_{C2}}{dt} = \dot{v_{C2}} = \frac{V_2}{R_2C_2} - \frac{v_{C2}}{R_2C_2} + \frac{i_{LM}}{C_2}(u_1) \tag{4.18}$$

Where the new nonlinear control variables u_1 and u_2 are:

$$u_1 = \left[\left(\frac{n}{n+1}\right)(m_2 - m_1) + n(m_3 - m_2)\right]q - \left[m_1 + \left(\frac{n}{n+1}\right)(m_2 - m_1)\right]\bar{q} \tag{4.19}$$

$$u_2 = \left[m_1 + \left(\frac{n}{n+1}\right)(m_2 - m_1)\right]q - \left[\left(\frac{n}{n+1}\right)(m_2 - m_1) + n(m_3 - m_2)\right]\bar{q} \tag{4.20}$$

4.4 Exact State Feedback Linearization

The non-linear characteristics of this system can be observed in the model developed in the previous section. It includes cross products between the state variables and the new control variables u_1 and u_2. Using the conventional linearization approach based on small signal variations around an operating point to design conventional PI-controllers, information would be lost and the system would not be fully described by the resulting model.

The main goal of an ESS is usually to control the output current, i_2, what can be done indirectly through the output voltage, v_{C2}. Frequently, this is done by employing a cascaded inner inductor current and outer output voltage control loop. However, since the developed model presents two control variables, u_1 and u_2, and in order to give more flexibility to the considered non-linear controller, a parallel control structure similar is implemented. In this case, the inductor current reference can be chosen according to the system needs, with high values favoring a faster dynamic response and lower ones for improved efficiency.

The first step of the controller design is to rewrite the DIDO system, presented in Figure 4.4, in an affine linear form to apply the theory of exact state feedback linearization. This is done by means of (4.21) and (4.22).

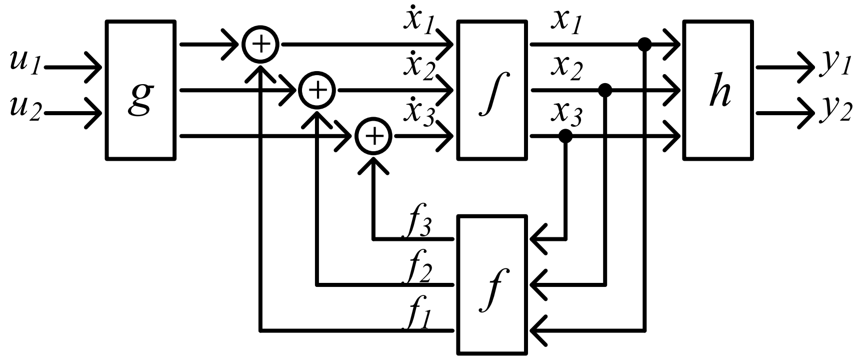

Figure 4.4 – Block diagram representation of the DIDO system

$$\dot{x} = f(x) + g(x)u \tag{4.21}$$

$$y = h(x) \tag{4.22}$$

Where $x \in \mathbb{R}^n$ is the state vector; $u \in \mathbb{R}^m$ relates to the control inputs; $y \in \mathbb{R}^{i}y$ defines the controlled outputs; *f*, *g*, and *h* are differentiable vector fields. Considering the model developed in the last section:

$$x = [i_{LM}, v_{C1}, v_{C2}]^t = [x_1, x_2, x_3]^t \tag{4.23}$$

$$u = [u_1, u_2]^t \tag{4.24}$$

$$f(x) = \left[0, \frac{V_1}{R_1C_1} - \frac{x_2}{R_1C_1}, \frac{V_2}{R_2C_2} - \frac{x_3}{R_2C_2}\right]^t \tag{4.25}$$

$$g(x) = \begin{bmatrix} -\frac{x_3}{L_M} & \frac{x_2}{L_M} \\ 0 & -\frac{x_1}{C_1} \\ \frac{x_1}{C_2} & 0 \end{bmatrix}, g_1(x) = \left[-\frac{x_3}{L_M}, 0, \frac{x_1}{C_2}\right]^t, g_2(x) = \left[\frac{x_2}{L_M}, -\frac{x_1}{C_1}, 0\right]^t \tag{4.26}$$

$$h_1(x) = x_1 = [1,0,0];\ h_2(x) = x_3 = [0,0,1] \tag{4.27}$$

There are several ways for obtaining the feedback linearization of the DIDO system [61] – [66]. First, the model is rewritten in a different set of coordinates, using the output *y* and its successive derivatives. This procedure is performed based on equation (4.22), obtaining:

$$\dot{y_i} = L_f h_i + \sum_{j=1}^{m} \left(L_{gj} h_i\right) u_j \tag{4.28}$$

Where $L_f h$ and $L_g h$ are, respectively, *Lie derivatives* of the smooth scalar vector *h*(*x*) as a function of *f*(*x*) and *g*(*x*). If $L_{gj}\, h_i(x) = 0$ for all *j*, then the inputs do not appear, and as highlighted by [63] and [64], one needs to differentiate repetitively as:

$$y_i{}^{(r_i)} = L_f{}^{(r_i)} h_i + \sum_{j=1}^{m} \left(L_{gj} L_f{}^{(r_i-1)} h_i\right) u_j \tag{4.29}$$

Until $L_{gj} L_f{}^{(r_i-1)} h_i \neq 0$ for at least one *j*. The values of r_i are the sub-relative degrees of the DIDO system and $L_{gj} L_f{}^{ri-1}\, h_i$ is the *Lie derivative* of the *i*-th output as a function of *f*(*x*) and *g*(*x*) [62] [63]. In such a case, (4.29) can be rewritten as:

$$\begin{bmatrix} y_1^{r_1} \\ \cdots \\ y_i^{r_i} \end{bmatrix} = A(x) + E(x) \begin{bmatrix} u_1 \\ \cdots \\ u_2 \end{bmatrix} \tag{4.30}$$

Where:

$$A(x) = \begin{bmatrix} L_f{}^{r_1} h_1 \\ \cdots \\ L_f{}^{r_i} h_i \end{bmatrix} \tag{4.31}$$

And:

$$E(x) = \begin{bmatrix} L_{g1} L_f{}^{(r_1-1)} h_1 & \cdots & L_{gm} L_f{}^{(r_1-1)} h_1 \\ \cdots & \cdots & \ldots \\ L_{g1} L_f{}^{(r_i-1)} h_i & \ldots & L_{gm} L_f{}^{(r_i-1)} h_i \end{bmatrix} \tag{4.32}$$

Matrix *E(x)* is called the decoupling matrix of the DIDO system. If it is nonsingular, the following input transformation can be defined:

$$u = -E^{-1} A(x) + E^{-1}(x) z \tag{4.33}$$

Where *z* concerns new input variables.

Substituting (4.33) in (4.30) results in a linear and decoupled differential relation between the output *y* and the new input *z* [35].

$$\begin{bmatrix} y_1^{r_1} \\ \cdots \\ y_i^{i} \end{bmatrix} = \begin{bmatrix} z_1 \\ \cdots \\ z_i \end{bmatrix} \tag{4.34}$$

It is important to remark that (4.30), or its closed loop (4.34), creates a new model for the converter. If this new state vector, represented by the original outputs and their derivatives, does not match the same number of states (n_s) of the original system, it means that this new mathematical model is not describing the dynamics of all states in the converter. As a consequence, any analysis based on this new model would disregard the remaining states. Those are called the zero-dynamics of this new representation. For a complete analysis of the converter, one must consider these new variables as well as these zero-dynamics.

Taking into account the 5-switch converter and its model with two nonlinear control variables (u_1 and u_2) and two state variables to be controlled (i_{Lm} and v_{C2}), one can find the sub-relative degrees by considering $m = 2$ (two inputs) and $i = 1$ and 2 (two outputs).

By solving the Lie derivatives one can find the sub-relatives degrees of the system as:

- For $y_1 = h_1 = x_1 = i_{Lm} = [1, 0, 0]$, then:

$$\begin{cases} L_{g1}h_1 = [1\ 0\ 0]\left[-\dfrac{x_3}{L_M}, 0, \dfrac{x_1}{C_2}\right]^t = -\dfrac{x_3}{L_M} \\ L_{g2}h_1 = [1\ 0\ 0]\left[\dfrac{x_2}{L_M}, -\dfrac{x_1}{C_1}, 0\right]^t = \dfrac{x_2}{L_M} \end{cases} \tag{4.35}$$

- For $y_2 = h_2 = x_3 = v_{C2} = [0, 0, 1]$, then:

$$\begin{cases} L_{g1}h_2 = [0\ 0\ 1]\left[-\dfrac{x_3}{L_M}, 0, \dfrac{x_1}{C_2}\right]^t = \dfrac{x_1}{C_2} \\ L_{g2}h_2 = [0\ 0\ 1]\left[\dfrac{x_2}{L_M}, -\dfrac{x_1}{C_1}, 0\right]^t = 0 \end{cases} \tag{4.36}$$

Thus, the sub-relative degrees of the system are $r_1 = 1$ and $r_2 = 1$. Knowing these two values, it is possible now to fully define matrix $E(x)$ as:

$$E(x) = \begin{bmatrix} L_{g1}L_f^{r_1-1}h_1 & L_{g2}L_f^{r_1-1}h_1 \\ L_{g1}L_f^{r_2-1}h_2 & L_{g2}L_f^{r_2-1}h_2 \end{bmatrix} = \begin{bmatrix} L_{g1}L_f^0 h_1 & L_{g2}L_f^0 h_1 \\ L_{g1}L_f^0 h_2 & L_{g2}L_f^0 h_2 \end{bmatrix} \tag{4.37}$$

Therefore, by replacing (4.35), and (4.36) into (4.37), matrix $E(x)$ is finally given by:

$$E(x) = \begin{bmatrix} -\dfrac{x_3}{L_M} & \dfrac{x_2}{L_M} \\ \dfrac{x_1}{C_2} & 0 \end{bmatrix} \tag{4.38}$$

Next, one computes vector *A*(*x*) as:

$$A(x) = \begin{bmatrix} L_f^{r_1} h_1 \\ L_f^{r_2} h_2 \end{bmatrix} = \begin{bmatrix} L_f h_1 \\ L_f h_2 \end{bmatrix} \tag{4.39}$$

Where:

$$\begin{cases} L_f h_1 = [1 \quad 0 \quad 0] \left[0, \dfrac{V_1}{R_1 C_1} - \dfrac{x_2}{R_1 C_1}, \dfrac{V_2}{R_2 C_2} - \dfrac{x_3}{R_2 C_2} \right]^t = 0 \\ L_f h_2 = [0 \quad 0 \quad 1] \left[0, \dfrac{V_1}{R_1 C_1} - \dfrac{x_2}{R_1 C_1}, \dfrac{V_2}{R_2 C_2} - \dfrac{x_3}{R_2 C_2} \right]^t = \dfrac{V_2}{R_2 C_2} - \dfrac{x_3}{R_2 C_2} \end{cases} \tag{4.40}$$

Thus:

$$A(x) = \left[0, \frac{V_2}{R_2 C_2} - \frac{x_3}{R_2 C_2} \right]^t \tag{4.41}$$

With matrices *E*(*x*) and *A*(*x*) defined, one obtains the control law of the converter from (4.33) as:

$$u = \begin{bmatrix} \dfrac{x_3 - V_2}{R_2 x_1} \\ \dfrac{x_3 (x_3 - V_2)}{R_2 x_1 x_2} \end{bmatrix} + \begin{bmatrix} 0 & \dfrac{C_2}{x_1} \\ \dfrac{L_M}{x_2} & \dfrac{x_3 C_2}{x_1 x_2} \end{bmatrix} z \tag{4.42}$$

It should be noted that, since for this particular converter $i_{LM} = x_1$ does not need to be reversed for power flow reversal and $v_{C1} = x_2 \approx V_1 > 0$ and $v_{C2} = x_3 \approx V_2 > 0$, there are no singularities in the linearized system. Particularizing (4.34) for this converter, one observes that the equivalent system is linear and decoupled as shown in (4.43). It can be represented by a block diagram as shown in Figure 4.5.

$$\begin{bmatrix} y_1^1 \\ y_2^1 \end{bmatrix} = \begin{bmatrix} i_{Lm} \\ \dot{v}_{C2} \end{bmatrix} = \begin{bmatrix} z_1 \\ z_2 \end{bmatrix} \tag{4.43}$$

For tracking reference values for i_{LM} and v_{C2}, given by i_{LM_ref} and v_{C2_ref}, respectively, one can use simple proportional controllers to obtain inputs z_1 and z_2 required in (4.43). This implies in taking:

$$
\begin{aligned}
z_1 &= -\lambda_1\left(i_{LM} - i_{LM\_ref}\right) \\
z_2 &= -\lambda_2\left(v_{C2} - v_{C2\_ref}\right)
\end{aligned}
\tag{4.44}
$$

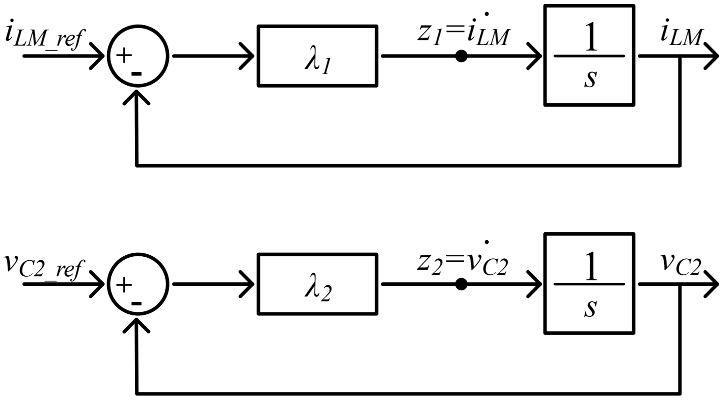

Figure 4.5 – Linear decoupled model of the 5-Switch converter

The overall system, with the original system, exact state feedback linearization network and simple proportional controllers is shown in Figure 4.6. In general, the objective of the "control system" is to provide the modulation signals that will result in the tracking of some reference quantities. In this case, the modulation signals are m_1, m_2, and m_3, and the quantities to be tracked are $i_{LM} = x_1$ and $v_{C2} = x_3$. The modulation signals can be obtained from (4.19) and (4.20), provided that u_1 and u_2 (signals in the input of block "*system*" in Figure 4.6) are known, and given operating mode from Tables 3.2 and 3.4 are determined. According to (4.42), and as depicted in Figure 4.6, u_1 and u_2 are functions of the state variables $i_{LM} = x_1$, $v_{C1} = x_2$ and $v_{C2} = x_3$ as well as z_1 and z_2. The latter, are the outputs of the proportional controllers of the inductor current and output voltage loops, shown in Figure 4.5 and (4.44).

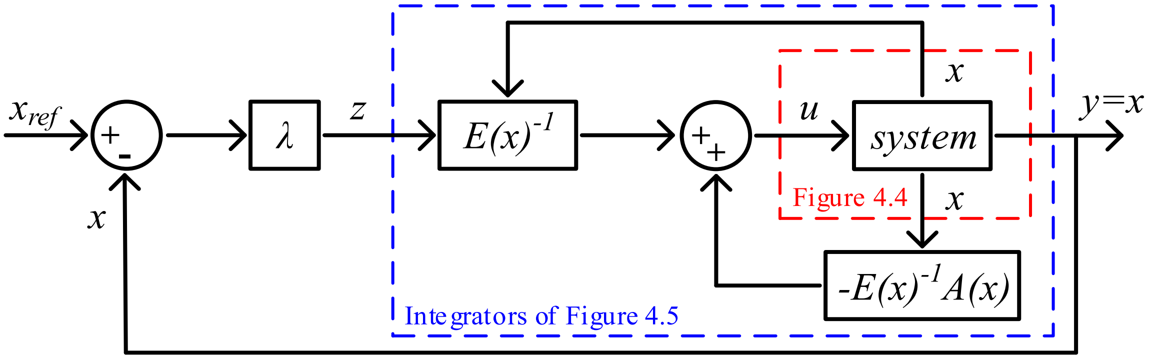

Figure 4.6 – Model of the DIDO system with the state-feedback linearization network and simple P-type controllers.

4.4.1 Zero-Dynamics Analysis

Now it is necessary to study the remaining dynamics of the system, the so-called zero-dynamics. In the present case they are trivial and are represented by the remaining state v_{C1}. For this analysis, one considers that dynamics when the controlled ones reach their equilibrium point. Then, the control boils down to (remark that $z = 0$ for this analysis):

$$\bar{u} = \begin{bmatrix} \dfrac{\overline{v_{C2}} - V_2}{R_2 \overline{\imath_{LM}}} \\ \dfrac{\overline{v_{C2}}(\overline{v_{C2}} - V_2)}{R_2 \overline{\imath_{LM}} x_2} \end{bmatrix} \tag{4.45}$$

And the zero-dynamics become:

$$\dot{v_{C1}} = -\frac{v_{C1}}{R_1 C_1} - \frac{\overline{v_{C2}}(\overline{v_{C2}} - V_2)}{C_1 R_2 v_{C1}} + \frac{V_1}{R_1 C_1} \tag{4.46}$$

This system has two equilibrium points given by:

$$v_{C1} = \frac{V_1}{2} \pm \sqrt{\frac{{V_1}^2}{4} - \overline{v_{C2}}(\overline{v_{C2}} - V_2)} \tag{4.47}$$

Where only the larger solution is feasible. This one, has as Jacobian:

$$-\frac{1}{R_1 C_1} + \frac{\overline{v_{C2}}(\overline{v_{C2}} - V_2)}{C_1 R_2} \left(\frac{V_1}{2} + \sqrt{\frac{{V_1}^2}{4} - \overline{v_{C2}}(\overline{v_{C2}} - V_2)} \right)^{-2} \tag{4.48}$$

That is negative inside a large operation region. Hence, the zero-dynamics are asymptotic stable in this region, and consequently, the full system is asymptotic stable.

4.5 System Parameters

The application scenario for the performance verification of the 5-switch converter with the proposed control scheme is as an interface between two DC-buses/elements. It is assumed that the values of V_2 and R_2 are known. The rated voltages were taken as $V_1 = 96$ V and $V_2 = 380$ V and the rated power 1.9 kW. Other converter parameters are: Turns ratio $n = 2$, $L_M = 38.8$ µH, $C_1 = 76.8$ µF, $C_2 = 76.8$ µF, and $f_{sw} = 250$ kHz. The feeder resistances are $R_1 = 0.0625$ Ω and $R_2 = 0.0625$ Ω. These parameters are similar to those used in in Chapters 2 and 3. The gains (λ_1 and λ_2) of the non-linear controller with exact state feedback linearization for the converter operating in tri-state Buck-Boost mode were computed, based on pole placement from linear control theory, as 250 k and 350 k, respectively. These gains are computed taking into account the behavior of a first-order system, where they relate to the time constant (T_{sys}) of such systems. In this case, $T_{sys\_\lambda 1}$=16 µs and $T_{sys\_\lambda 2}$=11.4 µs.

In order to demonstrate the feasibility and benefits of the proposed mode of operation, tri-state Buck-Boost, and state feedback linearization, its performance is compared in the next Section with a conventional technique. Usually, a converter like this operates in dual-state Buck-Boost mode with a cascaded inner current (i_{LM}) and outer voltage (v_{C2}) control loop, as presented in Figure 4.7.

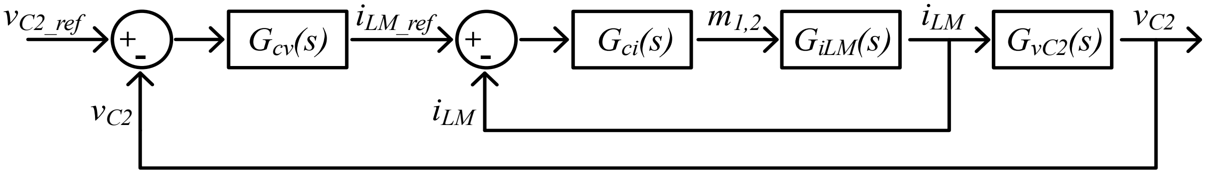

Figure 4.7 – Block diagram of the cascaded control

The small-signal model is obtained by means of the standard linearization of (4.16) - (4.18). For operation in Dual-state Buck-Boost mode, considering the modulation schemes discussed in last Chapter and the proposed PWM-modulator presented in Figure 4.1, one has to set m_3 to 1 V, to eliminate the free-wheeling states (S_{34} for the forward mode and S_{12} for the reverse mode), and then use the same control signal for m_1 and m_2 in order to eliminate states S_{23} and S_{14}, thus controlling the converter with a single control input, determined by $m_{1,2}$ in Figure 4.7. The value of q is set at 1, since the Forward power flow, which presents Boost characteristics, is the worst case concerning the design of the PI-controller. With $m_{1,2}$ as the control variable, $m_2 = 1$ and $q = 1$, one substitutes (4.19) and (4.20) in (4.16)-(4.18) to obtain new state equations as a function of a single control variable: $m_{1,2}$. Then, one employs the conventional linearization technique, based on small-signal variations around a base operating point to obtain transfer functions ($i_{LM}(s)/m_1(s)$ and $v_{C2}(s)/i_{LM}(s)$). The first can be found to be.

$$G_{iLM}(s) = \frac{i_{LM}(s)}{m_{1,2}(s)} = \frac{[R_2C_2(V_{C1} + nV_{C2})]s + \left[n^2R_2\left(1 - m_{1,2}\right)I_{LM} + V_{C1} + nV_{C2}\right]}{(R_2C_2L_M)s^2 + (L_M)s + n^2R_2\left(1 - m_{1,2}\right)^2} \quad (4.49)$$

It is used for designing the PI-type controller of the inner current loop for zero error in steady-state to step changes. For the design of the outer voltage control loop, considering that its bandwidth is 10-20% of the one for the inner current loop, the latter can be assumed to be a unity gain. Next, one can derive an expression for $v_{C2}(s)/i_{LM}(s)$, applying the current division principle that relates the current in the output capacitor ($i_{C2}(s)$) to $i_{LM}(s)$. This results in:

$$i_{C2}(s) = ni_{LM}(s)\left(1 - m_{1,2}\right) - i_2(s) = ni_{LM}(s)\left(1 - m_{1,2}\right) - \frac{v_{C2}(s) - V_2}{R_2} \tag{4.50}$$

Finally, by assuming that V_2 remains constant, one can compute the transfer function of the output capacitor voltage over the inductor current as:

$$G_{vC2}(s) = \frac{v_{C2}(s)}{i_{LM}(s)} = \frac{nR_2\left(1 - m_{1,2}\right)}{(R_2C_2)s + 1} \tag{4.51}$$

In this particular case, standard type-2 PI-controllers can be designed to provide the chosen bandwidths and phase margins for the inner and outer control loops. The parameters of the linear PI controllers were computed as follows: For the inner current loop, the bandwidth is selected as 50 kHz with a phase margin of 60°, resulting in $K_{pi} = 0.0427$, $\tau_i = 11.88$ μs and $f_{pi} = 186.7$ kHz. For the outer voltage loop, the bandwidth is chosen as 10 kHz with a phase margin of 60°, leading to $K_{pv} = 75.43$, $\tau_v = 12.62$ μs and $f_{pv} = 7.93$ kHz.

4.6 Performance Verification

Two types of tests were conducted, by means of simulations with PSIM, to demonstrate the feasibility and the advantages of the proposed 5-switch converter with a nonlinear control scheme based on exact state feedback linearization. First, it is assumed that the input voltage (v_1) is kept constant at 96 V, while the voltage at Bus 2 (v_2) is rated at 380 V and presents a triangular ripple between 370 V and 390 V, with a frequency of 40 Hz. The output current reference signal (i_{2_ref}) is a square waveform of +/- 5 A and 5 Hz. This can be seen as the case where the 5-switch converter (and control law) acts as an interlink converter between a strongly regulated DC-bus (meaning that its voltage remain constant regardless of the power injected to, or withdrawn from, the DC-bus) and a DC-Microgrid employing multiple variable loads. This can be considered as the base case. Here, the main goal is to verify whether one can control the output current (i_2) that is injected into the DC-Microgrid.

Next, a SC is used in Bus 1 (v_1). Typically, the voltage on a SC is allowed to vary between half-rated and rated values. This might present a challenge for the performance of the conventional PI-controllers, designed for a fixed operating point. Conversely, the non-linear control scheme with state feedback linearization should be able to compensate for this condition, presenting similar behavior in a wide range of operating points.

Another aspect to be considered is the operating mode of the converter to be used. Since the control is designed in terms of the nonlinear variables u_1 and u_2, a suitable conversion to $m_{1,2,3}$ must be employed. For this, a Tri-state Buck-Boost mode with free-wheeling state is considered in this Thesis. This way, considering the PWM modulator presented in Figure 4.1, if one wants to employ the mentioned operating mode, one has to set $m_1 = m_2$ in order to eliminate states S_{23} and S_{14} for the forward and reverse modes, respectively, and then control the converter in terms of $m_{1,2}$ and m_3.

4.6.1 Tests with a Fixed V_1 and V_2 with a Triangular Ripple

Figure 4.8 shows some key waveforms concerning the operation of the proposed nonlinear controller with a fixed voltage at Bus 1. The 370 V to 390 V triangular ripple at the voltage of Bus 2 (v_2), as depicted in Figure 4.8(a), is considered a disturbance in the system. In Figure 4.8(b) one sees that the output current (i_2) follows the reference signal (i_{2_ref}). This is achieved indirectly by controlling the output voltage of the converter (v_{C2}) as shown in Figure 4.8(c). The reference (i_{LM_ref}) and inductor current (i_{LM}) are shown in Figure 4.8(d). There one sees that i_{LM} tracks i_{LM_ref} very well and that power flow reversal, with i2 changing from -5 A to 5 A, can be done without reversing i_{LM}. What is more, the control of the two state variables, v_{C2} and i_{LM}, is done in a decoupled way as discussed in Section 4. It is worth pointing out that the i_{LM_ref} is kept at 25 A until t = 0.25 s, when it is changed to 35 A, and then changed back to 25 A at t = 0.35 s. This action has two goals. First is to show the good tracking capability of the inductor current control loop, to step changes. A change in i_{2_ref} has a minor effect on i_{LM}. Second, is to show the impact of the magnitude of i_{LM} on the values of the modulation signals, as discussed below. The waveforms of control variables (u_1 and u_2) which includes the flag "q" with the direction of the power flow are shown in Figure 4.8(e). Those concerning the modulation signals (m_1, m_2 and m_3) used in the PWM modulator can be seen in Figure 4.8(f). They remain within the range of the sawtooth carrier, 0 to 1 V, as expected. There one can see that as i_{LM_ref} increases, the magnitude of the modulation signals decrease.

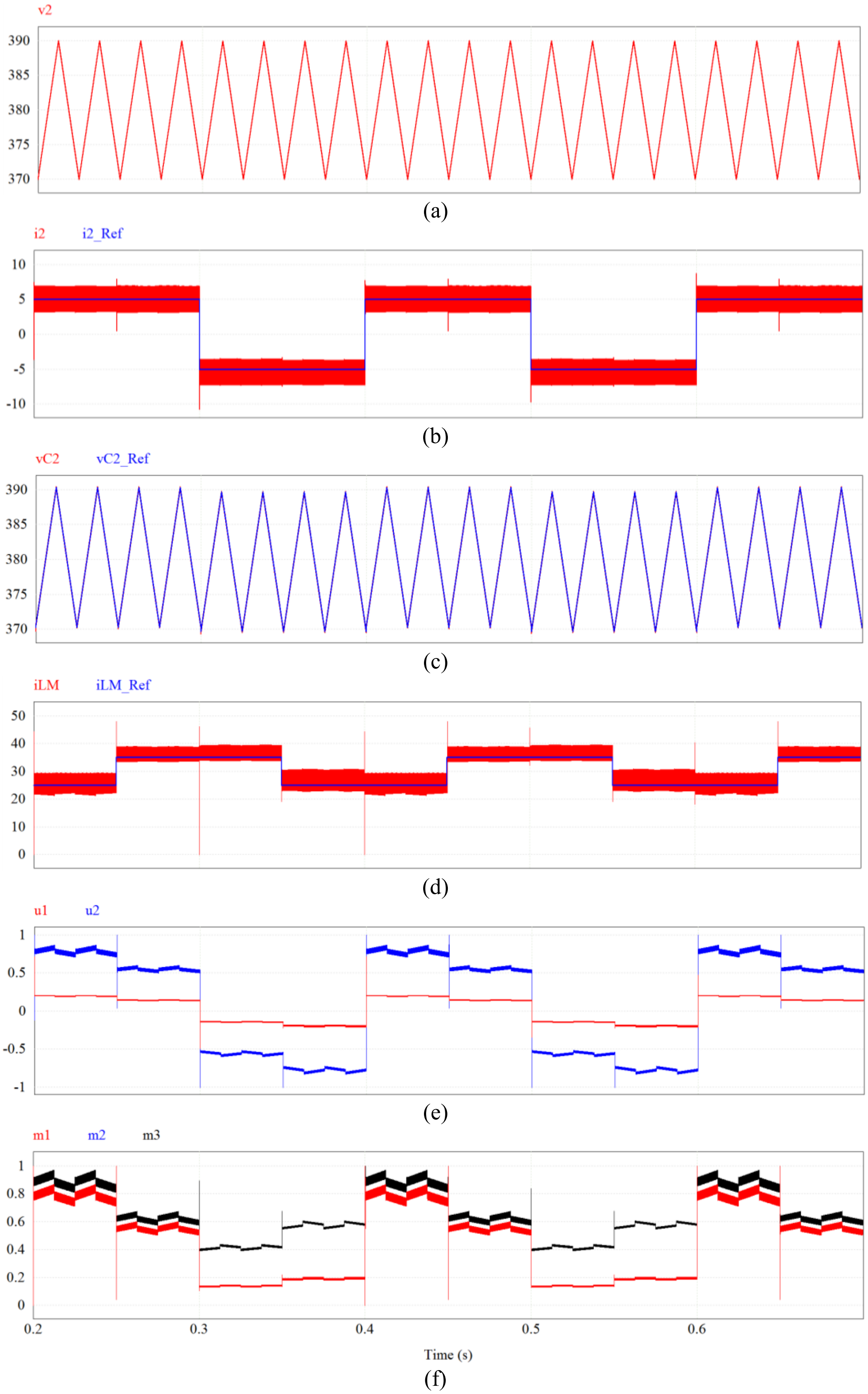

Figure 4.8 – Waveforms for the tri-state Buck-Boost control with exact state feedback linearization:
(a) Voltage at Bus 2 (in V), (b) reference and output current (in A), (c) reference and output capacitor voltage (in V),
(d) reference and inductor current (in A), (e) non-linear control variables, (f) PWM modulation signals.

Next, Figure 4.9 presents the results for essentially the same test, but for the converter operating in Dual-state mode with the cascaded linear controller.

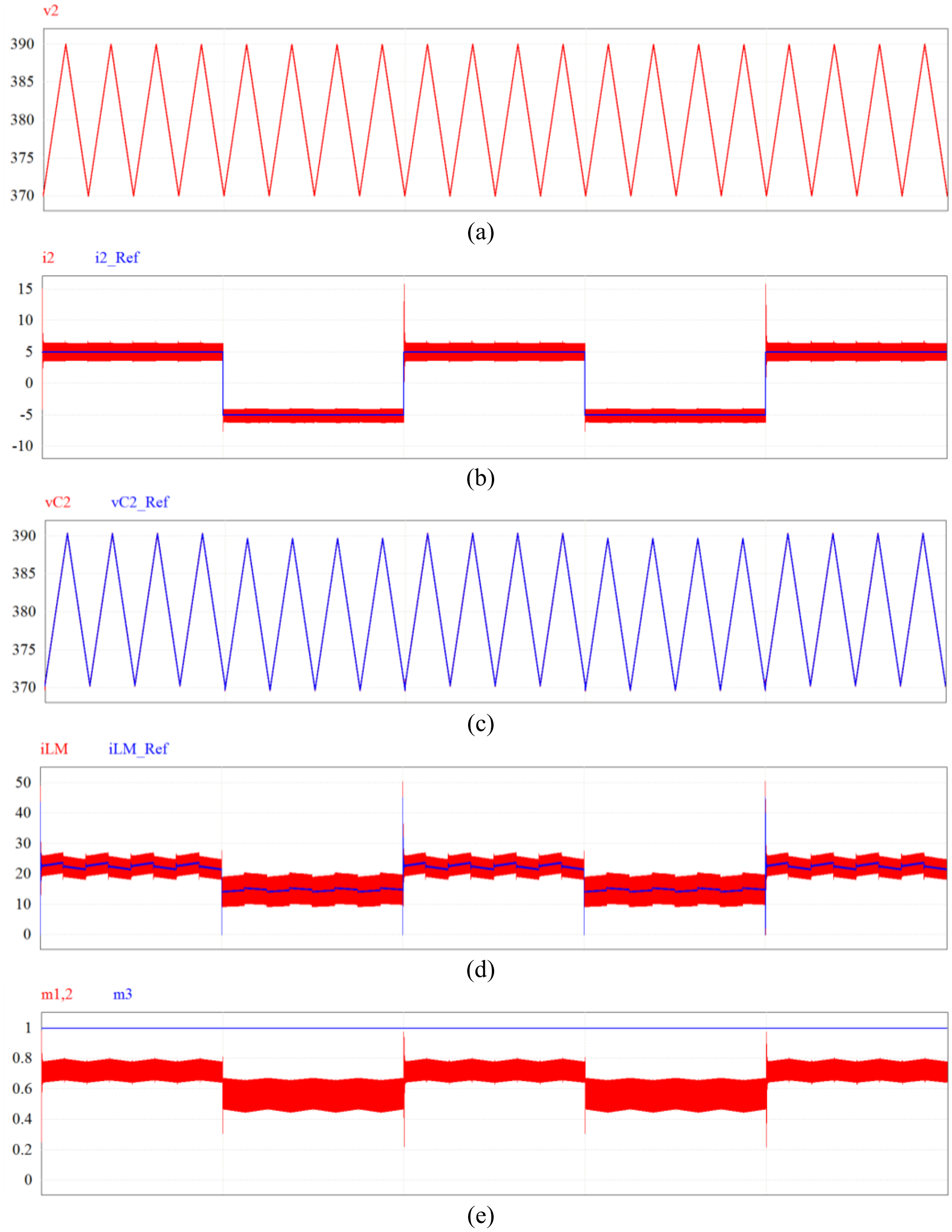

Figure 4.9 – Waveforms for the dual-state Buck-Boost control with conventional cascaded control loops: (a) Voltage at Bus 2 (in V), (b) reference and output current (in A), (c) reference and output capacitor voltage (in V), (d) reference and inductor current (in A), (e) PWM modulation signals.

In this case, the output voltage (v_{C2}) is adjusted by varying the inductor current (i_{LM}). In general, no major difference can be seen between the two control schemes regarding the control of the output current (i_2) in Figure 4.8(b) and Figure 4.9(b). Both control schemes present fast and accurate tracking of the output current reference (i_{2_ref}). However, this is achieved with different values for the i_{LM}, Figures 4.8(d) and 4.9(d). For the conventional cascaded control scheme, the inductor current reference i_{LM_ref} varies with the output voltage reference (v_{C2_ref}). When the power flow is reversed, at t = 0.3s and t = 0.4s, i_{LM} also changes, but it remains always positive. This is a feature of the 5-switch bidirectional DC-DC converter. Thus, i_{LM} and v_{C2} are coupled variables. Finally, Figure 4.9(e) shows that just only one modulation signal, $m_{1,2}$, is used for both power flow directions for the conventional cascaded controller, while the other one, m_3, is kept at 1V at all times.

4.6.2 Tests with a SC at Bus 1

In this test, the fixed voltage, or "strong bus" previously used in Bus 1, is replaced by a SC, a storage element, another common application for bidirectional DC-DC converters. This concerns a more demanding operating condition where the input voltage of the converter (v_1) can vary quite a bit, driving the operating point of the converter further away from the base operating point. There are several papers concerning the sizing of SCs for given applications [67] – [70]. In this test, the size of the SC was chosen in a way to show that the proposed control scheme is effective for operating with input voltages varying from rated to half-rated. This is a typical requirement for SC interfaces. In this particular test, a small supercapacitor (95 mF) was considered for the test so that one can observe the impact of its voltage variation on the response of the inductor current (i_{LM}) and output voltage (v_{C2}) control loops, in a single time frame.

Figure 4.10 shows some relevant waveforms for this test. The voltage waveform at Bus 2 (v_2) is the same as in the previous test, thus, it is omitted in the Figure. In Figure 4.10(a), one sees that the output current (i_2) tracks very well the reference signal (i_{2_ref}), a square wave of +/- 5 A and 5 Hz. The waveform of v_1 is shown in Figure 4.10(b). It starts at 96 V and decreases due to a positive value for i_2. At t = 0.3 s, it reaches about 72 V and starts to increase as the value of i_2 changes to – 5 A. Thus, the variation of v_1 had no negative impact on the performance of the proposed control scheme. Then, v_{C2} in Figure 4.10(c) and the i_{LM} in Figure 4.10(d) track their reference signals accurately. Note that in this case, the inductor current reference (i_{LM_ref}) was kept constant at 35 A. The good tracking performance was achieved with the waveforms of control variables (u_1 and u_2) shown in Figure 4.10(e) and modulation signals (m_1 and m_2) shown in Figure 4.10(f).

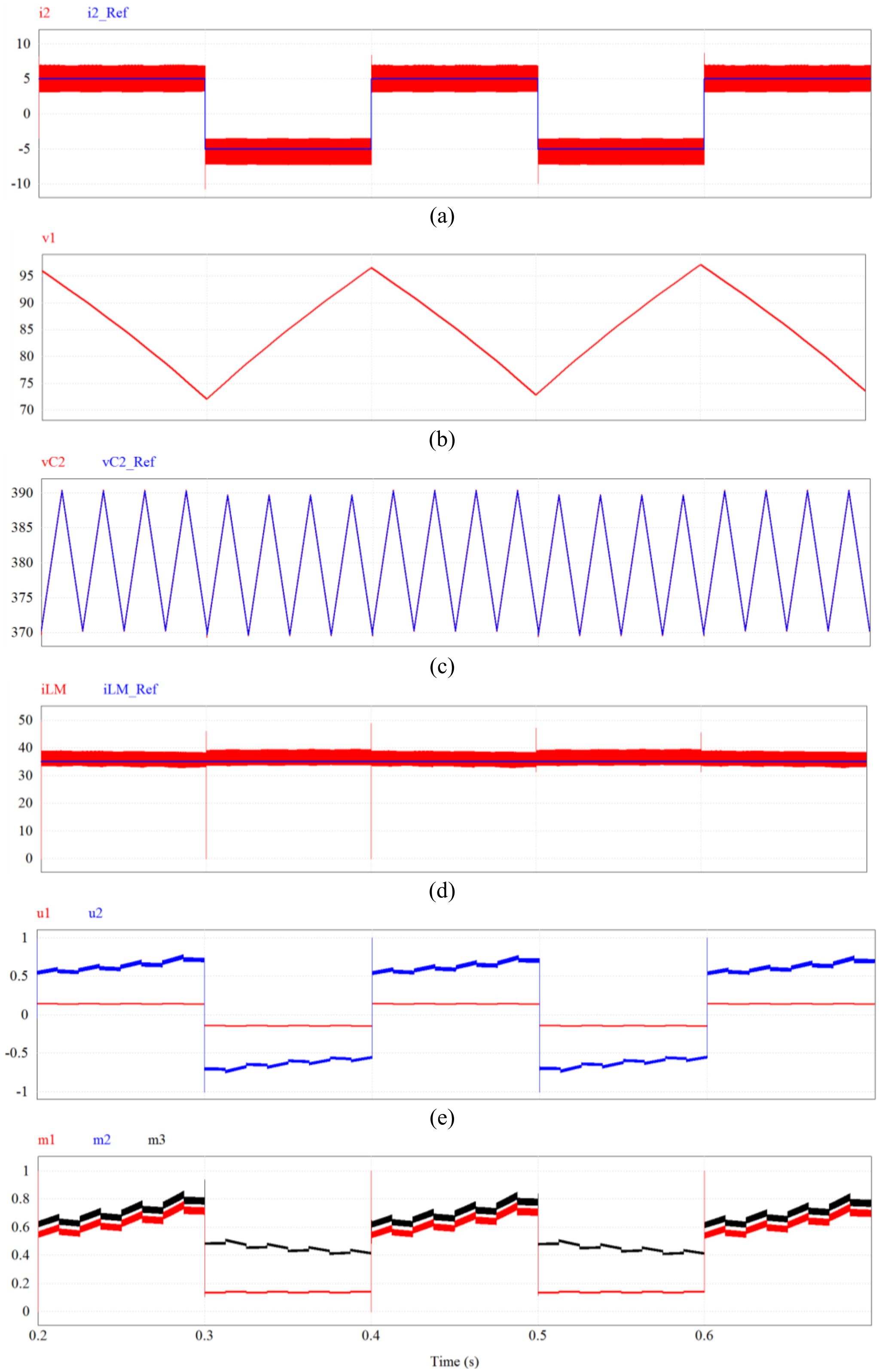

(a)

(b)

(c)

(d)

(e)

(f)

Figure 4.10 – Waveforms for the tri-state Buck-Boost control with state feedback linearization for test 2: (a) reference and output current (in A), (b) voltage at Bus 1 (in V), (c) reference and output capacitor voltage (in V), (d) reference and inductor current (in A), (e) nonlinear control variables, (f) PWM modulation signals.

The 5-switch converter operating with Dual-state Buck-Boost and conventional linear cascaded control loops is subjected to the same test. The results are shown in Figure 4.11.

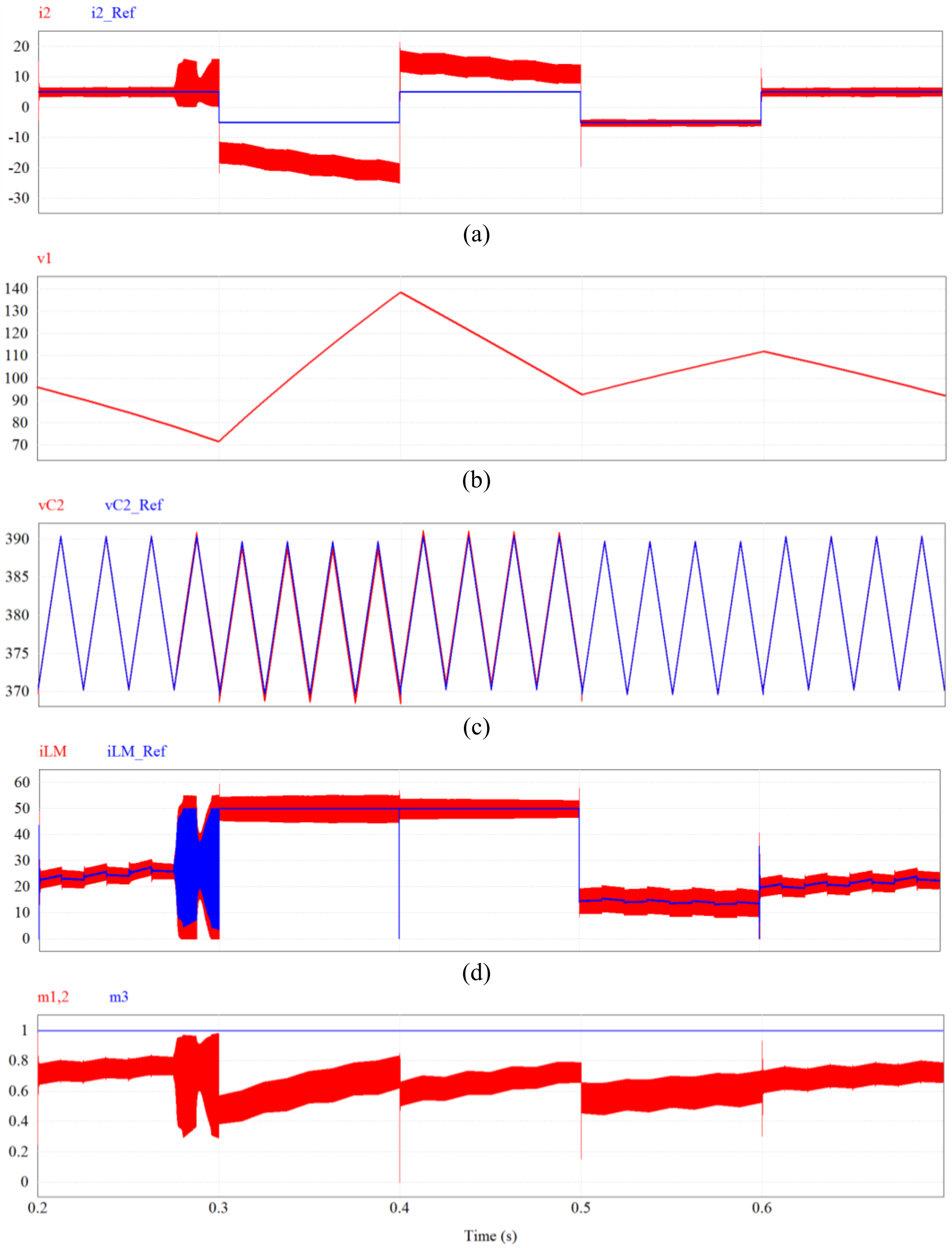

(a) (b) (c) (d) (e)

Figure 4.11 – Waveforms for the conventional cascaded control scheme for test 2:
(a) reference and output current (in A), (b) voltage at Bus 1 (in V), (c) reference and output capacitor voltage (in V),
(d) reference and inductor current (in A), (e) PWM modulation signals.

In Figure 4.11(a), one sees that it tracks the positive output current reference (i_{2_ref}) well until the moment the decreasing input voltage, (v_1) in Figure 4.11(b), reaches about 78.5 V. That is when the modulation signal ($m_{1,2}$) and several waveforms start to oscillate. The control scheme starts to mal function. At t = 0.3s, when the power flow reverses and i_{2_ref} = -5 A, the output current (i_2) fails to track it, becoming more negative (lower) than i_{2_ref}. The inductor current (i_{LM}) and inductor current reference (i_{LM_ref}) waveforms, shown in Figure 4.11(d), are limited at the maximum value, 50 A. One sees in Figure 4.11(e) that the modulation signal ($m_{1,2}$) decreases following the change of i_{2_ref} to -5 A, but starts to increase, unlike in the previous test, when its average value remained relatively constant. Overall, as a result of i_2 becoming more negative than i_{2_ref} at t = 0.3 s, v_1 increases more than expected, reaching 140 V at t = 0.4s. That is when i_{2_ref} becomes positive again but, still, i_2 fails to track it. Nonetheless, v_1 decreases. At t = 0.5s, when i_{2_ref} becomes -5 A and with v_1 with a value of about 92V, which is close to its rated value (96 V), the conventional control scheme starts to work again, with i_2 tracking i_{2_ref} well, until the end of the test.

4.6.3 Results for SC Voltage Falling to Half-Rated Value

This test is conducted only for the proposed control and modulation scheme, since the conventional one was unable to track the output current reference signals, for the voltage in Bus 1 (v_1) varying between about 96 V and 72 V. To have the SC voltage decreasing from rated (96 V) to half-rated (48 V) using the same square output current reference (i_{2_ref}) of +/- 5 A and 5 Hz, a smaller supercapacitor of 55 mF was used in this test.

Figure 4.12 shows some relevant waveforms for this test. The voltage waveform at Bus 2 (v_2) is the same as in the previous tests, thus, it is again omitted in the Figure. In Figure 4.12(a), one sees that the output current waveform (i_2) tracks very well i_{2_ref}. The voltage at the SC (v_1) is shown in Figure 4.12(b). It starts at 96 V and decreases due to the positive value for i_2. At t = 0.3s, it reaches 48 V and starts to increase as the value of i_2 changes to – 5 A. Thus, the large variation of v_1 had no negative impact on the performance of the proposed control scheme. The output capacitor voltage (v_{C2}) in Figure 4.12(c) and the inductor current (i_{LM}) in Figure 4.12(d) track their reference signals accurately. Note that in this case, the inductor current reference (i_{LM_ref}) was increased to 45A in order to avoid the saturation of the control variables that tend to increase as v_1 decreases. The good tracking performance was achieved with the waveforms of control variables (u_1 and u_2) shown in Figure 4.12(e) and modulation signals (m_1, m_2 and m_3) shown in Figure 4.12(f).

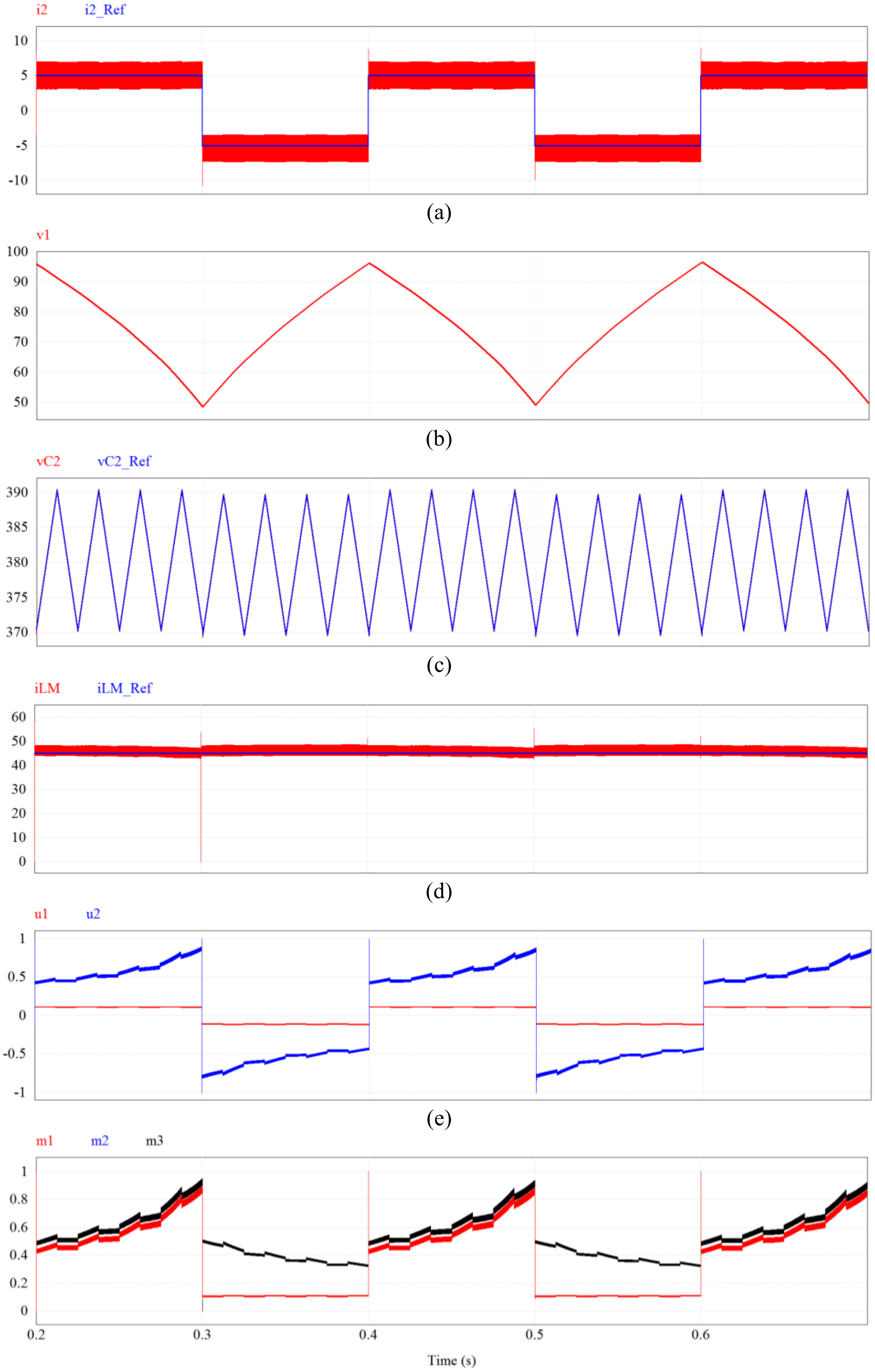

(a)

(b)

(c)

(d)

(e)

(f)

Figure 4.12 – Waveforms for the tri-state Buck-Boost control with state feedback linearization for test 3:
(a) reference and output current (in A), (b) voltage at Bus 1 (in V), (c) reference and output capacitor voltage (in V),
(d) reference and inductor current (in A), (e) nonlinear control variables, (f) PWM modulation signals.

4.7 Chapter Conclusion

The performance of Energy Storage Systems (ESSs), in terms of dynamic response and tracking of the reference output current, depends on the features of the power converter and control scheme. This Chapter presented the modelling of the novel 5-switch DC-DC power converter, which presents a high voltage gain (V_2/V_1) and does not require the reversal of the intermediate inductor current to achieve power flow reversal. In terms of control scheme, by operating this converter in a tri-state Buck-Boost mode, one eliminates the RHP zero from the output-to-control transfer function what facilitates the design of the control loop. Besides, by employing the exact state feedback linearization technique, the converter should be able to operate in a wider range than that with a PI-controller designed considering the conventional small-signal model of the converter. A systematic approach for modelling the converter and obtaining a control law with exact feedback linearization was presented. Note that since the inductor current, a state variable, does not need to reverse during power flow reversal in this particular converter, there will be not potential issues of "divide by zero" in the control law.

The performance of the 5-switch DC-DC power converter with the proposed modulation (Tri-state Buck-Boost) and control scheme (exact state feedback linearization) was verified by means of simulations. The selected application was as the interface of a SC-based ESS to an output DC-bus, such as a DC-Microgrid. It was compared to the converter operating in the conventional Dual-state Buck-Buck mode with linear cascaded current control loops. As expected, both control schemes present similar good behavior at the operating point where the conventional scheme was designed for. When the input voltage (V_1) varies even moderately, what is common in SC-based ESSs, the conventional scheme fails to track the output current reference. Conversely, the proposed modulation and control scheme tracks accurately, with good dynamic response and zero stead-state error, the output current reference even with the SC voltage varying in a wide range, from rated to half-rated. This is an important feature of interfaces of SC-based ESSs that is difficult to obtain with conventional power converters and control schemes.

5. Final Conclusions and Future Work

This research work was focused on modeling and control techniques applied to power electronics converters. First, the Introduction provided an overview of the applications targeted by this research work and how the work proposed in this PhD degree can address the problems and limitations of such technologies.

Chapter 2 presented a “unified controller for multi-state operation” for the conventional 4-swtich Bidirectional Buck-Boost DC-DC converter. Its novelty/contribution was on the configuration of the control scheme with: 1) PWM with three modulation signals for multi-state operation and 2) multi-variable (i_L and v_{C2}) control with feedback linearization. This required the development of a mathematical model for the converter that allows the design of the PI-controllers as well as the control laws and for both nonlinear control variables (w_1 and w_2). In the proposed control scheme, a multi-variable control scheme was employed, where control variable w_1 was used to control v_{C2} and w_2 to control i_L. The decoupling of the two control loops was achieved by means of feedback linearization. Besides, one can have the converter operating in various multi-state modes with the same controllers with the same dynamic response, which is beneficial for the applications targeted in this thesis, where the operating points/conditions constantly change. Simulation results for a SC-based ESS showed that the proposed control scheme provided fast and accurate regulation for step changes in the reference quantities under bi-directional power flow.

Then, to deal with some of the limitations presented by the converter and control law discussed in Chapter 2, which are the limited voltage gain provided by such topology and the zero crossing of the inductor current for bidirectional power flow, Chapter 3 proposed a novel bidirectional power electronics topology based on a Tapped-Inductor (TI). For this new topology, high voltage gain that can be achieved by adjusting the turns ratio (n) of the TI, allowing this new converter to work with wide input/output voltage ratios. Also, the arrangement of the power switches allows the direction of the power flow to be reversed without changing the direction of the intermediate inductor (magnetizing inductance in this case) current, which is well suited for nonlinear control approaches where the inductor current is frequently a denominator term in the control law. The working principle of the novel power electronics converter, including possible operating states/modes, was presented and discussed in detail. The theoretical analysis for a group of operating modes leading to design equations was carried out. Such equations were used for a well-oriented approach to determine the value of n and modes of operation in a given case study.

Finally, Chapter 4 presented the development of a nonlinear controller based on exact state feedback linearization employing Lie derivatives for the novel 5-switch bidirectional DC-DC converter. An explicit formal mathematical control design and stability analysis, based on a zero-dynamics formalism, was presented for such controller. This required the development of a unified mathematical model for the converter that allows the design of the control laws for control variables u_1 and u_2 of the nonlinear controllers. The proposed nonlinear control law was then compared to a conventional linear method usually used for the same application. The claim of performance improvement is on the control and dynamic response of the converter. It is intended to have the same performance regardless the conditions the converter is operating under, in this case being wide variations of input and output voltage, which is a common scenario for the application targeted in this Thesis. The results show that both control schemes work similarly well at the operating point where the conventional control scheme was designed for. However, only the proposed nonlinear control scheme allows the SC-based ESS to control the current injected into the DC-Microgrid with the voltage of the SC varying between the expected ranges of rated to half-rated.

5.1 Future Work

The work presented throughout this thesis validates the proposed modeling and control techniques and novel bidirectional power electronics topology by means of simulation using switched models. As such, current and voltage harmonics, potential of controller saturation and transport delays due to Pulse-Width Modulation are present in the system and simulation. These are phenomena that can impact the performance and validation of "modeling and control techniques" for power electronics converters. Conversely, the switched simulation approach does not, typically, takes into account switching and conduction losses, parasitic inductances and resistances in the passive components and so on. These have minimum, if any, impact on the validation of modeling and control techniques for power electronics converters, like the ones reported in this thesis. In this sense, simulations allow much more flexibility and easy to test different configurations and variations of parameters and operation points to better identify the effects of the controller, allowing the results to pinpoint control behavior aspects. Such results are often drowned among several other implementation aspects, and do not allow to highlight the control ones.

However, it is well-established for the academia that a working experimental prototype subject to multiple tests is the ultimate evidence of validation for a given technique, circuit or system. Therefore the natural next steps and future work of this research work would be the experimental validation of the proposed switching schemes and control techniques as well the novel 5-switch converter. This is currently being developed, where a prototype of the novel 5-switch Tapped-Inductor Multi-State Bidirectional DC-DC converter has been assembled in the power electronics laboratory for further testing.

Another possible path for future work is the investigation of different nonlinear control approaches for the power electronics converters and the switching-schemes/models proposed in this research work. In this thesis, the nonlinear control laws were developed based on feedback linearization approaches, where auxiliary nonlinear feedback and feedforward terms were introduced to the model so the system could be treated as linear for an extended operating region. However, there are still a number of different approaches that could be evaluated for such systems. Among these approaches, one could employ Lyupanov-based methods such as Backstepping and Sliding modes.

REFERENCES

[1] T. Dragicevic, X. Lu, J. C. Vasquez and J. M. Guerrero, "DC Microgrids – Part I: A Review of Control Strategies and Stabilization Techniques" on IEEE Transactions on Power Electronics, vol. 31, no. 7, pp. 4876-4891, July 2016.

[2] T. Dragicevic, X. Lu, J. C. Vasquez and J. M. Guerrero, "DC Microgrids – Part II: A Review of Power Architectures, Applications, and Standardization Issues" on IEEE Transactions on Power Electronics, vol. 31, no. 5, pp. 3528-3549, May 2016.

[3] A. T. Ghareeb, A. A. Mohamed and O. A. Mohammed, "DC Microgrids and Distribution Systems: An Overview" on IEEE Power & Energy Society General Meeting 2013, Vancouver – Canada, July 2013.

[4] L. F. N. Delboni, D. Marujo, P. P. Balestrassi and D. Q. Oliveira, "Electrical Power Systems: Evolution from Traditional Configuration to Distributed Generation and Microgrids" on Zambroni de Souza, A., Castilla, M. (eds) Microgrids Design and Implementation Springer Verlag, pp. 1-25, 2019.

[5] T. Adefarati and R. C. Bansal, "Integration of renewable distributed generators into the distribution system: a review" on IET Renewable Power Generation, vol. 10, no. 6, pp. 873-884, August 2016.

[6] J. Lai and M. W. Ellis, "Fuel Cell Power Systems and Applications" on Proceedings of the IEEE, vol. 105, no. 11, pp. 2166-2190, November 2017.

[7] O. Lucia, I. Cvetkovic, H. Sarnago, D. Boroyevich, P. Mattavelli and F. C. Lee, "Design of Home Appliances for a DC-Based Nanogrid System: An Induction Range Study Case" on IEEE Journal of Emerging and Selected Topics in Power Electronics, vol. 1, no. 4, pp. 315-326, September 2013.

[8] E. R. Diaz, M. Savaghebi, J. C. Vasquez, and J. M. Guerrero, "An overview of low voltage dc distribution systems for residential applications," on IEEE 5th International Conference on Consumer Electronics – Berlin (ICCE – Berlin), pp. 318-322, September 2015.

[9] P. H. Nguyen, M. M. V. M. Ali, F. M. Portelinha Jr, P. F. Ribeiro and J. F. G. Cobben, "Emerging Control Technologies and Load Management in Microgrids" on Zambroni de Souza, A., Castilla, M. (eds) Microgrids Design and Implementation Springer Verlag, pp. 217-237, 2019.

[10] D. Boroyevich, I. Cvetkovic, D. Dong, R. Burgos, F. Wang and F. Lee, “Future electronic power distribution systems – A contemplative view” on 12th International Conference on Optimization of Electrical and Electronic Equipment 2010, Basov – Romania, pp. 1369-1380, May 2010.

[11] T. Castelo, M. F. Z. de Souza, C. Duque and P. F. Ribeiro, “Power Quality and Hosting Capacity in Islanding Microgrids” on Zambroni de Souza, A., Castilla, M. (eds) Microgrids Design and Implementation Springer Verlag, pp. 269-286, 2019.

[12] L. A. S. Ribeiro, O. R. Saavedra, S. L. de Lima and J. de Matos, “Isolated Micro-Grids With Renewable Hybrid Generation: The Case of Lençóis Island” on IEEE Transactions on Sustainable Energy, vol. 2, no. 1, pp. 1-11, September 2010.

[13] F. Perez and G. Damm, “DC-Microgrids” on Zambroni de Souza, A., Castilla, M. (eds) Microgrids Design and Implementation Springer Verlag, pp. 447-475, 2019.

[14] J. G. de Matos, F. S. F. e Silva and L. A. S. Ribeiro, “Power Control in AC Isolated Microgrids With Renewable Energy Sources and Energy Storage Systems” on IEEE Transactions on Industrial Electronics, vol. 62, no. 6, pp. 3490-3498, June 2015.

[15] M. R. Sheibani, G. R. Yousefi, M. A. Latify and S. H. Dolatabadi, “Energy storage system expansion planning in power systems: a review” on IET Renewable Power Generation, vol. 12, no. 11, pp. 1203-1221, August 2018.

[16] T. Bocklisch, “Hybrid Energy Storage Systems for Renewable Energy Applications” on 9th International Renewable Energy Storage Conference (IRES) 2015, March 2015.

[17] J. Cao and A. Emadi, “A New Battery/UltraCapacitor Hybrid Energy Storage System for Electric, Hybrid, and Plug-In Hybrid Electric Vehicles” on IEEE Transactions on Power Electronics, vol. 27, no. 1, pp. 122-132, May 2011.

[18] W. Jing, C. H. Lai, S. H. W. Wong and M. L. D. Wong, “Battery-supercapacitor hybrid energy storage system in standalone DC microgrids: areview” on IET Renewable Power Generation, vol. 11, no. 4, pp. 461-469, May 2017.

[19] Yuanmao Ye, K. W. E. Cheng, K. Ding, D. Wang and Y. Bao, “Hybrid Energy Storage System and Associated Converters Examinations for DC Distribution” on 5th International Conference on Power Electronics Systems and Applications (ICPESA) 2013, December 2013.

[20] G. R. Broday, "Bidirectional DC-DC Converters for Hybrid Energy Storage Systems in Electric Vehicle Applications", M.S. thesis, Dept. of Electronic Eng., UTFPR - Federal University of Technology of Paraná, Ponta Grossa, Brazil, 2016.

[21] S. Ferahtia, A. Djeroui, T. Mesbahi, A. Houari, S. Zeghlache, H. Rezk and T. Paul, "Optimal Adaptive Gain LQR-Based Energy Management Strategy for Battery–Supercapacitor Hybrid Power System" on Energies, 14(6), 1660, pp. 1-16, March 2021.

[22] S. K. Kollimalla, M. K. Mishra, and N. L. Narasamma, "Design and Analysis of Novel Control Strategy for Battery and Supercapacitor Storage System" on IEEE Transactions on Sustainable Energy, vol. 5, no.4, pp. 1137-1144, October 2014.

[23] B. Hredzak, V. G. Agelidis and G. D. Demetriades, "A Low Complexity Control System for Hybrid DC Power Source Based on Ultracapacitor-Lead-Acid-Battery Configuration" on IEEE Transactions on Power Electronics, vol. 29, no.6, pp. 2882-2891, June 2014.

[24] J. M. A. Curti, H. J. Xiaoliang, R. H. Minaki and H. Yoichi, "A Simplified Power Management Strategy for a Battery/Supercapacitor Hybrid Energy Storage System Using the Half-Controlled Converter" on 38th Annual Conference on IEEE Industrial Electronics Society (IECON) 2012, pp. 4006-4011, October 2012.

[25] M. A. Abdullah, W. H. M. Yatim, C. Tan and A. S. Samosir, "Control of a Bidirectional Converter to Interface Ultracapacitor with Renewable Energy Sources" on IEEE International Conference on Industrial Technology (ICIT) 2013, pp. 673-678, February 2013.

[26] M. K Andreev, "An overview of Supercapacitors as New Power Sources in Hybrid Energy Storage Systems for Electric Vehicles" on XI National Conference with International Participation (ELECTRONICS) 2020, pp. 1-4, July 2020.

[27] A. Morais and L. A. C. Lopes, "Interlink Converters in DC nanogrids and its effect in power sharing using distributed control" on IEEE 7th International Symposium on Power Electronics for Distributed Generation Systems (PEDG) 2016, Vancouver – Canada, June 2016.

[28] X. Luo, J. V. Barreras, C. L. Chambon, B. Wu and E. Batzelis, "Hybridizing Lead–Acid Batteries with Supercapacitors: A Methodology" on Energies, 14(2), 507, January 2021.

[29] R. Mayer, A. Péres and S. V. Garcia Oliveira, "Multiphase Bidirectional DC/DC Non-Isolated Converter for Electric Drive System in Electric Vehicle and Hybrid Electric Vehicle" on Power Electronics Magazine, Campo Grande, vol. 20, no. 3, pp. 311-321, June-August 2015.

[30] R. Georgious, J. Garcia, M. Sumner, S. Saeed and P. Garcia, “Fault Ride-Through Power Electronic Topologies for Hybrid Energy Storage Systems” on Energies, 13(1), 257, January 2020.

[31] F. Perez, G. Damm, P. Ribeiro, F. Lamnabhi-Lagarrigue and L. Galai-Dol, “A Nonlinear Distributed Control Strategy for a DC MicroGrid using Hybrid Energy Storage for Voltage Stability” on IEEE 58th Conference on Decision and Control (CDC) 2019, Nice – France, December 2019.

[32] S. B Siad, A. Malkawi, G. Damm, L. Lopes and L. Galai-Dol, “Nonlinear control of a DC Microgrid for the integration of distibuted generation based on different time scales” on International Journal of Electrical Power and Energy Systems (IJEPES), vol. 111, pp. 93-100, April 2019.

[33] M. Gheisarnejad, H. Farsizadeh, M. Tavana and M. H. Khooban, “A Novel Deep Learning Controller for DC/DC Buck-Boost Converters in Wireless Power Transfer Feeding CPLs” on IEEE Transactions on Industrial Electronics, vol. 68, no.7, pp. 6379-6384, July 2021.

[34] O. Boutebba, S. Semcheddine, F. Krim, F. Corti, A. Reatti and F. Grasso, “A Nonlinear Back-stepping Controller of DC-DC Non Inverting Buck-Boost Converter for Maximizing Photovoltaic Power Extraction”, on IEEE International Conference on Environment and Electrical Enginnering and IEEE Industrial and Commercial Power Systems Europe (EEEIC/I&CPS) 2020, pp. 1-6, June 2020.

[35] A. Iovine, M. J Carrizosa, G. Damm and P. Alou, “Nonlinear Control for DC MicroGrids Enabling Efficient Renewable Power Integration and Ancillary Services for AC Grids” on IEEE Transactions on Power Systems, vol. 34, no.6, pp. 5136-5146, November 2019.

[36] C. Yuan, Y. Huangfu, R. Ma, B. Zhao and H. Bai, “Nonlinear PI and Finite-time Control for DC-DC Converter Based on Exact Feedback Linearization” on 45th Annual Conference of the IEEE Industrial Electronics Society (IECON) 2019, Lisbon – Portugal, pp. 6398-6403, October 2019.

[37] L. Callegaro, M. Ciobotaru, D. J. Pagano and J. E. Fletcher, “Feedback Linearization Control in Photovoltaic Module Integrated Converters” on IEEE Transactions on Power Electronics, vol. 34, no.7, pp. 6876-6889, July 2019.

[38] D. Shuai, “State feedback exact linearization control of Buck-Boost converter” on International Power Electronics and Application Conference and Exposition (PEAC) 2014, Shanghai – China, pp. 1490-1494, November 2014.

[39] F. Perez, A. Iovine, G. Damm, L. Galai-Dol and P. F. Ribeiro, “Stability Analysis of a DC Microgrid for a Smart Railway Station Integrating Renewable Sources” on IEEE Transactions on Control Systems Technology, vol. 28, no.5, pp. 1802-1816, September 2020.

[40] X. Li and X. Chen, “A Multi-Index Feedback Linearization Control for a Buck-Boost Converter” on Energies, 14(5), 1496, March 2021.

[41] F. Perez, A. Iovine, G. Damm and P. Ribeiro, “DC Microgrid Voltage Stability by Dynamic Feedback Linearization” on IEEE International Conference on Industrial Technology (ICIT) 2018, Lyon – France, pp. 129-134, February 2018.

[42] K. Viswanathan, R. Oruganti and D. Srinivasan, “A Novel Tri-State Boost Converter with Fast Dynamics” on IEEE Transactions on Power Electronics, vol. 17, no.5, pp. 677-683, September 2002.

[43] F. Caricchi, F. Crescimbini, F. G. Capponi and L. Solero, “Study of bi-directional Buck-Boost converter topologies for application in electrical vehicle motor drives” on IEEE 13rd Annual Applied Power Electronics Conference and Exposition (APEC) 1998, Anaheim – USA, February 1998.

[44] S. Saeed and L. A. C. Lopes, “Fault Protection Scheme for DC Nanogrids Based on the Coordination of Fault-Insensitive Power Electronic Interfaces and Contactors” on 45th Annual Conference of the IEEE Industrial Electronics Society (IECON) 2019, Lisbon – Portugal, pp. 5789-5794, October 2019.

[45] D.-H. Kim and B.-K. Lee, “An Enhanced Control Algorithm for Improving the Light-Load Efficiency of Noninverting Synchronous Buck-Boost Converters” on IEEE Transactions on Power Electronics, vol. 31, no.5, pp. 3395-3399, May 2016.

[46] S. Waffler and J. W. Kolar, “A Novel Low-Loss Modulation Strategy for High-Power Bidirectional Buck + Boost Converters” on IEEE Transactions on Power Electronics, vol. 24, no.6, pp. 1589-1599, June 2009.

[47] Y.-Y. Tsai, Y.-S. Tsai, C.-W. Tsai and C. –H. Tsai, “Digital Noninverting Buck-Boost Converter with Enhanced Duty-Cycle-Overlap Control” on IEEE Transactions on Circuits and Systems II: Express Briefs, vol. 64, no.1, pp. 41-45, January 2017.

[48] D. C. Jones and R. W. Erickson, “Buck-Boost Converter Efficiency Maximization via a Nonlinear Digital Control Mapping for Adaptive Effective Switching Frequency” on IEEE Journal of Emerging and Selected Topics in Power Electronics, vol. 1, no.3, pp. 153-165, September 2013.

[49] A. Choubey and L. A. C. Lopes, “A tri-state 4-switch bi-directional converter for interfacing supercapacitors to DC micro-grids” on IEEE 8th International Symposium on Power Electronics for Distributed Generation Systems (PEDG) 2017, Florianopolis – Brazil, pp. 1-6, April 2017.

[50] M. He, F. Zhang, J. Xu, P. Yang and T. Yan, “ High Efficiency Two-Switch Tri-State Buck-Boost Power Factor Correction Converter with Fast Dynamic Response and Low-Inductor Current Ripple” on IET Power Electronics, vol. 6, no. 8, pp. 1544-1554, September 2013.

[51] K. Viswanathan, R. Oruganti and D. Srinivasan, “Dual-mode control of tri-state boost converter for improved performance” on IEEE Transactions on Power Electronics, vol. 20, no.4, pp. 790-797, July 2005.

[52] I. Aharon, A. Kuperman and D. Shmilovitz, “Analysis of Dual-Carrier Modulator for Bidirectional Noninverting Buck-Boost Converter” on IEEE Transactions on Power Electronics, vol. 30, no.2, pp. 840-848, February 2015.

[53] N. Mohan, T. M. Undeland and W. P. Robbins, Power Electronics: Converters, applications and design, 3rd ed., USA: John Wiley & Sons, 2002.

[54] N. Mohan, Power Electronics: A First Course, 1st ed., USA: Wiley, 2011.

[55] D. A. Grant and Y. Darroman, “Extending the tapped-inductor DC-to-DC converter family” on Electronics Letters, vol. 37, no.3, pp. 145-146, March 2021.

[56] D. A. Grant, Y. Darroman and J. Suter, “Synthesis of Tapped-Inductor Switched-Mode Converters” on IEEE Transactions on Power Electronics, vol. 22, no.5, pp. 1964-1969, September 2007.

[57] W. Li, J. Xiao, J. Wu, J. Liu and X. He, “Application Summarization of Coupled Inductors in DC/DC Converters” on IEEE 24th Annual Applied Power Electronics Conference and Exposition (APEC) 2009, Washington DC – USA, pp. 1487-1491, February 2009.

[58] B. W. Williams, “Unified Synthesis of Tapped-Inductor DC-to-DC Converters” on IEEE Transactions on Power Electronics, vol. 29, no.10, pp. 5370-5383, October 2014.

[59] Y. T. Yau, W. Z. Jiang and K. I. Hwu, “Bidirectional Operation of High Step-Down Converter” on IEEE Transactions on Power Electronics, vol. 30, no.12, pp. 6829-6844, December 2015.

[60] G. R. Broday, C. B. Nascimento, E. Agostini Jr. and L. A. C. Lopes, “A Tri-State Bidirectional Buck-Boost Converter for A Battery/Supercapacitor Hybrid Energy Storage System in Electric Vehicle Applications” on IEEE Vehicular Power and Propulsion Conference (VPPC) 2015, Montral – Canada, pp. 1-6, October 2015

[61] A. Gonzalez, R. Lopez-Erauskin, J. Gyselinck, T. KeiChau, H. Ho-Ching and T. Fernando, “Nonlinear MIMO Control of Interleaved Three-Port Boost Converter by Means of State-Feedback Linearization” on IEEE 18th International Power Electronics and Motion Control Conference (PEMC) 2018, Budapest – Hungary, pp. 164-169, August 2018.

[62] P. Cai, X. Wu, R. Sun and Y. Wu, “Exact feedback linearization of general four-level buck DC-DC converters” on 29th Chinese Control and Decision Conference (CCDC) 2017, Chongqing – China, pp. 4638-4643, May 2017.

[63] D. Lee, G. Myoung Lee and K. Do Lee, “DC-bus voltage control of three-phase AC/DC PWM converters using feedback linearization” on IEEE Transactions on Industry Applications, vol. 36, no.3, pp. 826-833, May-June 2000.

[64] Z. Lu, X. Zhang and Y. Wang, “Nonlinear Control Strategy of Hybrid Energy Storage Systems Based on Feedback Linearization” on 4th CAA International Conference on Vehicular Control and Intelligence (CVCI) 2020, Hangzhou – China, pp. 674-677, December 2020.

[65] W. Ming and J. Liu, “A new experimental study of input-output feedback linearization based control of Boost type DC/DC converter” on IEEE International Conference on Industrial Technology (ICIT) 2010, Viña del Mar – Chile, pp. 685-689, March 2010.

[66] X. Li and X. Chen, “A Multi-Index Feedback Linearization Control for a Buck-Boost Converter” on Energies, 14(5), 1496, March 2021.

[67] D. B. W. Abeywardana, B. Hredzak, V. G. Agelidis and G. D. Demetriades, “Supercapacitor Sizing Method for Energy-Controlled Filter-Based Hybrid Energy Storage Systems” on IEEE Transactions on Power Electronics, vol. 32, no.2, pp. 1626-1637, February 2017.

[68] G. Dotelli, R. Ferrero, P. G. Stampino, S. Latorrata and S. Toscani, “Supercapacitor Sizing for Fast Power Dips in a Hybrid Supercapacitor-PEM Fuel Cell System” on IEEE Transactions on Instrumentation and Measurement, vol. 65, no.10, pp. 2196-2203, October 2016.

[69] D. Arnaudov, P. Punov and V. Dimitrov, “Supercapacitor Sizing for Power Defined Loads” on IEEE XXVIII International Scientific Conference Electronics (ET) 2019, Sozopol – Bulgaria, pp. 1-3, September 2019.

[70] A. Kuperman, M. Mellincovsky, C. Lerman, I. Aharon, N. Reichbach, G. Geula and R. Nakash, “Supercapacitor Sizing Based on Desired Power and Energy Performance” on IEEE Transactions on Power Electronics, vol. 29, no.10, pp. 5399-5405, October 2014.

[71] Ogata, K., Modern Control Engineering, Prentice Hall, 2010.